Instability-Driven Limits on Ion Temperature Anisotropy in the Solar Wind: Observations and Linear Vlasov Theory

Dissertation Advisor: Dr. Justin Christophe Kasper Bennett Andrew Maruca

Instability-Driven Limits on Ion Temperature Anisotropy in the Solar Wind: Observations and Linear Vlasov Theory

Abstract

Kinetic microinstabilities in the solar wind arise when its non-thermal properties become too extreme. This thesis project focused specifically on the four instabilities associated with ion temperature anisotropy: the cyclotron, mirror, and parallel and oblique firehose instabilities. Numerous studies have provided evidence that proton temperature anisotropy in the solar wind is limited by the actions of these instabilities. For this project, a fully revised analysis of data from the *Wind* spacecraft's Faraday cups and calculations from linear Vlasov theory were used to extend these findings in two respects. First, theoretical thresholds were derived for α-particle temperature anisotropy instabilities, which were then found to be consistent with a statistical analysis of *Wind* α-particle data. This suggests that α-particles, which constitute only about 5% of ions in the solar wind, are nevertheless able to drive temperature anisotropy instabilities. Second, a statistical analysis of *Wind* proton data found that proton temperature was significantly enhanced in plasma unstable due to proton temperature anisotropy. This implies that extreme proton temperature anisotropies in solar wind at 1 AU arise from ongoing anisotropic heating (versus cooling from, e.g., CGL double adiabatic expansion). Together, these results provide further insight into the complex evolution of the solar wind's non-fluid properties.

Contents

Acknowledgments

While working on this thesis project, I have relied on the help and support of many people. Though I could never hope to recognize all of them here, I do wish to express my thanks to a few in particular.

First, I extend my gratitude to my advisor, Justin Kasper, who has been my mentor, my advocate, and my friend. Working for Justin has been an honor and a joy, and, under his guidance, I have grown both professionally and personally. I also thank Jim Moran for his patient mentorship and for always having faith in me (even when I have not). I am very grateful to Peter Gary as well, who, beyond providing me with his linear Vlasov code, has shared his expertise and wisdom. I also humbly acknowledge the guidance of the other members of my thesis advisory committee: Doug Finkbeiner, Steve Cranmer, and John Raymond.

I have drawn upon the advice and friendship of many other scientists, and, in particular, I offer my thanks to Kelly Korreck, Mike Stevens, Stuart Bale, Rosanne di Stefano, Irwin Shapiro, and Lincoln Greenhill. I also thank Peg Herlihy, Donna Adams, and Jean Collins, who have tirelessly provided administrative support and have always been ready with a caring word and a sympathetic ear.

I extend additional thanks to my friends, who have showered me with innumerable kindnesses and have helped me to make this thesis project worthwhile. I especially thank my family — my parents, Terry and Karla, and my sisters, Becky and Vicki — for their patience, encouragement, and steadfast love.

This thesis project was supported by NASA Grant No. NNX08AW07G. In my research, I made use of the SAO/NASA Astrophysics Data System (ADS) in addition to calling upon the dedicated staff of the Wolbach Library.

pronaque cum spectent animalia cetera terram
os homini sublime dedit cælumque videre
iussit et erectos ad sidera tollere vultus

While other animals lean forward and gaze at the ground,
He gave to man a lofty countenance and commanded that
He look at the sky and raise his upright face to the stars.

∼ Ovid, *Metamorphoses* I.84-86

Chapter 1

Introduction

This chapter, the dissertation's introduction, was written to place this thesis project into a broader context and to overview fundamental concepts relating to it. Section 1.1 provides a brief history of heliophysics. Section 1.2 introduces definitions and prior results referenced throughout this dissertation, the structure of which is presented in Section 1.3.

1.1 Historical Overview of Heliophysics

Heliophysics is the study of the heliosphere: the region of space for which material from the Sun dominates conditions in the local environment. Of course, the study of the Sun is as old as astronomy itself. Throughout human history, virtually every society has recognized the importance of the Sun to its existence, and many went so far as to elevate the observation of the Sun to a divine office. Nevertheless, heliophysics is a relatively young discipline as its development has been heavily dependent on the in situ observations made possible by the Space Age.

1.1.1 Early Observations of the Solar Corona

That the Sun emits light was as obvious to the ancients as it is to humans today, but very few of the solar observations that have survived from antiquity unambiguously suggest material extending beyond the disk of the Sun. During a total solar eclipse, the solar corona (i.e., the Sun's "atmosphere") is plainly visible to the unaided eye. Scholars have identified various ancient symbols and drawings as including stylistic depictions of the corona (Bhatnagar & Livingston, 2005), though many of these interpretations are disputed. Plutarch (c. 90, 932 B) is often cited as providing the earliest, reasonably-credible description of the solar corona (Golub & Pasachoff, 1997):

> ἡ δὲ σελήνη κἂν ὅλον ποτὲ κρύψῃ τὸν ἥλιον, οὐκ ἔχει χρόνον οὐδὲ πλάτος ἡ ἔκλειψις ἀλλὰ περιφαίνεταί τις αὐγὴ περὶ τὴν ἴτυν οὐκ ἐῶσα βαθεῖαν γενέσθαι τὴν σκιὰν καὶ ἄκρατον.
>
> Even if the moon, however, does sometimes cover the sun entirely, the eclipse does not have duration or extension ; but a kind of light is visible about the rim which keeps the shadow from being profound and absolute. (Plutarch, 1957, translation)

During the European Renaissance, scientific observations of the corona during solar eclipses become more common and extensive. However, Kepler (1604, Chapter 8, Section 3) dismissed the corona as being simply an artifact of the lunar atmosphere refracting sunlight:

> *Etenim, quia supra capite 6. numero 9. eò audaciæ cum Plutarcho processimus, vt ausi fuerimus Lunæ, continentes, maria, montes & valles ascribere, quales hæc nostra tellus habet: quantum superest, vt & aërem Lunæ cirumfundamus, qualis huic nostræ terræ cirumfusus est? Tunc enim, nec id tamen crebrò, fiet id, quod supra capite 7. numero 5. de terrestri aëre demonstrauimus; vt radij ab extremitatibus Solis accedentes, Lunare corpus anfractu quodam, per refractiones in lunari aëre, circumeant, sicque ad visum nostrum breuiore cono terminentur.*
>
> Further, because in Chapter 6 Section 9 above we went along with Plutarch so far as to have dared to ascribe to the moon continents, seas, mountains, and valleys, such as this our earth has, how much more is it also to pour air around the moon, such as is poured around this our earth? For then, and even if it is not poured

> densely, that which we have demonstrated above in Chapter 7 Section 5 concerning the terrestrial air will happen: that the rays, approaching from the edges of the sun, go around the lunar body in a kind of bending through the refractions in the lunar air, and thus are bounded at our vision by a shorter cone. (Kepler, 2000, translation)

Of course, with the development of more sophisticated instruments and observing techniques, the corona was clearly identified as being a part of the Sun.

The nineteenth century saw the application of photography and spectroscopy to the study of the corona (Golub & Pasachoff, 1997). Photography greatly aided the study of the corona's many dynamic structures (e.g., streamers and prominences) (Proctor, 1884) and revealed the scale height of the corona to be on the order of one solar radius. However, such a thick atmosphere was inconsistent with spectroscopic observations of the Sun's photosphere (i.e., it's "surface"), which indicated temperatures of only about 6 000 K. Additionally, spectra of the solar atmosphere itself were found to contain many spectral lines that had never before been observed. This lead some to hypothesize that the corona was composed of an unknown, extremely light element, which became known as *coronium* (Golub & Pasachoff, 1997).

However, support for the existence of coronium eroded as continued laboratory measurements provided solar observers with more complete catalogs of spectral lines. Some of the mysterious lines in the solar atmosphere were identified with the previously unknown element helium[1]. However, others, in the corona itself, were found to originate from highly ionized states of iron, nickel, and calcium, the presence of which indicated coronal temperatures on the order of 1 MK (Abetti, 1962). While such high temperatures accounted for

[1]The word *helium* is aptly derived from the Greek word for *sun*: ἥλιος (*Oxford English Dictionary*, March 2012).

the corona's large scale height, it remained unclear why or how the corona could achieve temperatures hundreds or thousands of times hotter than the photosphere.

1.1.2 Early Indications of the Solar Wind

As important discoveries were being made about the solar corona, evidence was also mounting that solar material penetrated even deeper into space. Of course, for centuries, the tails of comets had been observed to extend away from the Sun (versus anti-parallel to the comet's trajectory). Cometary tails are now understood to result largely from the solar wind (Biermann, 1951; Zirin, 1966), which streams from the corona into deep space, but this conclusion was not immediately evident. Kepler (1619) had proposed that they were caused by the radiation pressure of sunlight (per the now-defunct corpuscular theory of light), and Olbers (1812) suggested that they arise from the Sun having a net charge (Tiersch & Notni, 1989; McInnes, 1999; Heidarzadeh, 2008).

One of history's most dramatic and influential examples of the Earth-Sun connection came when Carrington (1859) and Hodgson (1859) simultaneously and independently observed an intense solar flare originate from a cluster of sunspots. In describing the event, Hodgson (1859) wrote

> While observing a group of solar spots on the 1st September, I was suddenly surprised at the appearance of a very brilliant star of light, much brighter than the sun's surface, most dazzling to the protected eye, illuminating the upper edges of the adjacent spots and streaks, not unlike in effect the edging of the clouds at sunset; the rays extended in all directions; and the centre might be compared to the dazzling brilliancy of the bright star α *Lyræ* when seen in a large telescope with low power. It lasted for some five minutes, and disappeared instantaneously about 11.25 A.M.

Less than a day after this solar flare, Earth was embroiled in an intense geomagnetic storm.

Ground observations (e.g., from Kew Observatory) revealed heavy distortions in Earth's magnetic field, telegraphic communications were disrupted around the world, and the aurora borealis was observed as far south as the Caribbean (Boteler, 2006, and contemporary references therein). *The New York Times* (3 September 1859) printed the following description of the auroral activity as seen from New York City:

> Streamers of yellow and orange shot up and met and crossed each other, like the bayonets upon a stack of guns, in the open space between the constellations Aries, Taurus and the Head of Medusa — about fifteen degrees south of the zenith. In this manner — alternating great pillars, rolling cumuli, shooting streamers, curdled and wisped and fleecy waves — rapidly changing its hues from red to orange, orange to yellow, and yellow to white, and back in the same order to brilliant red, the magnificent auroral glory continued its grand and inexplicable movements until the light of morning overpowered its radiance and it was lost in the beams of the rising sun.

Shortly afterward, some researchers, especially Stewart (1861), proposed a direct connection between the solar flare and the geomagnetic storm (Alexander, 2005).

The discovery of the solar wind and the birth of modern heliophysics are usually credited to Parker (1958). Chapman (1957) developed a model for the corona as a static atmosphere (i.e., one with no inward or outward flow). However, the high coronal temperatures indicated by spectroscopy meant that the corona was highly conductive. In Chapman's model, this accounted for the corona's large scale height, but it prevented the corona from achieving hydrostatic equilibrium (i.e., the gas pressure did not tend to zero at an infinite distance from the Sun) (Zirin, 1966). To resolve this contraction, Parker (1958), building upon the work of Biermann (1951), introduced a model for the corona that included the radially outward flow of coronal material: a solar wind. Direct observational evidence for the solar wind came from Neugebauer & Snyder (1962), who, using the *Mariner 2* spacecraft, identified a continually-flowing solar wind with typical speeds between 400 and 700 km/s.

1.2 Background Information

This section introduces key concepts that are used throughout this dissertation and can therefore be considered an augmentation of the outline provided in Section 1.3.

1.2.1 The Solar Wind as a Plasma Physics Laboratory

The exact cause of the solar corona's extremely high temperatures remains unknown. However, as was first shown by Parker (1958), these temperatures would prevent a static corona from maintaining pressure balance with the interstellar medium, and therefore give rise to the supersonic outflow of the solar wind (Hundhausen, 1972; Burlaga, 1995; Golub & Pasachoff, 1997; Velli, 2001).

As measured near Earth (i.e., 1 AU from the Sun), the bulk flow of the solar wind is typically nearly-radial and at a speed between 250 and 900 km/s. The background magnetic field strength is generally about 5 nT, and the ion number density usually falls between about 1 and 10 cm^{-3}. The vast majority of these particles protons (i.e., ionized hydrogen atoms) and α-particles (i.e., fully ionized helium atoms). Protons are always the more abundant component: though the fraction of α-particles (by number density) can be as high as 0.2, it is most often between 0.01 and 0.05 (Schwenn, 1990; Kasper et al., 2007).

In astrophysical terms, the physical conditions of the solar wind are not unusual. On the contrary, hot, low-density, magnetized plasmas exist in a variety of environments including the interstellar medium, the intergalactic medium, and accretion disks (Schekochihin et al., 2009). However, solar wind is distinct in that it provides the only opportunity for these types of plasma conditions to be studied in situ (i.e., through direct measurements versus remote

observations). No other, similar astrophysical environment is accessible to spacecraft, and such low-density plasmas cannot be produced in laboratories. In this sense, the the solar wind provides a unique "laboratory" for studying the microkinetics of not only heliospheric plasma but of astrophysical plasmas in general. There is mounting evidence that these small-scale phenomena have significant effects on macroscopic processes (e.g., acceleration and heating) in the solar wind (Hollweg & Isenberg, 2002; Markovskii & Hollweg, 2004; Matteini et al., 2007; Mecheri & Marsch, 2008) as well as in extrasolar plasmas (Schekochihin & Cowley, 2006; Sharma et al., 2006).

1.2.2 Temperature Anisotropy

The physical conditions described above ensure remarkably low rates of particle collisions in solar wind plasma. Consequently, rather than being characterized as a fluid with a single temperature and bulk velocity, the solar wind is more accurately analyzed by considering the velocity distribution function (VDF), f_j, of each particle species j (where $j = p$ for protons, α for α-particles, and e for electrons). The function $f_j(\mathbf{u})$ essentially specifies the relative occurrence of j-particles with velocity $\mathbf{u}$ and is defined such that its zeroth, first, and second moments are

$$\begin{aligned} \int_{\forall \mathbf{u}} d^3u\, f_j(\mathbf{u}) &= n_j \ , \\ \int_{\forall \mathbf{u}} d^3u\, \mathbf{u}\, f_j(\mathbf{u}) &= n_j\, \mathbf{v}_j \ , \text{ and} \\ \int_{\forall \mathbf{u}} d^3u\, u^2\, f_j(\mathbf{u}) &= n_j \left(v_j^2 + w_j^2\right) \ , \end{aligned} \tag{1.1}$$

where n_j is the number density of species j, $\mathbf{v}_j$ is its bulk velocity, and w_j is its root-mean-square (RMS) thermal speed[2]. The temperature of species j is defined to be

$$T_j = \frac{m_j\, w_j^2}{k_B} \ , \tag{1.2}$$

where m_j is the mass of a j-particle. In thermal equilibrium, $\mathbf{v}_j$ and T_j would each be the same for all species j, but, as stated above, this is rarely observed in the solar wind due largely to its low collisionality (Kasper et al., 2008).

The presence of a background magnetic field, $\mathbf{B}_0$, in the solar wind creates direction-dependent transport coefficients (Stix, 1992). Essentially, this gives rise to heating and cooling processes that act preferentially either perpendicularly or parallel to $\mathbf{B}_0$. Consequently, each particle species j typically exhibits some degree of temperature anisotropy: i.e., spherical asymmetry in its VDF. This can be interpreted as the species having a temperature, $T_{\perp j}$, along the axes perpendicular to $\mathbf{B}_0$ that is distinct from its temperature, $T_{\parallel j}$, along the axis parallel to $\mathbf{B}_0$ (see Section 1.2.3 for a more complete model of an anisotropic VDF). The scalar temperature[3] of species j is then

$$T_j = \left(2\, T_{\perp j} + T_{\parallel j}\right) / \, 3 \ , \tag{1.3}$$

and its temperature anisotropy is typically quantified by the ratio

$$R_j = \frac{T_{\perp j}}{T_{\parallel j}} = \frac{w_{\perp j}^2}{w_{\parallel j}^2} \ . \tag{1.4}$$

---

[2]The *root-mean-square* thermal speed differs from the *most-probable* thermal speed, which is larger by a factor of $\sqrt{2}$.

[3]The term *scalar temperature* is customarily used this way in the literature. Nevertheless, it is technically erroneous as $T_{\perp j}$ and $T_{\parallel j}$ cannot be used to define a "vector temperature" in a way that is consistent with the axioms of vector spaces.

Spectroscopic measurements of the solar corona indicate that, for minor ions (e.g., oxygen), the R_j-values therein typically range from 10 to 20 (Cranmer et al., 2008), which suggests that temperature anisotropy plays an important role in coronal heating (Isenberg & Hollweg, 1983; Cranmer, 2001; Marsch & Tu, 2001; Isenberg & Vasquez, 2007). However, the temperature anisotropy of protons and α-particles at 1 AU from the Sun usually falls between 0.1 and 10.

Numerous anisotropic heating and cooling processes have been found to affect the solar wind as it streams outward from the corona. The most frequently cited anisotropic cooling mechanism is CGL double adiabatic expansion (Chew et al., 1956), which causes $T_{\perp j}$ to decrease more quickly than $T_{\parallel j}$ as the plasma expands. This phenomenon can partially account for the observed trend in R_p as a function of distance from the Sun (Marsch & Richter, 1984; Matteini et al., 2007) and for the extreme temperature anisotropies encountered in the lunar wake (Clack et al., 2004). Conversely, perpendicular heating has been associated with the cyclotron-resonant absorption of Alfvén waves (Marsch & Tu, 2001; Hollweg & Isenberg, 2002; Kasper et al., 2007). Likewise, studies have identified the Landau damping of kinetic Alfvén waves as a source both of perpendicular heating (Sahraoui et al., 2009, 2010) and of parallel heating (Quataert, 1998; Schekochihin et al., 2009; Chandran et al., 2010).

1.2.3 The Bi-Maxwellian VDF

The VDF's observed in the solar wind are typically quite complex. However, for the study of ion temperature anisotropy, it is generally sufficient to use a bi-Maxwellian distribution, which (for a species j) is defined to be

$$f_j^{(b)}(\mathbf{u}) = \frac{n_j}{(2\pi)^{3/2}\ w_\perp^2\ w_\parallel} \exp\left(-\frac{\left|\mathbf{u}_\parallel - \mathbf{v}_{\parallel j}\right|^2}{2\, w_{\parallel j}^2} - \frac{\left|\mathbf{u}_\perp - \mathbf{v}_{\perp j}\right|^2}{2\, w_{\perp j}^2} \right) , \tag{1.5}$$

where $w_{\perp j}$ and $w_{\parallel j}$ denote the perpendicular and parallel RMS thermal speeds, respectively. In particular,

$$w_{\perp j} = \sqrt{\frac{k_B\, T_{\perp j}}{m_j}}\ , \qquad \text{and} \qquad w_{\parallel j} = \sqrt{\frac{k_B\, T_{\parallel j}}{m_j}}\ . \tag{1.6}$$

The perpendicular and parallel projections of $\mathbf{u}$ (or any vector quantity) can be expressed as

$$\mathbf{u}_\parallel = \left(\mathbf{u}\cdot\hat{\mathbf{B}}_0\right)\hat{\mathbf{B}}_0\ , \qquad \text{and} \qquad \mathbf{u}_\perp = \mathbf{u} - \mathbf{u}_\parallel = \mathbf{u}\times\hat{\mathbf{B}}_0\ , \tag{1.7}$$

respectively.

In part, the bi-Maxwellian model works well for ions in the solar wind because, while the VDF of an ion species is generally anisotropic, it is almost always gyrotropic (i.e., is symmetric about $\hat{\mathbf{B}}_0$). Gyrotropy develops relatively rapidly — typically in about one cyclotron period, $2\,\pi\,/\,\Omega_j$, where

$$\Omega_j = \frac{q_j\, B_0}{m_j}\ , \tag{1.8}$$

is the cyclotron (angular) frequency of species j and q_j is the charge of a j-particle. Under typical conditions in the solar wind, $\Omega_p \sim 1$ Hz, so the plasma is typically only observed to deviate from gyrotropy during periods of particularly extreme and rapid changes. Locations where spacecraft occasionally encounter non-gyrotropic distributions include planetary magnetosheaths (Lacombe et al., 1995) and the interaction region between the solar wind and comet tails (Motschmann & Glassmeier, 1993). These plasmas are distinguished from normal solar wind by the significant degree to which they evolve on timescales shorter than the gyroscale.

Of course, temperature anisotropy can only develop in the presence of a background magnetic field, which restricts the flow of thermal energy in the perpendicular directions.

The degree to which a species j is influenced by this magnetic field can be quantified by

$$\beta_{\parallel j} = \frac{n_j \, k_B \, T_{\parallel j}}{B_0^2 \, / \, (2 \, \mu_0)} \; , \tag{1.9}$$

which is the ratio of the parallel pressure of the j-particles to the magnetic pressure. Essentially, $\beta_{\parallel j}$ gauges how much effect the magnetic field has on the behavior and evolution of species j. Since the solar wind has an extremely high electrical conductivity (Hundhausen, 1972), the magnetic field and particles therein are essentially locked together. When $\beta_{\parallel j} \ll 1$, the magnetic field has more energy in it than the j-particles do in their thermal motion, so the field primarily controls the evolution of the plasma and drags the particles along with it. However, when $\beta_{\parallel j} \gg 1$, the magnetic field follows the cue of the particles since they have more of the plasma's energy.

Because, by mass density, protons are the dominant particle species in the solar wind, the value of $\beta_{\parallel p}$ can be interpreted in another way. In particular,

$$\beta_{\parallel p} \approx \left(\frac{\sqrt{2} \, w_{\parallel p}}{c_A} \right)^2 \; , \tag{1.10}$$

where

$$c_A = \frac{B_0}{\sqrt{\mu_0 \, \sum_{\forall j} m_j \, n_j}} \approx \frac{B_0}{\sqrt{\mu_0 \, m_p \, n_p}} \; , \tag{1.11}$$

is the Alfvén speed, which is the speed at which Alfvén waves propagate through the plasma. Likewise, $\sqrt{2} \, w_{\parallel p}$ is approximately the speed of sound waves (at least those propagating parallel to the magnetic field). Thus, $\beta_{\parallel p}$ approximates the relative propagation speeds of these two types of waves. In highly magnetized plasma, $\beta_{\parallel p} \ll 1$, so Alfvén waves propagate more quickly than sound waves. However, when $\beta_{\parallel p} \gg 1$, sound waves propagate faster.

1.2.4 Particle Collision Rates and Collisional Age

As stated above, the low densities and high temperatures of the solar wind ensure that, by terrestrial standards, the rates of Coulomb collisions among particles remain very low. Particle collisions play an important role in establishing thermal equilibrium in a fluid, so the observed non-thermal features of solar wind plasma (e.g., temperature anisotropy and differential flow) are a direct consequence of weak collisionality.

The collisional timescale quantifies the characteristic length of time necessary for a given parcel of plasma to be significantly effected by particle collisions. Numerous definitions exist for this parameter because collisions erode different non-equilibrium features at different rates. For the purposes of this thesis project, though, it was sufficient to consider the "self-collision time" of an ion species j (Spitzer, 1956):

$$\tau_j = (11.4 \text{ s}) \left(\frac{1}{\ln \Lambda_j} \right) \left(\frac{m_j}{m_p} \right)^{1/2} \left(\frac{q_j}{q_p} \right)^{-4} \left(\frac{n_j}{1 \text{ cm}^{-3}} \right)^{-1} \left(\frac{T_j}{1 \text{ K}} \right)^{3/2} , \tag{1.12}$$

where

$$\Lambda_j = \left(\frac{12\,\pi}{q_p\, q_j^2} \right) \left(\frac{\epsilon_0^3\, k_B^3\, T_j^3}{n_j} \right)^{1/2} , \tag{1.13}$$

is the plasma parameter (i.e., the argument of the Coulomb logarithm, $\ln \Lambda_j$).

Since the ion population of the solar wind is dominated by protons, it is possible to define the collisional age of a parcel of solar wind plasma to be

$$A_c = \frac{D}{\tau_p\, v_p} , \tag{1.14}$$

where D is the distance of the observer from the Sun. Essentially, A_c is the number of proton self-collision times that elapsed as the parcel traveled from the solar corona to the observer. This interpretation tacitly assumes that, for the plasma's entire journey, τ_p and $\mathbf{v}_p$

are constant and $\mathbf{v}_p$ is radial. Fortunately, though, observations in the inner heliosphere with the *Helios* spacecraft have revealed that these parameters' variations with distance from the Sun are less significant than their temporal variations (Marsch et al., 1982; Marsch, 1991).

In situ measurements of the solar wind at $D = 1$ AU have shown that several indicators of plasma equilibrium are strongly correlated with A_c (Kasper et al., 2008). For example, in collisionally old plasma (i.e., that with $A_c \gg 1$), significant departures from ion temperature isotropy and temperature equilibrium are rare. However, such deviations are commonly present in collisionally young plasma (i.e., that with $A_c \ll 1$). Near Earth, the value of A_c typically ranges from 0.01 to 100., which makes this location an excellent laboratory for the exploration of collisional effects in astrophysical plasmas.

1.2.5 Ion Temperature Anisotropy Instabilities

In plasma, non-Maxwellian VDF's and departures from thermal equilibrium are entropically unfavorable as they provide a source of free energy. Therefore, in the absence of some sustaining process, these features are eventually eroded, and the medium enters equilibrium. As stated in Section 1.2.4, Coulomb collisions play a large role in this process in the solar wind, but, in collisionally young solar wind, kinetic microinstabilities can also contribute. Such an instability is triggered when the plasma departs so far from equilibrium that the amplitudes of certain waves begin to grow exponentially. The resulting enhanced fluctuations scatter particles in phase space and force the plasma closer to equilibrium.

Anisotropy-driven instabilities are the subset of kinetic microinstabilities that result from $R_j \neq 1$. Both electron and ion temperature anisotropy can cause plasma to become unstable, but the instabilities driven by each have very different properties (Gary, 1993).

Consequently, this thesis project focused only on ion temperature anisotropy instabilities.

Instabilities driven by proton temperature anisotropy (i.e., by $R_p \neq 1$) have been studied extensively and found to have a strong effect on the observed distribution of R_p-values in the solar wind. The actions of the cyclotron instability in limiting $R_p > 1$ and of the parallel firehose instability in limiting $R_p < 1$ have both received extensive theoretical and observational analysis (Gary et al., 1994, 1998, 2001; Kasper et al., 2002). However, more-recent, larger-scale studies have suggested that the mirror instability may be more active in limiting $R_p > 1$ while the oblique firehose instability may be more active in limiting $R_p < 1$ (Hellinger et al., 2006; Bale et al., 2009).

As stated above, this thesis project focused on ion temperature anisotropy instabilities in the solar wind. In particular, the analysis of data from the *Wind* spacecraft's Faraday cups and calculations from linear Vlasov theory were used together to build upon these existing results for proton instabilities and to extend them to the corresponding α-particle instabilities, which have received far less attention in the literature (see Section 7.1).

1.3 Summary of This Dissertation

Including this introduction (i.e., Chapter 1), this dissertation contains a total of nine chapters.

The in situ measurements of the solar wind that were used in this thesis project came primarily from the *Wind* spacecraft's Faraday cups (*Wind*/FC), which are described in Chapter 2. Chapter 3 reports how *Wind*/FC "ion spectra" were analyzed, and Chapter 4 details how a dataset of the highest-quality spectra was compiled for this study.

Chapter 5 introduces the analysis of ion temperature anisotropy instabilities with linear Vlasov theory. This discussion includes the derivation of analytic results as well as a description of the software used in this project to calculate the growth rates of these instabilities.

Chapters 6 and 7 focus respectively on proton and α-particle temperature anisotropy instabilities. Each reports on the analysis of the dataset detailed in Chapter 4 with the software described in Chapter 5. Chapter 8 describes an extension of the work reported in Chapter 6 and explores the connection between proton instabilities and heat flow in the solar wind.

The general conclusions of this dissertation are presented in Chapter 9, which includes a summary of key results and a brief discussion of possible continuations of this thesis project.

Appendix A provides information about the notation and typographical conventions used in this dissertation. Its principal mathematical symbols are listed in Appendix B.

Chapter 2

The *Wind* Faraday Cups

The observations used in this thesis project came primarily from the *Wind* spacecraft's Faraday cups (*Wind*/FC). Section 2.1 briefly overviews the motivations for the *Wind* spacecraft and the purpose of its Faraday cups. Section 2.2 describes the typical design of Faraday cups used for in situ measurements of space plasma, and Section 2.3 provides a more quantitative analysis of their operation and performance. A conceptual overview of a *Wind*/FC *ion spectrum* is given in Section 2.4, but a full discussion of processing these spectra is reserved for Chapter 3.

2.1 Introduction to the *Wind* Spacecraft

The *Wind* spacecraft was launched on November 1, 1994 to explore the Earth's magnetosphere and the solar wind (Acuña et al., 1995). Along with the *Polar* spacecraft, *Wind* was a part of the NASA Global Geospace Science (GGS) Program, which coordinated in situ measurements of space environments with Earth-based remote observations and theoretical

investigations. In turn, the GGS Program was part of the International Solar Terrestrial Physics (ISTP) Program, which oversaw a multinational collaboration studying the Earth-Sun system.

For its first decade of operation, *Wind* traveled widely and spent time near Earth, the Moon, and the first and second Lagrangian points (L1 and L2, respectively). *Wind* has since been positioned at L1, where it is slated to stay for the remainder of its mission.

As is evident from the diagram in Figure 2.1, the *Wind* spacecraft's body is cylindrical (Harten & Clark, 1995). *Wind* is a spin-stabilized spacecraft and rotates about its axis with a period of approximately 3 seconds. The spacecraft is kept oriented such that its spin axis is perpendicular to the ecliptic plane.

The observational investigations described in this dissertation primarily used ion measurements from the *Wind* spacecraft's two Faraday cups, which are part of the Solar Wind Experiment (SWE) thereon (Ogilvie et al., 1995). The *Wind* Faraday cups (*Wind*/FC) were designed to collect solar wind plasma and to measure directly the basic properties of its ions (e.g., density). The cups are located on opposite sides of the spacecraft body, and each is tilted slightly out of the ecliptic plane: one 15° north and the other 15° south.

2.2 Faraday Cup Design and Operation Principles

Essentially, a Faraday cup is a metal shell (typically cylindrical) with an aperture through which plasma particles pass onto a plate called the *collector*, which is kept electrically isolated from the metal shell. The collector is connected to ground via a detection circuit that measures the current generated by the charged particles striking the plate.

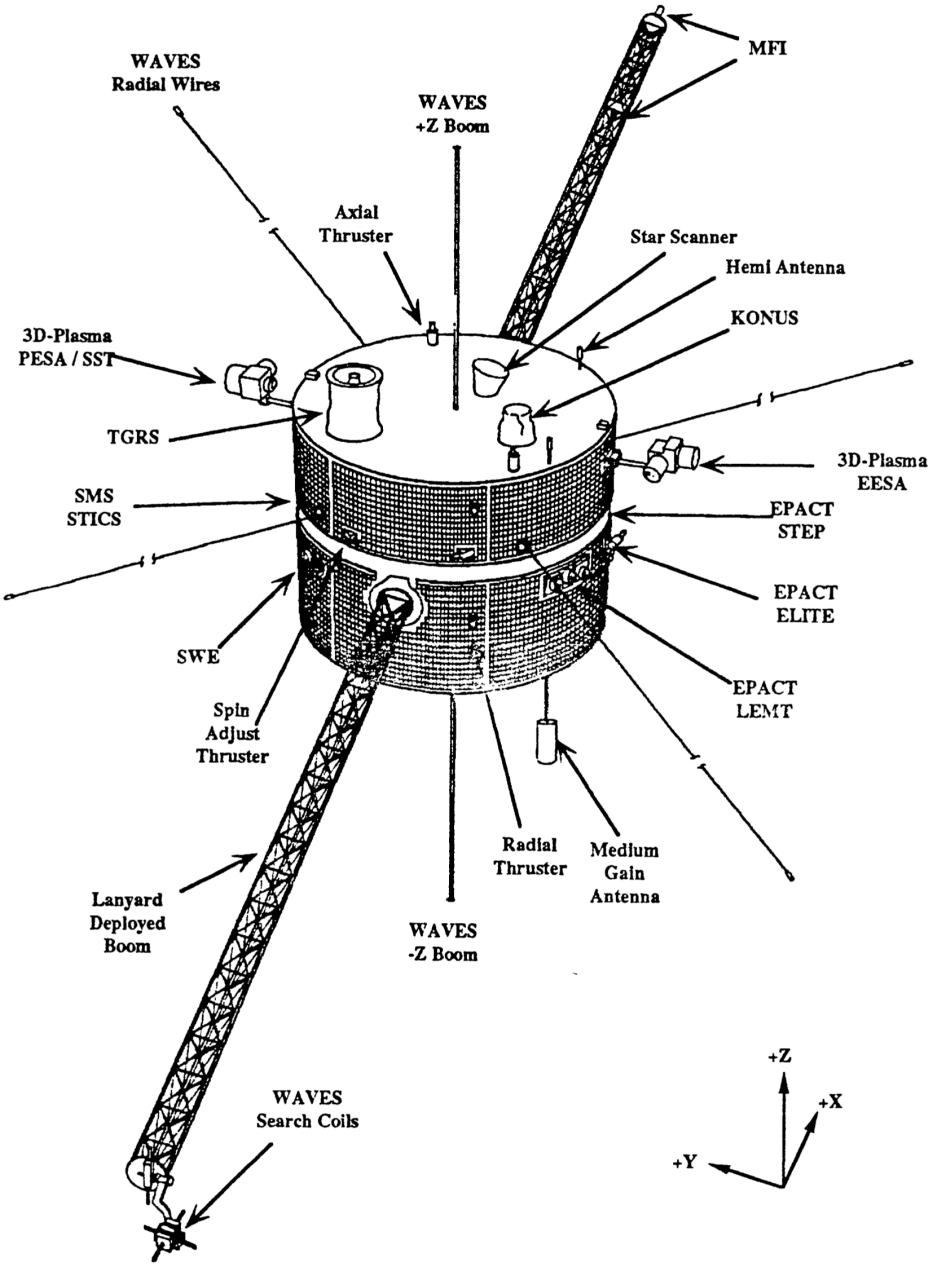

Figure 2.1.— Diagram of the *Wind* spacecraft published by Harten & Clark (1995).

In the simplest design of a Faraday cup, any particle that is incident on the cup's aperture is allowed to enter (regardless of its mass, charge, and inflow speed) and the detection circuit is just an ammeter. Then, the measured current indicates the net charge flux from the inflowing plasma particles. Such a design is useful in some laboratory settings (e.g., for the calibration of ion beams), but it has limited applications to space science. First, since the solar wind is charge neutral (on scales larger than the Debye length) (Spitzer, 1956), the currents from its electrons and ions would mostly cancel each other. Second, this design provides no mechanism for discriminating among particles of different species or energies. Consequently, composition cannot be measured, the particle number density and bulk speed remain inextricably coupled, and no determination of temperature can be made.

In order to overcome these limitations, a Faraday cup for space science research typically has a system of grids between its aperture and collector. Figure 2.2 shows a cross-sectional diagram of a Faraday cup with three such grids. Both the outer grid and the inner grid are electrically grounded, but the middle grid, known as the *modulator*, is allowed to have a non-zero voltage. If the modular voltage is positive, all electrons flowing into the cup are allowed to enter, but only ions with sufficient inflow speed are able to do so. Likewise, if the modulator voltage is negative, all ions can enter but electrons that are entering too slowly are deflected.

Because the Faraday cup in Figure 2.2 (like the *Wind* Faraday cups) is intended to measure ions, its modulator voltage is kept non-negative. One mode of operation would be to apply various DC modulator voltages and to measure the collector current for each. If the cup is fixed in space and plasma conditions are static, then the measured collector current should decrease as the modulator voltage increases. The exact trend in collector current versus modulator voltage can thus be used to deduce information about the distribution of

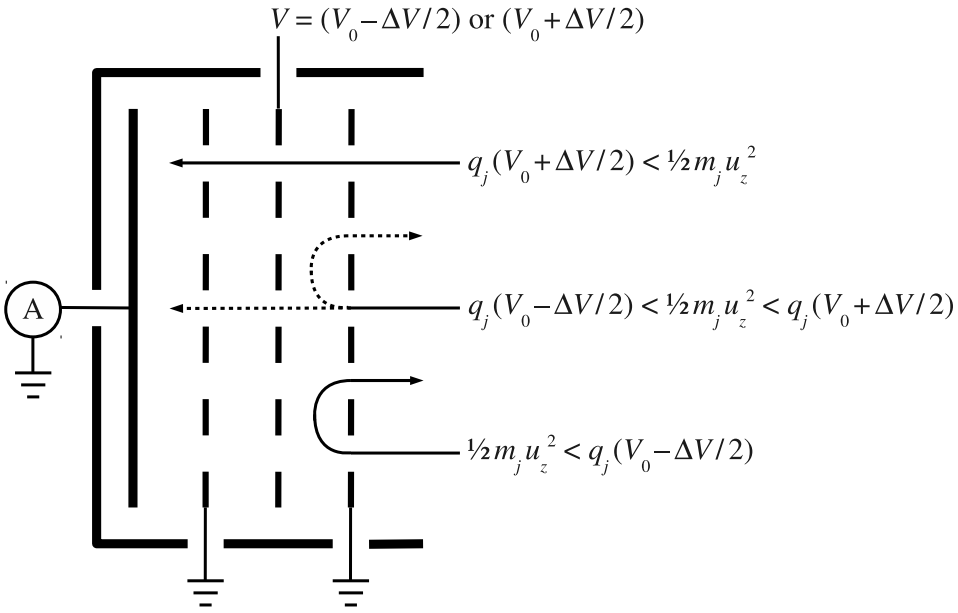

Figure 2.2.— Cross-sectional diagram of a Faraday cup with a square-wave modulator voltage for the measurement of ions. The cup's aperture is on the right, its collector plate is on the left, and its three grids are indicated by dashed lines. The interaction of a j-ion with velocity $\mathbf{u}$ is considered. To ensure that the ion enters the cup, it is implicitly assumed that $u_z < 0$ (where $\hat{\mathbf{z}}$ is the pointing direction of the cup). For simplicity, the two other components of $\mathbf{u}$ are neglected in this diagram. The arrows indicate the three possible types of trajectories that the ion can take. If u_z satisfies the criterion for the lower trajectory, the particle is always deflected by the modulator. Conversely, if u_z meets the upper criterion, it always goes past the modulator and onto the collector plate. However, if u_z satisfies the middle criterion, the particle is rejected when the modulator voltage is high and accepted when it is low.

ion energies.

While this use of DC modulator voltages allows for a relatively simple measurement scheme, it is highly sensitive to sources of background current. As mentioned above, a positive modulator voltage means that all incident electrons from the plasma are allowed to enter the cup. However, ultraviolet photons and other types of radiation generate additional electrons as they strike the instrument. At 1 AU from the Sun, the current from all these electrons can easily dwarf that of particles from solar wind plasma.

To mitigate the effects of background noise, most Faraday cups used in space environments employ an AC modulator voltage and a synchronous detection circuit that is similar in concept to a lock-in amplifier. In many cases (including that of the *Wind* Faraday cups), a square wave is used for the modulator voltage. Figure 2.2 shows the modulator voltage, V, alternating between

$$V = (V_0 - \Delta V/2) \text{ and } (V_0 + \Delta V/2) \ , \tag{2.1}$$

where V_0 is the DC offset of the square wave and ΔV is its peak-to-peak amplitude[1]. This figure also considers an ion of mass $m_j > 0$ and charge $q_j > 0$ flowing into the cup. The $\hat{\mathbf{z}}$-direction is taken to be the pointing direction of the cup, and u_z denotes the z-component of the particle's velocity[2]. The voltage difference between the outer grid and the modulator creates an electric field between them that exerts a force on the ion in the $\hat{\mathbf{z}}$-direction. Then, depending on the value of u_z, the ion's trajectory will fall into one of three basic categories.

[1]Of course, in order to maintain a non-negative modulator voltage, it is tacitly assumed that $0 \leq \Delta V \leq 2\,V_0$.

[2]For the particle to actually flow into the cup, it must hold that $u_z < 0$.

First, if u_z is such that

$$m_j \, u_z^2 \, / \, 2 \, < \, q_j \, (V_0 - \Delta V/2) \ , \tag{2.2}$$

then (regardless of whether V is in the high or low state) the electric field always reverses the trajectory of the particle and thereby prevents it from reaching the collector. Second, if u_z is such that

$$q_j \, (V_0 + \Delta V/2) \, < \, m_j \, u_z^2 \, / \, 2 \ , \tag{2.3}$$

then the electric field slows down but can never stop the incoming particle from reaching the modulator. Because the inner grid is grounded, such a particle, after passing the modulator, is accelerated back to its original inflow speed before it strikes the collector. The third and final case is that of u_z satisfying

$$q_j \, (V_0 - \Delta V/2) \, < \, m_j \, u_z^2 \, / \, 2 \, < \, q_j \, (V_0 + \Delta V/2) \ . \tag{2.4}$$

For this range of u_z-values, the modulator repels the particle when its voltage is in the high state but not when its voltage is in the low state.

For Faraday cups with square-wave modulator voltages, the detector typically contains a demodulation and integration circuit that is sensitive to the difference between the collector current when V is low and that when V is high (Kasper, 2002). More specifically, the AC-coupling and synchronization of the detector to the modulator voltage means that the measured quantity is the half of the average value of this difference in current. As is shown more explicitly in Section 2.3, the factor of one half is present because the ions satisfying Equation 2.4 can only reach the collector half of the time (i.e., when V is in the low state). The currents from other ions, solar wind electrons, and photoelectrons are automatically excluded because they produce a DC signal at the collector.

2.3 Theoretical Response of an Ideal Faraday Cup

This section extends Section 2.2 by presenting a more analytic discussion of an ideal Faraday cup with a square-wave modulator voltage and synchronous detection. In particular, it derives the theoretical response of such an instrument to a plasma consisting of a single ion species j (with mass $m_j > 0$, charge $q_j > 0$, and VDF f_j). Throughout this section, the ion VDF is assumed to be homogeneous and static (i.e., that f_j is independent of space and time). As above, the Faraday cup is assumed to be stationary and, without the loss of generality, to be pointing in the $\hat{\mathbf{z}}$ direction.

The first of this section's three parts considers a completely arbitrary ion VDF. The second part adds the assumption that the ion bulk flow is supersonic, which allows the concept of the reduced VDF to be introduced. Finally, in the third part, the VDF is assumed to be a supersonic bi-Maxwellian.

2.3.1 Response for an Arbitrary VDF

As in the previous section, the modulator voltage is denoted V. The first portion of this derivation treats V as a constant, but then its results are generalized to the case where $V = V(t)$ is a square-wave. Nevertheless, because this hypothetical Faraday cup is for measuring ions, V is assumed to be non-negative at all times.

The Faraday cup's effective collecting area, A, accounts for the various geometric factors that affect the flow of particles into the instrument: e.g., the projected size of the aperture (in the particles' frame of reference) and the transparency of the grids. Consequently, A is a function of $\hat{u}_z = \hat{\mathbf{u}} \cdot \hat{\mathbf{z}}$ (i.e., the z-component of the normalized particle velocity $\hat{\mathbf{u}}$).

Typically, when the particles are moving straight into the cup (i.e., when $\hat{u}_z = -1$), the effective collecting area is at its maximum and almost equals the geometric area of the cup's opening. Intuitively,

$$A(\hat{u}_z) = 0 \qquad \text{for} \qquad \hat{u}_z \geq 0 \ , \tag{2.5}$$

since particles should have some inward (versus outward) velocity component in order to enter the cup.

The expression

$$d^3u = du_x \, du_y \, du_z \ , \tag{2.6}$$

denotes an infinitesimal volume of velocity space centered at a given particle velocity $\mathbf{u}$. If $V = 0$, then the contribution of the particles in this volume to the collector current is

$$dI_j = -q_j \, u_z \, A(\hat{u}_z) \, f_j(\mathbf{u}) \, d^3u \ . \tag{2.7}$$

The negative sign in the above equation comes from the choice of coordinate system and simply reflects the convention that $u_z < 0$ for inflowing particles.

A non-negative modulator voltage, V, sets a threshold value for $-u_z$, below which the particles in d^3u create no collector current (since none passes the modulator grid), and above which they contribute the current specified in Equation 2.7. By conservation of energy, this cut-off speed is

$$u_j^{(c)}(V) = \sqrt{\frac{2 \, q_j \, V}{m_j}} \ . \tag{2.8}$$

Thus, for a constant voltage $V \geq 0$, the total collector current is

$$\begin{aligned} I_j(V) &= \int_{u_z < -u_j^{(c)}(V)} dI_j \\ &= -q_j \int_{-\infty}^{-u_j^{(c)}(V)} du_z \, u_z \int_{-\infty}^{\infty} du_y \int_{-\infty}^{\infty} du_x \, A(\hat{\mathbf{u}} \cdot \hat{\mathbf{z}}) \, f_j(\mathbf{u}) \ . \end{aligned} \tag{2.9}$$

In the above expression, the argument of the effective collecting area, A, has been written as $\hat{\mathbf{u}} \cdot \hat{\mathbf{z}}$ (versus $\hat{u}_z$) to emphasize that it depends on all three variables of integration (i.e., u_x, u_y, and u_z).

If instead the modulator voltage, V, is taken to be a square wave, then $V(t)$ can be parameterized as follows:

$$V(t) = \begin{cases} V_0 + \Delta V/2 & t \in [0, \tau_m/2) \\ V_0 - \Delta V/2 & t \in [\tau_m/2, \tau_m) \\ V(t \bmod \tau_m) & \text{else} \end{cases} , \tag{2.10}$$

where t is time, τ_m is the period of the modulator voltage, $V_0 > 0$ is its offset, and $\Delta V \in [0, 2V_0]$ is its peak-to-peak amplitude. Assuming that the collector current is detected synchronously, the demodulated (i.e., measured) current is

$$\begin{aligned} \Delta I_j &= \frac{1}{\tau_m} \left[\int_0^{\tau_m/2} dt \left(\overline{I}_j - I_j[V(t)] \right) + \int_{\tau_m/2}^{\tau_m} dt \left(I_j[V(t)] - \overline{I}_j \right) \right] \\ &= \frac{1}{\tau_m} \left(- \int_0^{\tau_m/2} dt \, I_j[V(t)] + \int_{\tau_m/2}^{\tau_m} dt \, I_j[V(t)] \right) , \end{aligned} \tag{2.11}$$

where

$$\overline{I}_j = \frac{1}{\tau_m} \int_0^{\tau_m} I_j[V(t)] \, dt , \tag{2.12}$$

is the mean current from the collector (Kasper, 2002). Substitution of Equations 2.9 and 2.10 into Equation 2.11 gives the demodulated current for a square-wave modulator voltage:

$$\begin{aligned} \Delta I_j &= \frac{1}{2} \left[I_j(V_0 - \Delta V \,/\, 2) - I_j(V_0 + \Delta V \,/\, 2) \right] \\ &= -\frac{q_j}{2} \int_{-u_j^{(c)}(V_0+\Delta V/2)}^{-u_j^{(c)}(V_0-\Delta V/2)} du_z \, u_z \int_{-\infty}^{\infty} du_y \int_{-\infty}^{\infty} du_x \, A(\hat{\mathbf{u}} \cdot \hat{\mathbf{z}}) \, f_j(\mathbf{u}) . \end{aligned} \tag{2.13}$$

2.3.2 Supersonic Flow and the Reduced VDF

The expression for ΔI_j in Equation 2.13 holds true for any VDF f_j. However, at 1 AU from the Sun, the solar wind is invariably highly-supersonic. Mathematically, this means that $v_j \gg w_j$ (where $\mathbf{v}_j$ is the bulk velocity of species j and w_j is its thermal speed; see Equation 1.1) so that $f_j(\mathbf{u})$ is sharply peaked near $\mathbf{u} = \mathbf{v}_j$. If A is a slowly varying function, then, to good approximation,

$$\Delta I_j = -\frac{q_j}{2} A(\hat{v}_{zj}) \int_{-u_j^{(c)}(V_0+\Delta V/2)}^{-u_j^{(c)}(V_0-\Delta V/2)} du_z \, u_z \int_{-\infty}^{\infty} du_y \int_{-\infty}^{\infty} du_x \, f_j(\mathbf{u}) \ . \tag{2.14}$$

This expression for ΔI_j can also be written as

$$\Delta I_j = -\frac{q_j}{2} A(\hat{v}_{zj}) \int_{-u_j^{(c)}(V_0+\Delta V/2)}^{-u_j^{(c)}(V_0-\Delta V/2)} du_z \, u_z \, F_{zj}(u_z) \ , \tag{2.15}$$

where

$$F_{zj}(u_z) = \int_{-\infty}^{\infty} du_y \int_{-\infty}^{\infty} du_x \, f_j(\mathbf{u}) \ , \tag{2.16}$$

is the "reduced VDF" (along the z-axis).

Intuitively, the moments of the reduced VDF, F_{zj}, should be closely connected to those of the VDF itself, f_j, (see Equation 1.1). The zeroth moment of F_{zj} is

$$\int_{-\infty}^{\infty} du_z \, F_{zj}(u_z) = \int_{-\infty}^{\infty} du_z \int_{-\infty}^{\infty} du_y \int_{-\infty}^{\infty} du_x \, f_j(\mathbf{u}) = n_j \ . \tag{2.17}$$

Thus, f_j and F_{zj} have the same zeroth moment: n_j. Likewise, the first moment of F_{zj} is

$$\begin{aligned} \int_{-\infty}^{\infty} du_z \, u_z \, F_{zj}(u_z) &= \int_{-\infty}^{\infty} du_z \int_{-\infty}^{\infty} du_y \int_{-\infty}^{\infty} du_x \, u_z \, f_j(\mathbf{u}) \\ &= \left[\int_{-\infty}^{\infty} du_z \int_{-\infty}^{\infty} du_y \int_{-\infty}^{\infty} du_x \, \mathbf{u} \, f_j(\mathbf{u}) \right] \cdot \hat{\mathbf{z}} \\ &= n_j \, v_{zj} \ , \end{aligned} \tag{2.18}$$

Therefore, the first moment of F_{zj} is simply the z-component of the first moment of f_j. The thermal speed, w_j, is defined such that the second moment of f_j is $n_j \left(w_j^2 + v_j^2 \right)$. By analogy,

w_{zj}, the effective thermal speed along the z-axis, is defined such that the second moment of F_{zj} is

$$\int_{-\infty}^{\infty} du_z \, u_z^2 \, F_{zj}(u_z) = n_j \left(w_{zj}^2 + v_{zj}^2 \right) \ . \tag{2.19}$$

In the special case of an isotropic VDF, the effective thermal speed along any axis equals w_j.

2.3.3 Response for a Supersonic Bi-Maxwellian VDF

If f_j is assumed to be bi-Maxwellian (i.e, it is assumed that $f_j = f_j^{(b)}$; see Equation 1.5) as well as supersonic, then, based on Equations 2.15 and 2.16, the demodulated current is

$$\Delta I_j^{(b)} = -\frac{q_j}{2} \, A(\hat{v}_{zj}) \int_{-u_j^{(c)}(V_0+\Delta V/2)}^{-u_j^{(c)}(V_0-\Delta V/2)} du_z \, u_z \, F_{zj}^{(b)}(u_z) \ , \tag{2.20}$$

and the reduced VDF is

$$F_{zj}^{(b)}(u_z) = \int_{-\infty}^{\infty} du_y \int_{-\infty}^{\infty} du_x \, f_j^{(b)}(\mathbf{u}) \ . \tag{2.21}$$

These integrals are more easily evaluated in the rest frame of the plasma than that of the Faraday cup. Mathematically, this corresponds to making the substitution

$$\mathbf{u}' = \mathbf{u} - \mathbf{v}_j \ . \tag{2.22}$$

Then, the demodulated current can be written as

$$\Delta I_j^{(b)} = -\frac{q_j}{2} \, A(\hat{v}_{zj}) \int_{-u_j^{(c)}(V_0+\Delta V/2)-v_{zj}}^{-u_j^{(c)}(V_0-\Delta V/2)-v_{zj}} du'_z \, (u'_z + v_{zj}) \, F_{zj}^{(b)}(u'_z + v_{zj}) \ , \tag{2.23}$$

where

$$F_{zj}^{(b)}(u'_z + v_{zj}) = \frac{n_j}{\sqrt{8\,\pi^3}\, w_{\perp j}^2 \, w_{\parallel j}} \int_{-\infty}^{\infty} du'_y \int_{-\infty}^{\infty} du'_x \exp\left(-\frac{u_\parallel'^2}{2\, w_{\parallel j}^2} - \frac{u_\perp'^2}{2\, w_{\perp j}^2} \right) \ . \tag{2.24}$$

By definition (see Equation 1.7),

$$\begin{aligned} u_{\parallel}'^2 &= \left(\mathbf{u}' \cdot \hat{\mathbf{B}}_0\right)^2 \\ &= u_x'^2\,\hat{B}_{x0}^2 + u_y'^2\,\hat{B}_{y0}^2 + u_z'^2\,\hat{B}_{z0}^2 \\ &\quad + 2\,u_x'\,u_y'\,\hat{B}_{x0}\,\hat{B}_{y0} + 2\,u_y'\,u_z'\,\hat{B}_{y0}\,\hat{B}_{z0} + 2\,u_z'\,u_x'\,\hat{B}_{z0}\,\hat{B}_{x0}\ , \end{aligned} \tag{2.25}$$

and consequently

$$\begin{aligned} u_{\perp}'^2 &= u'^2 - u_{\parallel}'^2 \\ &= u_x'^2\,\left(1-\hat{B}_{x0}^2\right) + u_y'^2\,\left(1-\hat{B}_{y0}^2\right) + u_z'^2\,\left(1-\hat{B}_{z0}^2\right) \\ &\quad - 2\,u_x'\,u_y'\,\hat{B}_{x0}\,\hat{B}_{y0} - 2\,u_y'\,u_z'\,\hat{B}_{y0}\,\hat{B}_{z0} - 2\,u_z'\,u_x'\,\hat{B}_{z0}\,\hat{B}_{x0}\ . \end{aligned} \tag{2.26}$$

Then, by substitution,

$$\begin{aligned} F_{zj}^{(b)}(u_z' + v_{zj}) = \frac{n_j}{\sqrt{8\,\pi^3}\,w_{\perp j}^2\,w_{\parallel j}} \exp\left[-u_z'^2\,\frac{\hat{B}_{z0}^2\,w_{\perp j}^2 + \left(1-\hat{B}_{z0}^2\right)w_{\parallel j}^2}{2\,w_{\perp j}^2\,w_{\parallel j}^2}\right] \\ \int_{-\infty}^{\infty} du_y' \exp\left[-u_y'^2\,\frac{\hat{B}_{y0}^2\,w_{\perp j}^2 + \left(1-\hat{B}_{y0}^2\right)w_{\parallel j}^2}{2\,w_{\perp j}^2\,w_{\parallel j}^2} - u_y'\,\frac{u_z'\,\hat{B}_{y0}^2\,\hat{B}_{z0}^2\left(w_{\perp}^2 - w_{\parallel}^2\right)}{w_{\perp}^2\,w_{\parallel}^2}\right] \\ \int_{-\infty}^{\infty} du_x' \exp\left[-u_x'^2\,\frac{\hat{B}_{x0}^2\,w_{\perp j}^2 + \left(1-\hat{B}_{x0}^2\right)w_{\parallel j}^2}{2\,w_{\perp j}^2\,w_{\parallel j}^2} - u_x'\,\frac{\hat{B}_{x0}\left(\hat{B}_{y0}\,u_y' + \hat{B}_{z0}\,u_z'\right)\left(w_{\perp}^2 - w_{\parallel}^2\right)}{w_{\perp}^2\,w_{\parallel}^2}\right]\ . \end{aligned} \tag{2.27}$$

Evaluating the u'_x-integral gives

$$
\begin{aligned}
F_{zj}^{(b)}(u'_z + v_{zj}) = \frac{n_j}{\sqrt{8\,\pi^3}\,w_{\perp j}^2\,w_{\parallel j}} \exp\left[-u_z'^2\,\frac{\hat{B}_{z0}^2\,w_{\perp j}^2 + \left(1-\hat{B}_{z0}^2\right)w_{\parallel j}^2}{2\,w_{\perp j}^2\,w_{\parallel j}^2}\right] \\
\int_{-\infty}^{\infty} du'_y \exp\left[-u_y'^2\,\frac{\hat{B}_{y0}^2\,w_{\perp j}^2 + \left(1-\hat{B}_{y0}^2\right)w_{\parallel j}^2}{2\,w_{\perp j}^2\,w_{\parallel j}^2}\right. \\
\left. - u'_y\,\frac{u'_z\,\hat{B}_{y0}^2\,\hat{B}_{z0}^2\left(w_\perp^2 - w_\parallel^2\right)}{w_\perp^2\,w_\parallel^2}\right] \\
w_{\perp j}\,w_{\parallel j}\sqrt{\frac{2\,\pi}{\hat{B}_{x0}^2\,w_{\perp j}^2 + \left(1-\hat{B}_{x0}^2\right)w_{\parallel j}^2}} \\
\exp\left(\frac{\hat{B}_{x0}^2\left[\hat{B}_{y0}\,u'_y + \hat{B}_{z0}\,u'_z\right]^2\left[w_\perp^2 - w_\parallel^2\right]^2}{2\,w_\perp^2\,w_\parallel^2\left[\hat{B}_{x0}^2\,w_{\perp j}^2 + \left(1-\hat{B}_{x0}^2\right)w_{\parallel j}^2\right]}\right)\,,
\end{aligned}
\tag{2.28}
$$

which reduces to

$$
\begin{aligned}
F_{zj}^{(b)}(u'_z + v_{zj}) = \frac{n_j}{2\,\pi\,w_{\perp j}\sqrt{\hat{B}_{x0}^2\,w_{\perp j}^2 + \left(1-\hat{B}_{x0}^2\right)w_{\parallel j}^2}} \\
\exp\left(-u_z'^2\,\frac{\left(1-\hat{B}_{y0}^2\right)w_{\perp j}^2 + \hat{B}_{y0}^2\,w_{\parallel j}^2}{2\,w_{\perp j}^2\left[\hat{B}_{x0}^2\,w_{\perp j}^2 + \left(1-\hat{B}_{x0}^2\right)w_{\parallel j}^2\right]}\right) \\
\int_{-\infty}^{\infty} du'_y \exp\left(-u_y'^2\,\frac{\left[1-\hat{B}_{z0}^2\right]w_{\perp j}^2 + \hat{B}_{z0}^2\,w_{\parallel j}^2}{2\,w_{\perp j}^2\left[\hat{B}_{x0}^2\,w_{\perp j}^2 + \left(1-\hat{B}_{x0}^2\right)w_{\parallel j}^2\right]}\right. \\
\left. - u'_y\,\frac{u'_z\,\hat{B}_{y0}\,\hat{B}_{z0}\left[w_\perp^2 - w_\parallel^2\right]}{w_{\perp j}^2\left[\hat{B}_{x0}^2\,w_{\perp j}^2 + \left(1-\hat{B}_{x0}^2\right)w_{\parallel j}^2\right]}\right)\,.
\end{aligned}
\tag{2.29}
$$

The evaluation of the remaining integral gives

$$
\begin{aligned}
F_{zj}^{(b)}(u'_z + v_{zj}) = & \frac{n_j}{2\,\pi\,w_{\perp j}\,\sqrt{\hat{B}_{x0}^2\,w_{\perp j}^2 + \left(1 - \hat{B}_{x0}^2\right) w_{\| j}^2}} \\
& \exp\left(-u_z'^2\,\frac{\left[1 - \hat{B}_{y0}^2\right] w_{\perp j}^2 + \hat{B}_{y0}^2\,w_{\| j}^2}{2\,w_{\perp j}^2\left[\hat{B}_{x0}^2\,w_{\perp j}^2 + \left(1 - \hat{B}_{x0}^2\right) w_{\| j}^2\right]} \right) \\
& \sqrt{\frac{2\,\pi\,w_{\perp j}^2\left[\hat{B}_{x0}^2\,w_{\perp j}^2 + \left(1 - \hat{B}_{x0}^2\right) w_{\| j}^2\right]}{\left(1 - \hat{B}_{z0}^2\right) w_{\perp j}^2 + \hat{B}_{z0}^2\,w_{\| j}^2}} \\
& \exp\left(\frac{u_z'^2\,\hat{B}_{y0}^2\,\hat{B}_{z0}^2}{2\,w_{\perp j}^2\left[\hat{B}_{x0}^2\,w_{\perp j}^2 + \left(1 - \hat{B}_{x0}^2\right) w_{\| j}^2\right]} \right. \\
& \left. \frac{\left[w_\perp^2 - w_\|^2\right]^2}{\left(1 - \hat{B}_{z0}^2\right) w_{\perp j}^2 + \hat{B}_{z0}^2\,w_{\| j}^2} \right) .
\end{aligned}
\tag{2.30}
$$

This expression simplifies considerably to

$$
F_{zj}^{(b)}(u'_z + v_{zj}) = \frac{n_j}{\sqrt{2\,\pi}\,w_{zj}} \exp\left[-\frac{1}{2}\left(\frac{u'_z}{w_{zj}^{(b)}} \right)^2 \right] , \tag{2.31}
$$

where

$$
w_{zj}^{(b)} = \sqrt{\left(1 - \hat{B}_{z0}^2\right) w_{\perp j}^2 + \hat{B}_{z0}^2\,w_{\| j}^2} , \tag{2.32}
$$

is the effective thermal speed of species j along the z-axis for a bi-Maxwellian VDF[3]. Equation 2.31 shows that the reduced VDF of a bi-Maxwellian is simply a one-dimensional Maxwellian with a thermal speed $w_{zj}^{(b)}$.

[3]The definition of $w_{zj}^{(b)}$ (i.e., the effective thermal speed for a bi-Maxwellian VDF) given in Equation 2.32 is consistent with that of w_{zj} (i.e., the effective thermal speed for an arbitrary VDF) given in Equation 2.19.

Substituting Equation 2.31 into Equation 2.23 gives

$$\Delta I_j^{(b)} = -\frac{q_j\, n_j\, A(\hat{v}_{zj})}{\sqrt{8\,\pi}\, w_{zj}} \int_{-u_j^{(c)}(V_0+\Delta V/2)-v_{zj}}^{-u_j^{(c)}(V_0-\Delta V/2)-v_{zj}} du'_z \\ (u'_z + v_{zj}) \exp\left[-\frac{1}{2}\left(\frac{u'_z}{w_{zj}^{(b)}}\right)^2\right] \ . \tag{2.33}$$

Evaluating this integral gives the final expression for the demodulated current from ion species j:

$$\Delta I_j^{(b)} = \frac{1}{4}\, q_j\, n_j\, A(\hat{v}_{zj}) \left[w_{zj}^{(b)} \sqrt{\frac{2}{\pi}}\, \exp\left[-\frac{1}{2}\left(\frac{u'_z}{w_{zj}^{(b)}}\right)^2\right] \right. \\ \left. - v_{zj}\, \mathrm{erf}\left(\frac{u'_z}{\sqrt{2}\, w_{zj}^{(b)}}\right) \right]_{u'_z=-u_j^{(c)}(V_0+\Delta V/2)-v_{zj}}^{u'_z=-u_j^{(c)}(V_0-\Delta V/2)-v_{zj}} , \tag{2.34}$$

where "erf" denotes the error function (Bevington & Robinson, 2003).

2.4 *Wind*/FC Ion Spectra

The analysis in Section 2.3 considers only a single particle species. However, in reality, a Faraday cup measures the total demodulated current, ΔI, which incorporates the contributions of the various ion species in the plasma. More explicitly,

$$\Delta I = \sum_{\forall j} \Delta I_j + \Delta I^{(n)} \ , \tag{2.35}$$

where the sum is taken over all ion species and $\Delta I^{(n)}$ quantifies the various sources of noise in the measurement.

An *ion spectrum* from the *Wind* Faraday cups consists of all measurements of ΔI, from both cups over a specified number of 3-second spacecraft rotations, Ξ, which may be as high as 31. For any given rotation, the voltage on each cup's modulator is varied (according to a

200 Hz square wave) between

$$V_\xi^{(w)} - \frac{\Delta V_\xi^{(w)}}{2} \ , \qquad \text{and} \qquad V_\xi^{(w)} + \frac{\Delta V_\xi^{(w)}}{2} \ , \tag{2.36}$$

where $\xi = 1, \ldots, \Xi$ indicates the rotation number (Ogilvie et al., 1995). Thus, each spacecraft rotation ξ corresponds to a *voltage window* that is centered at $V_\xi^{(w)}$ and has a width $\Delta V_\xi^{(w)}$. Typically, to within digital precision,

$$\frac{\Delta V_\xi^{(w)}}{V_\xi^{(w)}} = \frac{\Delta V_{\xi+1}^{(w)}}{V_{\xi+1}^{(w)}} \approx 6.5\% \ , \tag{2.37}$$

and

$$V_\xi^{(w)} + \frac{\Delta V_\xi^{(w)}}{2} = V_{\xi+1}^{(w)} - \frac{\Delta V_{\xi+1}^{(w)}}{2} \ , \tag{2.38}$$

for $\xi = 1, \ldots, (\Xi - 1)$ (Ogilvie et al., 1995). These relations provide for the continuous coverage by and the logarithmic spacing of the voltage windows.

Over the course of each spacecraft rotation, each Faraday cup measures ΔI along 20 different directions. Since the two cups point in opposite directions, this corresponds to a total of 40 unique pointing directions:

$$\hat{\mathbf{z}}_1, \ldots, \hat{\mathbf{z}}_\eta, \ldots, \hat{\mathbf{z}}_{40} \ . \tag{2.39}$$

Thus, a *Wind* ion spectrum consists of the set of measurements of the demodulated current

$$\Delta J_{(\eta,\xi)} = \Delta I\left(\hat{\mathbf{z}}_\eta, V_\xi^{(w)}, \Delta V_\xi^{(w)}\right) \ , \tag{2.40}$$

for $\xi = 1, \ldots, \Xi$ and $\eta = 1, \ldots, 40$. The symbol J is used in place of I on the right-hand side of the above expression to emphasize that $\Delta J_{(\eta,\xi)}$ is a measured quantity while ΔI is calculated based on a model. Chapter 3 discusses how the measurements of current can be used to infer properties of the underlying VDF's.

Chapter 3

Processing *Wind*/FC Ion Spectra

This chapter focuses on the theory and practice of analyzing *Wind*/FC ion spectra, which are introduced in Section 2.4. The theoretical basis for interpreting these spectra is presented in Section 3.1, and two different methods for carrying out this analysis are described in Section 3.2. Section 3.3 describes the specific analysis code used in this thesis project and focuses on its improvements over the prior version.

3.1 Physical Meaning of *Wind*/FC Ion Spectra

The measured currents, $\Delta J_{(\eta,\xi)}$, of a *Wind*/FC ion spectrum (see Section 2.4) do not have a direct physical interpretation, per se, because they depend on both the plasma parameters (e.g., particle density) as well as the instrument parameters (e.g., the effective collecting area, A). However, as Equations 2.13 and 2.40 would suggest, each measured $\Delta J_{(\eta,\xi)}$-value reveals some information about the VDF's of the plasma's particle species.

This section describes a simple formalism that relates the $\Delta J_{(\eta,\xi)}$-values of a given spectrum to the proton reduced-VDF, $F_{z_\eta p}$, for that spectrum's various pointing directions, $\hat{\mathbf{z}}_\eta$. This analysis, which essentially is based on Equation 2.15, requires numerous simplifications and, most notably, assumes that the protons are the only ion species in the plasma. Nevertheless, it provides a physically intuitive method of visualizing *Wind*/FC ion spectra and lays the foundation for the moments analysis thereof (see Section 3.2.1).

3.1.1 Relating Current to the Reduced VDF

The center voltage and voltage width of a spectrum's ξ-th window are respectively denoted V_ξ and ΔV_ξ. If protons are assumed to be the only ion species in the plasma, then the voltage windows can be converted to inflow-speed windows. So long as the window's relative width is sufficiently narrow, its center inflow-speed is approximately

$$u_\xi^{(w)} = u_p^{(c)}\left(V_\xi^{(w)}\right) \ , \tag{3.1}$$

and its width in inflow speed is

$$\Delta u_\xi^{(w)} = u_p^{(c)}\left(V_\xi^{(w)} + \frac{\Delta V_\xi^{(w)}}{2}\right) - u_p^{(c)}\left(V_\xi^{(w)} - \frac{\Delta V_\xi^{(w)}}{2}\right) \ . \tag{3.2}$$

The function $u_p^{(c)}(V)$ (see Equation 2.8) can likewise be approximated by its first-order Taylor expansion about $V = V_\xi^{(w)}$:

$$u_p^{(c)}(V) = u_p^{(c)}\left(V_\xi^{(w)}\right) + \frac{u_p^{(c)}\left(V_\xi^{(w)}\right)}{2\,V_\xi^{(w)}}\,\left(V - V_\xi^{(w)}\right) \ . \tag{3.3}$$

Thus,

$$\Delta u_\xi^{(w)} = \frac{1}{2}\,u_p^{(c)}\left(V_\xi^{(w)}\right)\,\frac{\Delta V_\xi^{(w)}}{V_\xi^{(w)}} = \frac{1}{2}\,u_\xi^{(w)}\,\frac{\Delta V_\xi^{(w)}}{V_\xi^{(w)}} \ . \tag{3.4}$$

Assuming that the proton VDF is sufficiently supersonic, Equation 2.15 can be used to deduce that the measured current for the ξ-th window along the η-th pointing direction, $\hat{\mathbf{z}}_\eta$, is

$$\Delta J_{(\eta,\xi)} = -\frac{q_p}{2}\, A(\hat{v}_{z_\eta p}) \int_{-\left(u_\xi^{(w)}+\Delta u_\xi^{(w)}/2\right)}^{-\left(u_\xi^{(w)}-\Delta u_\xi^{(w)}/2\right)} du_{z_\eta}\, u_{z_\eta}\, F_{z_\eta p}\big(u_{z_\eta}\big) \ . \tag{3.5}$$

For a sufficiently narrow window (relative to the width of the VDF), the measured current can be approximated as

$$\Delta J_{(\eta,\xi)} = \frac{q_p}{2}\, A(\hat{v}_{z_\eta p})\, F_{z_\eta p}\Big(u_\xi^{(w)}\Big)\ u_\xi^{(w)}\, \Delta u_\xi^{(w)} \ . \tag{3.6}$$

With the integral now gone, this expression can be rearranged to give

$$\tilde{F}_{z_\eta p}\Big(u_\xi^{(w)}\Big) = \frac{2\,\Delta J_{(\eta,\xi)}}{q_p\, A(\hat{v}_{z_\eta p})\, u_\xi^{(w)}\, \Delta u_\xi^{(w)}} \ . \tag{3.7}$$

The left-hand side of this equation appears as $\tilde{F}_{z_\eta p}$ rather than $F_{z_\eta p}$ in order to emphasize that the right-hand side is the value of $F_{z_\eta p}$ that is inferred from the measured current, $\Delta J_{(\eta,\xi)}$. Conveniently, $\tilde{F}_{z_\eta p}$ is directly proportional to $\Delta J_{(\eta,\xi)}$, and, other than physical constants, the constant of proportionality depends only on the design and settings of the instrument.

3.1.2 Visualizing *Wind*/FC Ion Spectra

Though Equation 3.7 was derived using numerous assumptions, it provides a mechanism for visualizing a *Wind*/FC ion spectrum that emphasizes the physical meaning of the raw measurements. Rather than the measured current, $\Delta J_{(\eta,\xi)}$, being plotted versus V_ξ, the inferred reduced-VDF, $\tilde{F}_{z_\eta p}$, are plotted versus $u_\xi^{(w)}$. Essentially, this process removes the instrument parameters (e.g., effective collecting area) from the plot to leave only the plasma parameters.

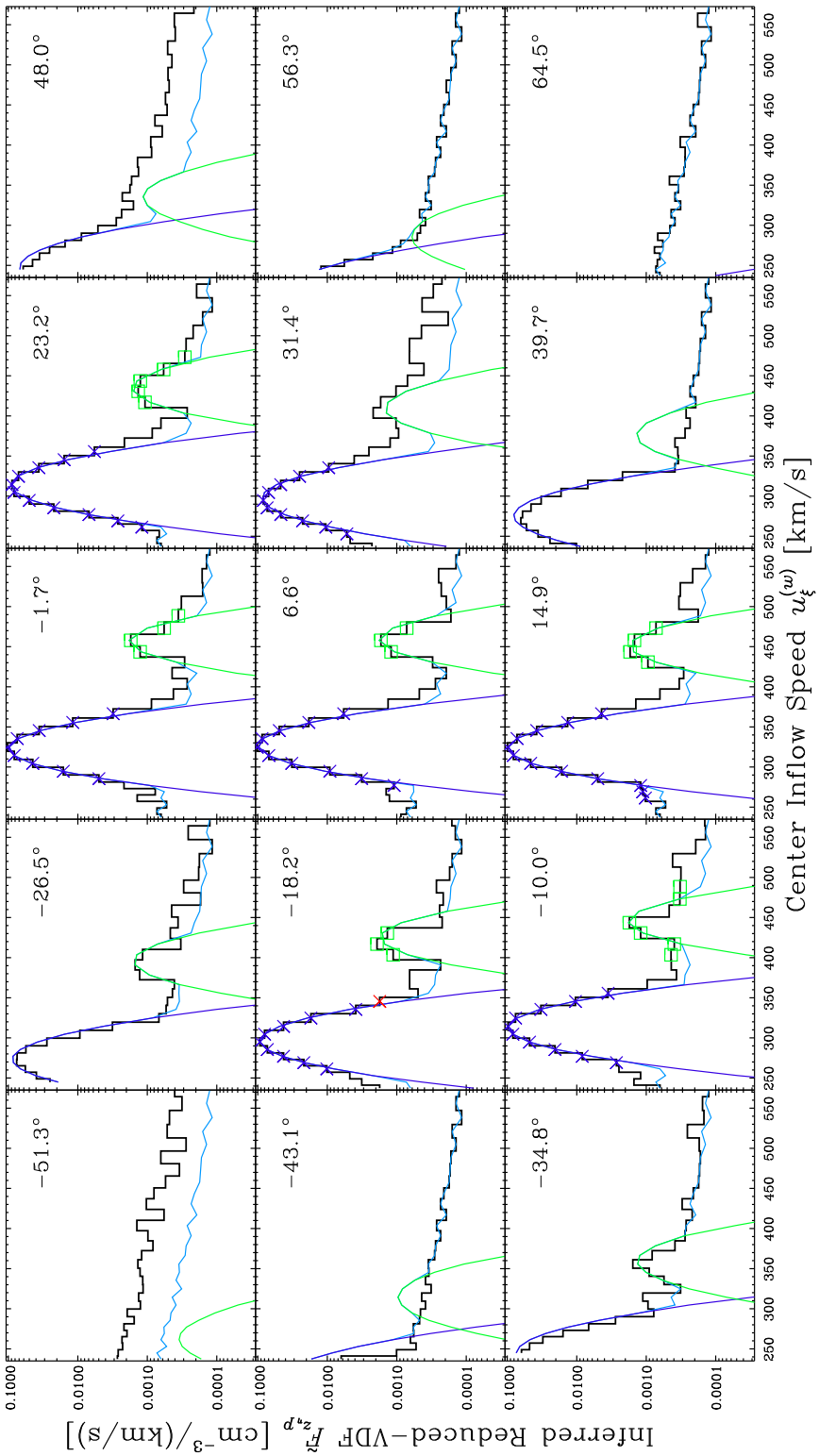

Figure 3.1.— A partial *Wind*/FC ion spectrum from 00:20 UTC on 03 January 2008. Each plot shows, in black, the inferred reduced-VDF, $\tilde{F}_{z_\eta p}$, versus $u^{(w)}_\xi$ (as defined in Equations 3.7 and 3.1, respectively) for a different pointing direction, $\hat{\mathbf{z}}_\eta$. The colored symbols and curves indicate the results of the `dvapbimax` analysis code (see Section 3.3.2).

For example, Figure 3.1 shows part of a typical *Wind*/FC ion spectrum that was collected at roughly 00:20 UTC on 3 January 2008. More specifically, this figure contains a plot (in black) of $\tilde{F}_{z_\eta p}$ versus $u_\xi^{(w)}$ for each of 15 pointing directions $\hat{\mathbf{z}}_\eta$. A full *Wind* ion spectrum contains measurements from 40 pointing directions (see Section 2.4), but the remaining 25 have been excluded for concision.

Each plot in Figure 3.1 is labeled with the azimuthal angle between its corresponding $\hat{\mathbf{z}}_\eta$ and the sunward direction. A "noise floor" is visible in each plot and is actually the result of the instrument's non-zero measurement threshold[1]. The plots for which the cup was pointed in the Sun's general direction also show two peaks: the taller, lower-speed peak corresponds to the protons and the other to the α-particles. Even though the α-particle bulk speed is usually comparable to that of the protons, the α-particle peak in each plot appears translated by a factor of about 2 relative to the proton peak because, by Equation 2.8,

$$u_j^{(c)}(V) = \sqrt{\frac{q_j \,/\, q_p}{m_j \,/\, m_p}}\, u_p^{(c)}(V) \ , \tag{3.8}$$

for any ion species j and modulator voltage V. This scaling allows Faraday cups to be used to discriminate among different particle populations based on charge-to-mass ratio.

The plots in Figure 3.1 also contain various colored curves and symbols. These indicate the results of the `dvapbimax` analysis code, which is described in Section 3.3.2.

[1]More formally, this is the smallest current that the spacecraft is able to digitally encode. While this threshold is independent of the modulator voltage, V, this noise floor appears as a power law because the voltage bins of a *Wind*/FC ion spectrum are logarithmically spaced (see Equation 2.37). However, the noise floor does have slight deviations from an ideal power law because the finite set of discrete voltages that the instrument's high voltage power supply can produce do not themselves have perfectly logarithmic spacing.

3.2 Methods for Analyzing *Wind*/FC Ion Spectra

This section introduces the principles behind two algorithms for processing ion spectra from the *Wind* Faraday cups: moments analysis and non-linear analysis. While the discussion in this section is primarily theoretical, specific implementations of these analysis techniques are detailed in Section 3.3.

3.2.1 Moments Analysis

In its simplest form, moments analysis assumes that protons are the only ion species in the plasma[2]. In this technique, data from each pointing direction $\hat{\mathbf{z}}_\eta$ are considered separately, and discrete calculus is used to infer values for n_p, $v_{z_\eta p}$, and $w_{z_\eta p}$ from the moments of the inferred reduced-VDF, $\tilde{F}_{z_\eta p}$. This approach is limited because it ignores the effects of other ion species (most notably, α-particles) as well as the noise floor. Additionally, moments analysis relies heavily on Equation 3.7, which was derived based on numerous assumptions about the operation of the instrument and the plasma parameters. Nevertheless, moments analysis has the advantage of being computationally relatively simple and robust.

For a given pointing direction, $\hat{\mathbf{z}}_\eta$, summing Equation 3.7 over all velocity windows gives

$$\sum_{\xi=1}^{\Xi} \tilde{F}_{z_\eta p}\left(u_\xi^{(w)}\right) \Delta u_\xi^{(w)} = \frac{2}{q_p\, A(\hat{v}_{z_\eta p})} \sum_{\xi=1}^{\Xi} \frac{\Delta J_{(\eta,\xi)}}{u_\xi^{(w)}} \ . \tag{3.9}$$

Assuming that the velocity windows are relatively narrow and offer sufficiently wide and

[2]While the moments analysis code for *Wind* Faraday cup spectra makes this assumption, it is not absolutely necessary. For example, the corresponding code for the SWEPAM ion instrument on the *ACE* spacecraft is able to discriminate among different ion species. However, the *ACE*/SWEPAM instrument suite (McComas et al., 1998) differs substantially from *Wind*/SWE (Ogilvie et al., 1995).

continuous coverage, the left-hand side of the above expression is approximately the zeroth moment of $F_{z_\eta p}$. By this assumption and Equation 2.17,

$$\sum_{\xi=1}^{\Xi} \tilde{F}_{z_\eta p}\Big(u_\xi^{(w)}\Big)\,\Delta u_\xi^{(w)} \approx \int_{-\infty}^{\infty} F_{z_\eta p}\Big(u_\xi^{(w)}\Big)\,du_\xi^{(w)} = n_p\ . \tag{3.10}$$

Therefore, the inferred proton density is

$$\tilde{n}_{\eta p} = \frac{2}{q_p\,A\Big(\hat{\tilde{v}}_{z_\eta p}\Big)} \sum_{\xi=1}^{\Xi} \frac{\Delta J_{(\eta,\xi)}}{u_\xi^{(w)}}\ . \tag{3.11}$$

The subscript η on $\tilde{n}_{\eta p}$ indicates that a separate value for n_p is inferred along each pointing direction $\hat{\mathbf{z}}_\eta$. A better estimate of n_p can be derived from the weighted average of multiple $\tilde{n}_{\eta p}$-values, where the weights are computed based on the standard methods of error propagation (Bevington & Robinson, 2003).

The first moment of the reduced VDF can be approximated in the same way so that, by Equation 2.18,

$$\sum_{\xi=1}^{\Xi} u_\xi^{(w)}\,\tilde{F}_{z_\eta p}\Big(u_\xi^{(w)}\Big)\,\Delta u_\xi^{(w)} \approx \int_{-\infty}^{\infty} u_\xi^{(w)}\,F_{z_\eta p}\Big(u_\xi^{(w)}\Big)\,du_\xi^{(w)} = n_p\,v_{z_\eta p}\ . \tag{3.12}$$

Combining this result with Equation 3.7 gives the inferred value for the proton bulk speed along the z_η-axis:

$$\tilde{v}_{z_\eta p} = \frac{2}{q_p\,\tilde{n}_{\eta p}\,A\Big(\hat{\tilde{v}}_{z_\eta p}\Big)} \sum_{\xi=1}^{\Xi} \Delta J_{(\eta,\xi)}\ . \tag{3.13}$$

Finally, this method, along with Equation 2.19, can be used to approximate the second moment of the reduced VDF:

$$\begin{aligned} \sum_{\xi=1}^{\Xi} \Big(u_\xi^{(w)}\Big)^2\,\tilde{F}_{z_\eta p}\Big(u_\xi^{(w)}\Big)\,\Delta u_\xi^{(w)} &\approx \int_{-\infty}^{\infty} \Big(u_\xi^{(w)}\Big)^2\,F_{z_\eta p}\Big(u_\xi^{(w)}\Big)\,du_\xi^{(w)} \\ &= n_p\left(w_{z_\eta p}^2 + v_{z_\eta p}^2\right)\ . \end{aligned} \tag{3.14}$$

This result, along with Equation 3.7, gives the inferred value for the proton thermal speed along the z_η-axis:

$$\tilde{w}_{z_\eta p} = \sqrt{\frac{2}{q_p\,\tilde{n}_{\eta p}\,A\Big(\hat{\tilde{v}}_{z_\eta p}\Big)}\sum_{\xi=1}^{\Xi} u_\xi^{(w)}\,\Delta J_{(\eta,\xi)} - \tilde{v}_{z_\eta p}^2}\ . \tag{3.15}$$

Equations 3.11, 3.13, and 3.15 specify the values of n_p, $v_{z_\eta p}$, and $w_{z_\eta p}$ inferred from a moments analysis of the η-th speed window of a *Wind*/FC ion spectrum. However, $v_{z_\eta p}$, and $w_{z_\eta p}$ are not particularly useful quantities, per se, because they are specific to the z_η-axis. Additionally, the quantity

$$A\Big(\hat{\tilde{v}}_{z_\eta p}\Big)\ , \tag{3.16}$$

appears as a factor in all three equations. While the effective collecting area function, A, itself is measured as part of instrument calibration or estimated based on the instrument's design, its argument in these equations can only be computed if the vector bulk velocity, $\mathbf{v}_p$, can be inferred.

For these reasons, data from multiple pointing directions are necessary. Presumably, each pointing direction, $\hat{\mathbf{z}}_\eta$, of the cup is known *a priori* and therefore can be expressed in geocentric solar ecliptic (GSE) coordinates (Russell, 1971) (or any other standard coordinate system that is independent of the spacecraft). More formally, this means that each $\hat{\mathbf{z}}_\eta$ can be expressed as

$$\hat{\mathbf{z}}_\eta = (\hat{\mathbf{z}}_\eta \cdot \hat{\mathbf{x}}_{\mathrm{GSE}})\,\hat{\mathbf{x}}_{\mathrm{GSE}} + (\hat{\mathbf{z}}_\eta \cdot \hat{\mathbf{y}}_{\mathrm{GSE}})\,\hat{\mathbf{y}}_{\mathrm{GSE}} + (\hat{\mathbf{z}}_\eta \cdot \hat{\mathbf{z}}_{\mathrm{GSE}})\,\hat{\mathbf{z}}_{\mathrm{GSE}}\ , \tag{3.17}$$

where each of the above dot products is known (based on the instrument configuration) for each $\hat{\mathbf{z}}_\eta$. The z_η-component of the proton bulk velocity can likewise be expressed in terms of

the these known dot products:

$$\begin{aligned} v_{z_\eta p} &= \mathbf{v}_p \cdot \hat{\mathbf{z}}_\eta \\ &= v_{x_{\mathrm{GSE}}\,p}\left(\hat{\mathbf{z}}_\eta \cdot \hat{\mathbf{x}}_{\mathrm{GSE}}\right) + v_{y_{\mathrm{GSE}}\,p}\left(\hat{\mathbf{z}}_\eta \cdot \hat{\mathbf{y}}_{\mathrm{GSE}}\right) + v_{z_{\mathrm{GSE}}\,p}\left(\hat{\mathbf{z}}_\eta \cdot \hat{\mathbf{z}}_{\mathrm{GSE}}\right) \ . \end{aligned} \tag{3.18}$$

Thus, for a given *Wind*/FC ion spectrum, values of $\tilde{v}_{z_\eta p}$ from multiple pointing directions, $\hat{\mathbf{z}}_\eta$, can be used together to derive estimators for the components of $\mathbf{v}_p$ in the GSE (or any other) coordinate system.

If a bi-Maxwellian model is assumed for the proton VDF, a similar procedure can be used to extract estimates of $w_{\perp p}$ and $w_{\parallel p}$ from the inferred values of $w_{z_\eta p}$ based on Equation 2.32. However, this method requires measurements of the direction of the background magnetic field, $\hat{\mathbf{B}}_0$, in order to separate the perpendicular and parallel thermal speeds. In the case of *Wind*, measurements of $\hat{\mathbf{B}}_0$ are readily available from another of its instruments (see Section 3.3.1).

3.2.2 Non-Linear Analysis

As discussed above, the moments analysis of a *Wind*/FC spectrum has numerous limitations. First, the derivation of Equations 3.11, 3.13, and 3.15 relies on numerous assumptions, most of which related to the relative width of each inflow-speed window being sufficiently small. In reality, though, the windows are rather coarsely spaced so that a higher cadence of spectra can be achieved. Second, the moments analysis derived above does not account for the finite performance characteristics of the instrument. The *Wind* Faraday cups operate near their detection threshold, which can consequently skew the results of a moments analysis. Third, this moments analysis provides no mechanism for inferring the physical properties of the α-particles.

Non-linear fitting offers an alternative that eliminates some of these problems. In this approach, an analytic expression that is dependent on known instrument parameters and unknown particle parameters is developed to model the measured currents, $\Delta J_{(\eta,\xi)}$, of a spectrum. Then, the best-fit values of the particle parameters can be derived from a non-linear fitting algorithm (i.e., χ^2-minimization program) (Taylor, 1997; Bevington & Robinson, 2003).

For example, in the standard code, the *Wind* Faraday cups are assumed to only detect protons and α-particles and that each of these species has a bi-Maxwellian VDF. Consequently, the measured currents are modeled as follows:

$$\begin{aligned}\Delta J_{(\eta,\xi)} = \Delta I_p^{(b)}\left(\hat{\mathbf{z}}_\eta, V_\xi^{(w)}, \Delta V_\xi^{(w)}\right) + \Delta I_\alpha^{(b)}\left(\hat{\mathbf{z}}_\eta, V_\xi^{(w)}, \Delta V_\xi^{(w)}\right) \\ + \Delta I^{(n)}\left(\hat{\mathbf{z}}_\eta, V_\xi^{(w)}, \Delta V_\xi^{(w)}\right) \ ,\end{aligned} \tag{3.19}$$

where the $\Delta I_j^{(b)}$ terms are as specified in Equation 2.34 and $\Delta I^{(n)}$ is a function that models all sources of "noise" (e.g., the non-zero detection threshold of the instrument).

Of course, as is detailed below, non-linear analysis is fraught with its own complications. First, initial guesses of the fit parameters are required by virtually all non-linear fitting algorithms. Especially for complicated models, these algorithms tend to be highly-sensitive to the initial guesses and to converge properly only for guesses that are already quite close to the best-fit values. Second, non-linear fitting programs usually invoke iterative or Monte-Carlo algorithms, which typically require very large numbers of CPU cycles.

3.3 Code for Analyzing *Wind*/FC Ion Spectra

Since *Wind*'s inception, the analysis software for ion spectra from its Faraday cups has been written and rewritten several times. The earliest and most fundamental programs were developed at the Massachusetts Institute of Technology (MIT) primarily by Drs. Alan Lazarus and John Steinberg and focused primarily on deriving the proton bulk parameters. Modifications by Dr. Mathias Aellig expanded the code to derive both proton and α-particle parameters. Later, Dr. Justin Kasper built upon Dr. Aellig's work to develop the `IDL` program `apbimax`, which (for the first time) modeled the ion VDF's as bi-Maxwellians (versus Maxwellians) (Kasper, 2002).

A major component of this thesis project was the modification of `apbimax` to a yet more sophisticated version: `dvapbimax`. All *Wind*/FC ion parameters presented in the subsequent chapters of this dissertation are from the output of `dvapbimax`. This section provides a detailed description of `dvapbimax`, but first presents an outline of `apbimax`, upon which it was based.

3.3.1 The `apbimax` Code

To process a given *Wind*/FC ion spectrum, the `apbimax` code first loads in the data from that spectrum: i.e., the measured values of $\Delta J_{(\eta,\xi)}$ along with the associated values of $\hat{\mathbf{z}}_\eta$, $V_\xi^{(w)}$, and $\Delta V_\xi^{(w)}$. However, in order to separate the perpendicular and parallel temperature components, `apbimax` also needs measurements of the background magnetic field, $\mathbf{B}_0$, which are taken from *Wind*'s Magnetic Field Investigation (MFI) (Lepping et al., 1995). The publicly-available *Wind*/MFI data provide measurements of the local magnetic field at a

3-second cadence (i.e., essentially one measurement per rotation[3]). Since a *Wind*/FC ion spectrum is measured over $\Xi > 1$ rotations, $\mathbf{B}_0$ is simply taken to be the average measured value:

$$\overline{\mathbf{B}} = \frac{1}{\Xi} \sum_{\xi=1}^{\Xi} \mathbf{B}_{\xi} \ , \tag{3.20}$$

where $\mathbf{B}_{\xi}$ denotes the local magnetic field as measured during the spectrum's ξ-th spacecraft rotation.

As stated above, `apbimax` models the plasma as being composed of protons and α-particles and assumes that each species has a bi-Maxwellian VDF (see Equation 3.19). This gives a total of twelve free parameters: each species j has the three components of its bulk velocity ($\mathbf{v}_j$), its number density (n_j), and its perpendicular and parallel thermal speeds ($w_{\perp j}$ and $w_{\parallel j}$, respectively). The ultimate function of `apbimax` is to use a non-linear algorithm to fit the model specified in Equation 3.19 to the spectrum's measured currents, $\Delta J_{(\eta,\xi)}$, and thereby derive best-fit values for these twelve free parameters. However, because the parameter space is relatively large, `apbimax` employs a multi-step process to reduce false or failed convergences of the fitting algorithm.

First, `apbimax` uses a moments analysis (as described above) to derive estimates of the protons' six free parameters, which are then used as initial guesses for these parameters in the non-linear analysis. Initial guesses of the α-particle parameters are naïvely derived from those for the proton parameters. For example, the initial guess of n_{α} is taken to be 0.03 times the initial guess of n_p.

Next, `apbimax` selects which of the spectrum's $\Delta J_{(\eta,\xi)}$-values will be used for the non-

[3]The measurements of the magnetic field by *Wind*/MFI are provided, to within the precision of spacecraft's clock, at a 3-second cadence. However, *Wind*'s rotation period is not exactly 3 seconds and has actually varied slightly over the course of its mission.

linear fit. This step is necessary because, as exemplified by the spectrum in Figure 3.1, most $\Delta J_{(\eta,\xi)}$-values have ion contributions that fall below the noise floor (i.e., the detection threshold) of the instrument (see Equation 3.19). When such data are included in the non-linear fitting, they often cause the algorithm to converge to non-physical parameter values. Based on the initial guesses of the fit parameters, the code identifies two subsets of the spectrum's $\Delta J_{(\eta,\xi)}$-values (that need not be mutually exclusive): those for which protons seem to have contributed significantly to the measured current (i.e., the "proton points") and likewise for the α-particles (i.e., the "α-particle points").

Once the point selection is made, `apbimax` finally runs the non-linear fitting, which is actually done twice. First, `apbimax` uses only the proton points and calculates best-fit values for the six proton parameters. These new proton parameters are then used to generate new initial guesses of the α-particle parameters (in lieu of those from the moments analysis) and point selection is rerun. Finally, `apbimax` runs the non-linear fitting algorithm for the second time, but now fits all twelve free parameters based on all selected points (i.e., the unions of the proton and the α-particle points).

3.3.2 The `dvapbimax` Code

The plots of *Wind*/FC ion spectra in this chapter are shown with the results of the `dvapbimax` analysis. The blue and green curves correspond to $F^{(b)}_{z_\eta j}$ (for $j = p$ and α, respectively; see Equation 2.31) as evaluated using the best-fit parameter values from `dvapbimax`. The cyan curve indicates the sum of the blue and green curves along with a noise term that reflects the non-zero detection threshold of the instrument (see Equation 3.19). Like its predecessor, `dvapbimax` uses an algorithm for point selection: blue $\times$'s indicate proton points, green

□'s indicate α-particle points, and cyan ⊠'s indicate points for both species. Occasionally, selected points are shown in red rather than their usual color; these data were used in the fit but then subsequently identified as likely outliers.

As stated above, `dvapbimax` is an enhanced version of `apbimax` that was developed as a major component of this thesis project. The name "`dvapbimax`" refers to one of the key features of this code: an improved model of the α-proton differential flow

$$\Delta \mathbf{v}_{\alpha p} = \mathbf{v}_{\alpha} - \mathbf{v}_{p} \ , \tag{3.21}$$

which is detailed below along with other modifications.

3.3.2.1 Improved Model of α-Proton Differential Flow

In `apbimax`, the components of proton and α-particle bulk velocities along each axis are mutually-independent fit parameters. However, the gyrotropy of the solar wind, which helps to give rise to the bi-Maxwellian distribution in the first place (see Chapter 1), would suggest that $\Delta \mathbf{v}_{\alpha p}$ should tend to be parallel to the background magnetic field, $\mathbf{B}_0$. Indeed, the distribution in Figure 3.2, which was generated by Kasper et al. (2006) using output from `apbimax`, confirms that (to within instrumental precision) $\Delta \mathbf{v}_{\alpha p}$ is almost always parallel to the average magnetic field, $\overline{\mathbf{B}}$. The only significant exception occurs when $\Delta v_{\alpha p}$ is very small. However, this is to be expected since, for small values of $\Delta v_{\alpha p}$, the relative uncertainty in $\Delta v_{\alpha p}$ is so large that (to within instrumental precession) $\Delta v_{\alpha p}$ is effectively zero.

Based on this assessment, `apbimax`'s use of independent proton and α-particle bulk velocities is redundant. For `dvapbimax`, the perpendicular component of the α-proton differential flow, $\Delta v_{\perp \alpha p}$, was explicitly assumed to be zero so that the fit parameters $v_{x\alpha}$, $v_{y\alpha}$, and $v_{z\alpha}$ could be replaced with a single free parameter for the parallel component of differential

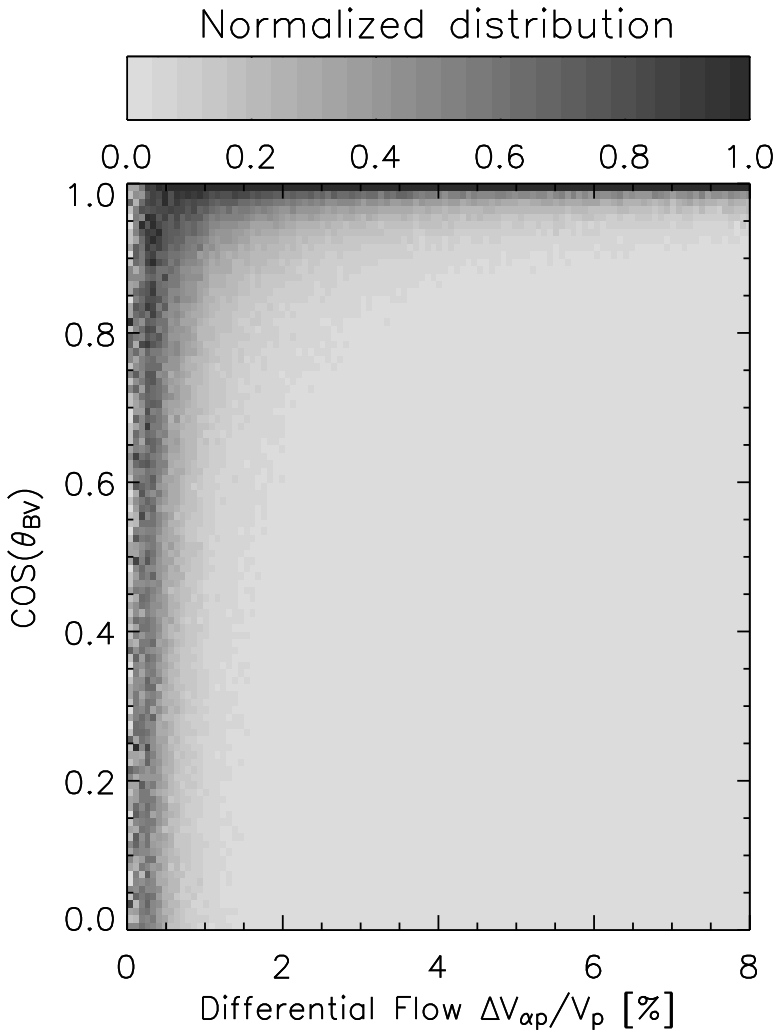

Figure 3.2.— Distribution, reproduced from Kasper et al. (2006), of the values of $\Delta v_{\alpha p} \,/\, v_p$ and $\left|\Delta \hat{\mathbf{v}}_{\alpha p} \cdot \hat{\overline{\mathbf{B}}}\right|$ from `apbimax` output. Each column has been normalized so that the maximum value therein is unity. When $\Delta v_{\alpha p} \,/\, v_p$ is very small, the differential flow's magnitude is (to within measurement precision) zero, and its angle relative to the measured magnetic field is noise-dominated. However, for all other values of $\Delta v_{\alpha p} \,/\, v_p$, the value of $\left|\Delta \hat{\mathbf{v}}_{\alpha p} \cdot \hat{\overline{\mathbf{B}}}\right|$ generally strays very little from unity, which suggests that the differential flow remains strongly aligned with the background magnetic field under most conditions in the solar wind.

flow: $\Delta v_{\|\alpha p}$. Under this convention, the inferred value of $\mathbf{v}_\alpha$ is calculated (via Equation 3.21) from the fit value of $\mathbf{v}_p$ and

$$\Delta \mathbf{v}_{\alpha p} = \Delta v_{\|\alpha p} \hat{\mathbf{B}}_0 \ , \tag{3.22}$$

where the value of $\Delta v_{\|\alpha p}$ is taken from the fit and the value of $\hat{\mathbf{B}}_0$ is derived from *Wind*/MFI data. The introduction of this new model for differential flow reduced the total number of fit parameters from twelve to ten. In general, the removal of superfluous parameters decreases both the computation time and the likelihood of the algorithm failing to converge or converging to a false fit.

3.3.2.2 Higher-Cadence Measurements of Magnetic Field

As stated above, `apbimax` uses *Wind*/MFI data with a 3-second time resolution but then averages these measurements of the magnetic field over the duration of each ion spectrum. However, the direction of the solar wind's magnetic field is known to change very rapidly. The variation in the magnetic field direction over the course of a given spectrum can be quantified by the angular deviation

$$\psi_{\mathbf{B}} = \frac{1}{\Xi} \sum_{\xi=1}^{\Xi} \arccos \left(\hat{\mathbf{B}}_\xi \cdot \hat{\overline{\mathbf{B}}} \right) \ . \tag{3.23}$$

Figure 3.3 shows a plot of $\psi_{\mathbf{B}}$ for a one-hour sample of 3-second MFI data; for simplicity, rather than showing $\psi_{\mathbf{B}}$ for individual ion spectra, a running, 31-measurement window is used instead. While $\psi_{\mathbf{B}}$ sometimes remained close to zero, this plot shows periods during which $\psi_{\mathbf{B}}$ became quite large, which correspond to times when the direction of the magnetic field was changing dramatically.

These changes in the direction of the magnetic field have important implications for the measurement of temperature anisotropy. Under typical conditions in the solar wind,

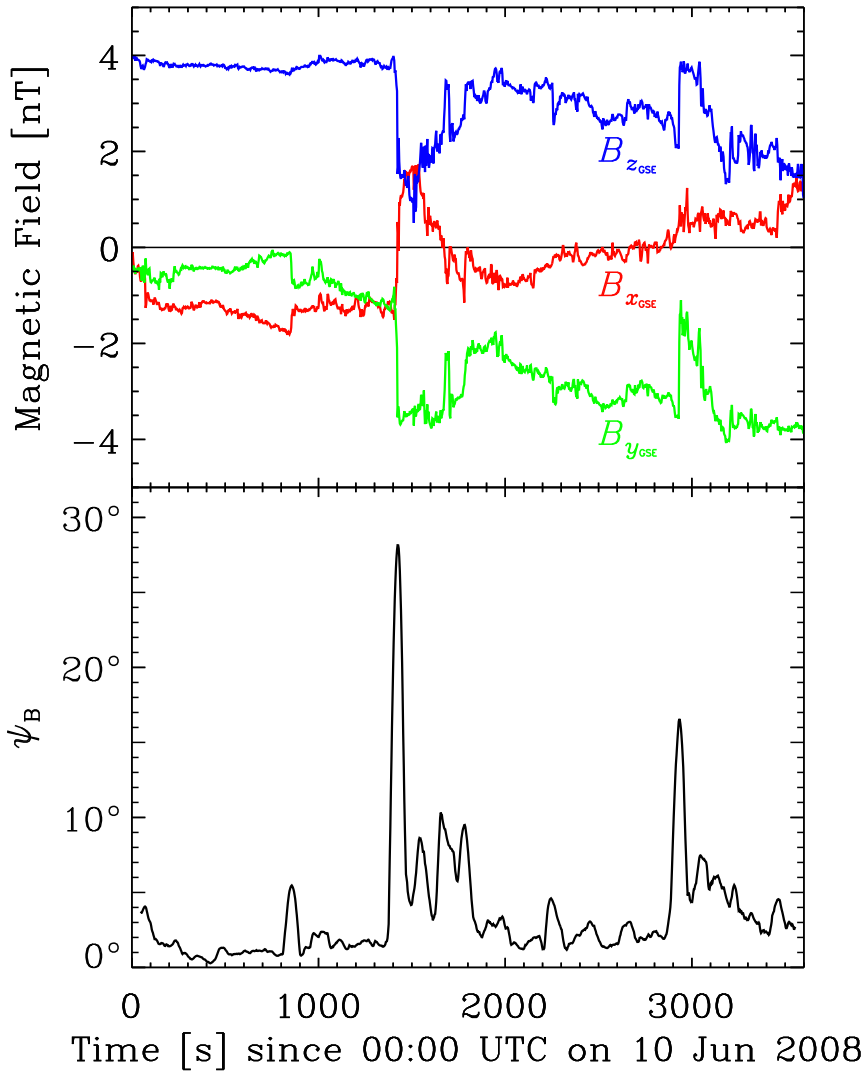

Figure 3.3.— Plots of the magnetic field components (top) and $\psi_{\mathbf{B}}$ (bottom) for a one-hour period of 3-second *Wind*/MFI data beginning at 00:00 UTC on 10 June 2008. The upper plot uses the geocentric solar ecliptic (GSE) coordinate system (Russell, 1971); the x_{GSE}-component of the magnetic field $\mathbf{B}$ is shown in red, the y_{GSE}-component in green, and the z_{GSE}-component in blue. The lower plot was generated using Equation 3.23 with a running 31-measurement window (i.e., $\Xi = 31$).

the magnetic field varies far more rapidly than the ion bulk parameters. Nevertheless, the perpendicular and parallel temperature components are defined relative to the background magnetic field. Therefore, even if the temperature components are nearly constant over a given ion spectrum, the variations in the magnetic field direction cause the ion VDF's to rotate in kind. When the *Wind* Faraday cups measure an ion spectrum while this is happening, the perpendicular and parallel temperature components are smeared together, which causes the temperature to seem more isotropic than it actually is.

In `dvapbimax`, the averaging of MFI data has been eliminated so that each speed window (i.e., 3-second spacecraft rotation) of each spectrum has its own measurement of the background magnetic field. Essentially, `dvapbimax` uses $\hat{\mathbf{B}}_\xi$ for $\hat{\mathbf{B}}_0$ in Equations 2.32 and 3.22, while `apbimax` uses $\hat{\overline{\mathbf{B}}}$. Thus, even though `dvapbimax` assigns each spectrum a single value for each of its ten fit parameters (including $\Delta v_{\parallel \alpha p}$, $w_{\perp j}$, and $w_{\parallel j}$), the values of $\Delta \mathbf{v}_{\alpha p}$ and $w_{z_\eta j}$ vary from rotation to rotation.

The use of the higher-resolution magnetic field data, along with the differential flow model described above, has produced significant improvements in the quality of `dvapbimax` output relative to that of `apbimax`. For example, Figure 3.4 shows a partial ion spectrum from a period of high magnetic-variability along with the corresponding `dvapbimax` analysis. In the `apbimax` analysis, the fitted reduced-VDF of each ion species in each pointing direction would always appear as a parabola on a log-lin plot (like those in this figure) because the VDF is modeled with a bi-Maxwellian and the magnetic field is assumed to be constant. A parabola, though, does not describe the α-particle spectral peaks in Figure 3.4. However, these irregularities are reproduced quite well by the reduced VDF's from the `dvapbimax` analysis. Evidently, the non-parabolic shapes of the α-particle spectral peaks primarily result from strong changes in the direction of the magnetic field, which `dvapbimax` incorporates

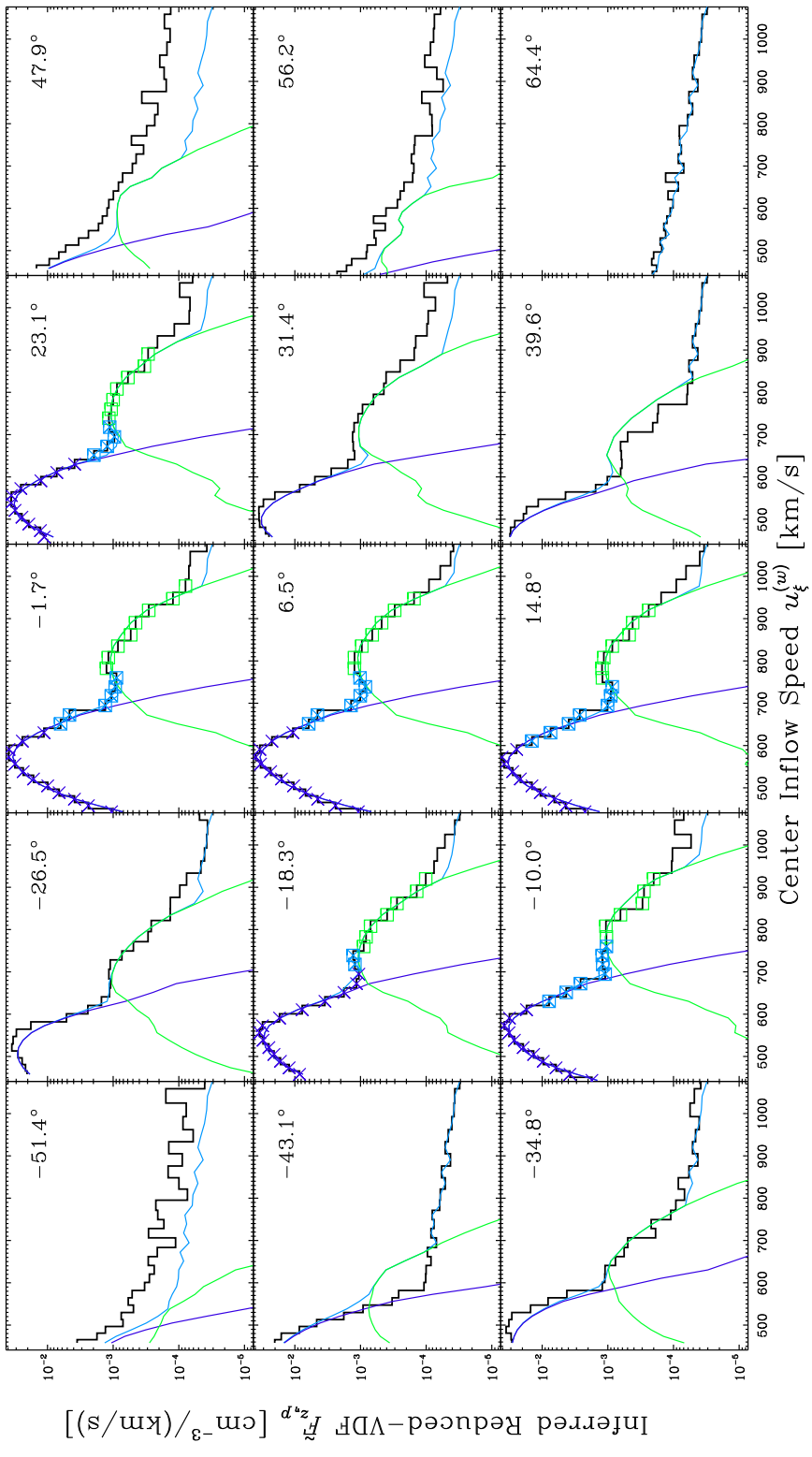

Figure 3.4.— A partial *Wind*/FC ion spectrum from 00:25 UTC on 14 January 2008 that exemplifies `dvapbimax`'s use of higher-resolution magnetic field measurements. Taking advantage of the higher-cadence magnetic field measurements, `dvapbimax` was able to account for the irregular features of the α-particle spectral peaks (green □'s).

more accurately than its predecessor.

For broader evidence of the superiority of `dvapbimax` to `apbimax` in this regard, Figure 3.5 shows a direct, statistical comparison of the output from these two codes. To generate this plot, the $(\psi_{\mathbf{B}}, R_p)$-plane was divided into bins that were linearly spaced along the $\psi_{\mathbf{B}}$-axis and logarithmically spaced along the R_p-axis. The ion spectra were then divided among these bins based first on the results of `apbimax` and then based on the results of `dvapbimax`. For a fair comparison, only spectra that were successfully fit by both programs were used. For each bin, separate counts were kept of the number of `apbimax` spectra and the number of `dvapbimax` spectra therein. The plot in Figure 3.5 shows the ratio of the `dvapbimax` counts to the `apbimax` counts for bins which had at least 16 spectra from each code.

Since `apbimax` and `dvapbimax` calculate $\psi_{\mathbf{B}}$ in the same way, Figure 3.5 compares the R_p-values of `dvapbimax` to those of `apbimax` as a function of $\psi_{\mathbf{B}}$. This plot shows that `dvapbimax` generally produces more extreme values (both $\gg 1$ and $\ll 1$) for R_p, which suggests that `apbimax` truly does suppress temperature anisotropy by smearing temperature components.

3.3.2.3 Improved Non-Linear Fitting Algorithm

For the non-linear fitting of the *Wind*/FC ion spectra, `apbimax` uses the standard `IDL` command `curvefit`, which is an implementation of the Levenberg-Marquardt algorithm (Marquardt, 1963) and is based largely on the implementation given by Bevington & Robinson (2003). However, for the `dvapbimax` code, `curvefit` was replaced with Dr. Craig Markwardt's `mpfit` (Markwardt, 2009). While `mpfit` is also an implementation of the Levenberg-Marquardt algorithm, it is based on that found in the `MINPACK-1` library of `FORTRAN` subrou-

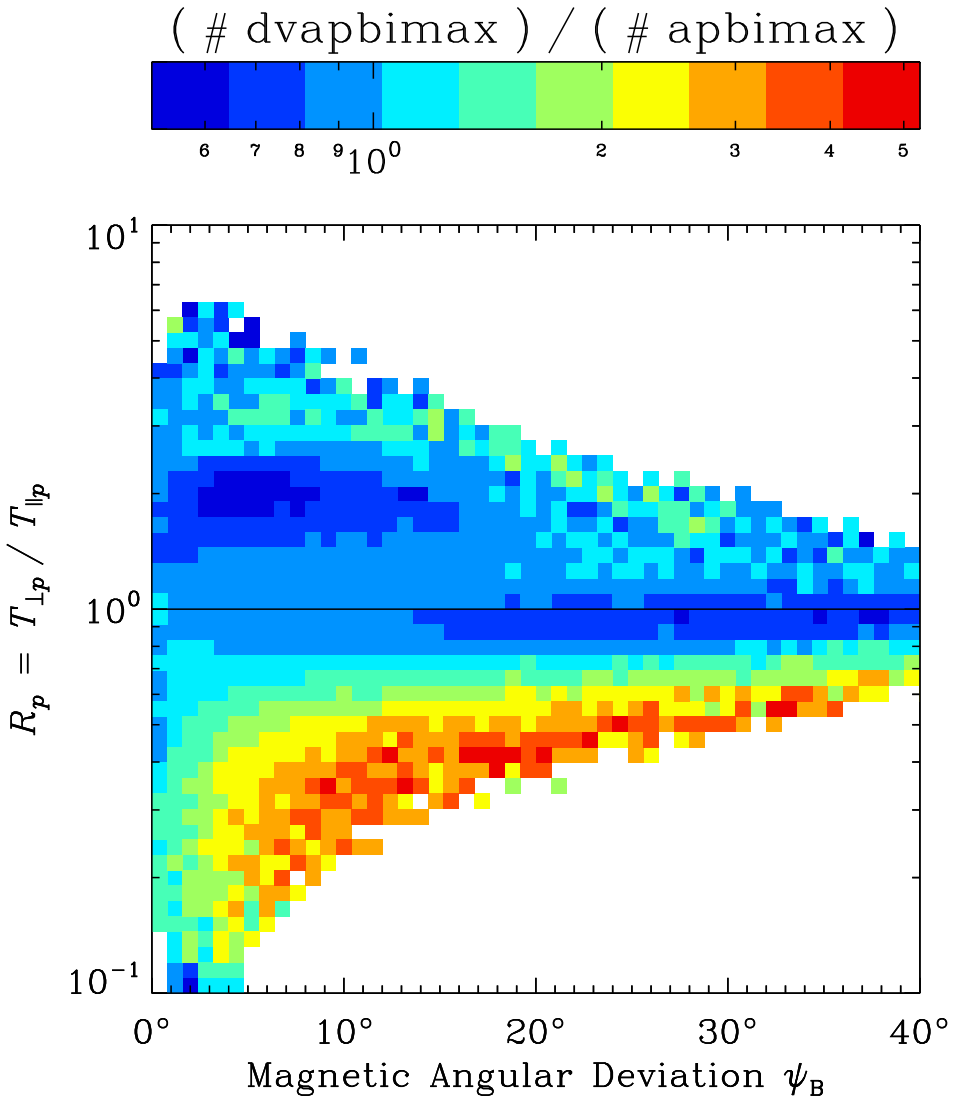

Figure 3.5.— Occurrences of $(\psi_{\mathbf{B}}, R_p)$-values in the `dvapbimax` data relative to those in the `apbimax` data. The color assigned to each $(\psi_{\mathbf{B}}, R_p)$-bin corresponds to the ratio of the number of `dvapbimax` data in that bin to the number of `apbimax` data. In order to suppress the effects of counting statistics, only bins with at least 16 data from each analysis code are shown.

tines (Moré et al., 1980). On the whole, `mpfit` is far more robust and flexible than `curvefit`, so `dvapbimax` could include a more sophisticated non-linear analysis than `apbimax`.

In particular, `mpfit` allows its user to hold the values of some fit parameters fixed while best-fit values are calculated for the others. As stated above, `apbimax`'s non-linear analysis of a *Wind*/FC ion spectrum first fits for the proton bulk parameters and then for the proton and α-particle parameters together. However, utilizing the features of `mpfit`, `dvapbimax` fits for the proton parameters, then for the α-parameters (while holding the values of the proton parameters fixed), and finally fits for the proton and α-particle parameters together.

This process of fitting the response of each species independently before fitting their joint response is particularly useful in handling a proton *beam*, which occurs when a fraction of the protons form a second bi-Maxwellian population that usually has a slightly-higher bulk speed than that of the proton *core* (Feldman et al., 1973; Asbridge et al., 1974). Figure 3.6 shows a portion of a typical *Wind* ion spectrum that features a prominent proton beam. Like most such spectra, the density and speed of the beam relative to the core are not high enough for the beam to appear as its own spectral peak in these plots; instead it manifests as a distortion to the high-speed side of the proton core's peak. This type of distortion tends to cause both the moments and non-linear analysis to produce a proton VDF that is too wide as it is essentially stretched to accommodate the two overlapping spectral peaks. To correct this, `dvapbimax` searches for any strong outliers from the initial fit of the proton parameters that are consistent with the effects of a proton beam. The algorithm then eliminates these from the subsequent joint fit of the proton and α-particle parameters so that the best-fit proton parameters describe the proton core only.

While α-particle beams are rarely (if ever) observed in *Wind* ion spectra, fitting for the

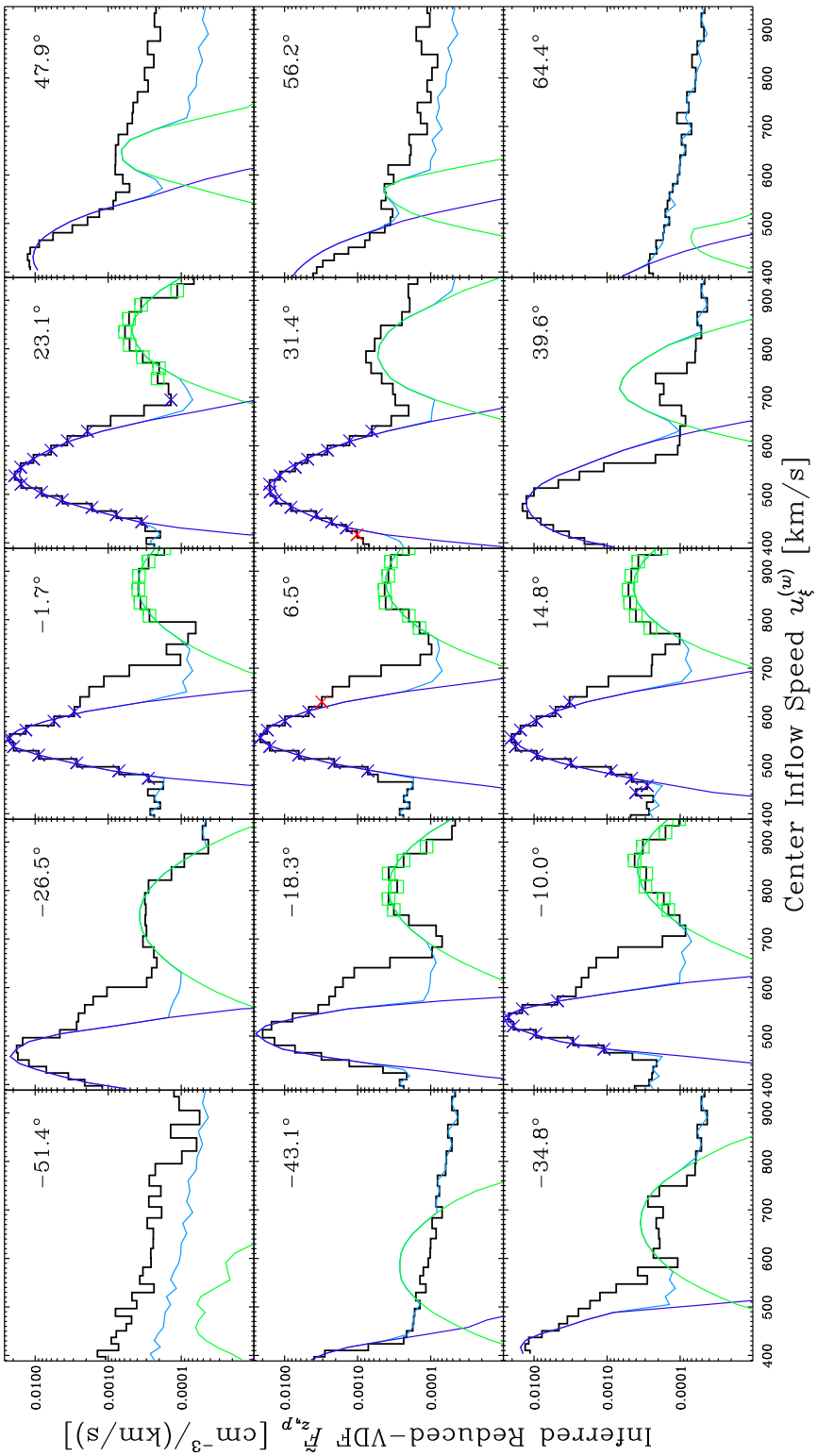

Figure 3.6.— A partial *Wind*/FC ion spectrum from 00:07 UTC on 09 January 2008 that exemplifies the effects of a proton beam on a spectrum and the handling of this phenomenon by `dvapbimax`. The data points corresponding to the beam do not have blue ×'s because `dvapbimax` successfully excluded them from its joint fit of the proton and α-particle parameters.

α-particle parameters brings its own problems. For example, complications often arise when the α-particles are particularly hot and/or fast relative to the protons. In particular, these conditions can cause `dvapbimax` to make poor initial guesses of the α-particle fit parameters and consequently to misidentify α-particle points during point selection. Ironically, part of the problem is that runs of `mpfit` (or `curvefit` for that matter) generally do not explicitly fail; instead, the code converges but does so to physically unreasonable values for the fit parameters. To compensate for this, `dvapbimax` uses a series of checks to assess the validity of parameter values. If any check fails, `dvapbimax` generates a revised initial guess of the α-particles' parameters, reselects the α-particle points, and reruns the fit of the α-particle VDF. In this way, `dvapbimax` can recover from a poor fit by revising its fit strategy.

Chapter 4

Selecting *Wind*/FC Ion Spectra for Statistical Analysis

The `dvapbimax` software (see Section 3.3.2) was used to analyze the 4 798 309 *Wind*/FC ion spectra captured from late-1994 (i.e., launch) to mid-2010. However, the results from only a fraction of these were suitable for the statistical analysis described in the proceeding chapters. Section 4.1 details the various criteria used to select the set of spectra whose `dvapbimax` output was ultimately used in this study. Some of the basic properties of this final dataset are presented in Section 4.2.

4.1 Selection Criteria

A given spectrum was only included in the final dataset if it satisfied three different sets of selection criteria, each of which is described below. The first (and most fundamental) set of criteria were based on *Wind*'s location relative to Earth and on the convergence of the

`dvapbimax` algorithm. The criteria in the second set established standards for the quality of the `dvapbimax` fits. The third was actually only a single criterion and specified a maximum collisional age for the spectra.

4.1.1 Spacecraft Location and Algorithm Convergence

The most fundamental selection criterion for a spectrum was that the *Wind* spacecraft was actually in the solar wind when it was recorded. Until recently, *Wind* spent a significant portion of its time near or inside Earth's magnetosphere (see Section 2.1). As the physics associated with the magnetosphere is distinct from that of the solar wind (Prölss, 2004), only spectra from when *Wind* was far outside of the Earth's bow shock were selected. In particular, based on Merka et al. (2003), it was required that

$$\frac{r^{(s)}_{x_{\mathrm{GSE}}}}{R_{\oplus}} > 30 - \frac{3}{250}\,\frac{\left(r^{(s)}_{y_{\mathrm{GSE}}}\right)^2 + \left(r^{(s)}_{z_{\mathrm{GSE}}}\right)^2}{R^2_{\oplus}}\ , \tag{4.1}$$

where $R_{\oplus}$ is the radius of the Earth and

$$\mathbf{r}^{(s)} = r^{(s)}_{x_{\mathrm{GSE}}}\,\hat{\mathbf{x}}_{\mathrm{GSE}} + r^{(s)}_{y_{\mathrm{GSE}}}\,\hat{\mathbf{y}}_{\mathrm{GSE}} + r^{(s)}_{z_{\mathrm{GSE}}}\,\hat{\mathbf{z}}_{\mathrm{GSE}}\ , \tag{4.2}$$

denotes the position vector of the spacecraft in the geocentric solar ecliptic (GSE) coordinate system (Russell, 1971). The boundary of the region specified by Equation 4.1 is a cylindrically symmetric paraboloid with its axis along the x_{GSE}-axis.

Another important selection criterion was that the fitting algorithm have converged in a reasonable number of iterations. Most of the spectra that did not meet this criterion had a weak α-particle signal. When the α-particle number density is particularly low, the α-particle spectral peak can fall below the *Wind*/FC detection threshold. Likewise, if the

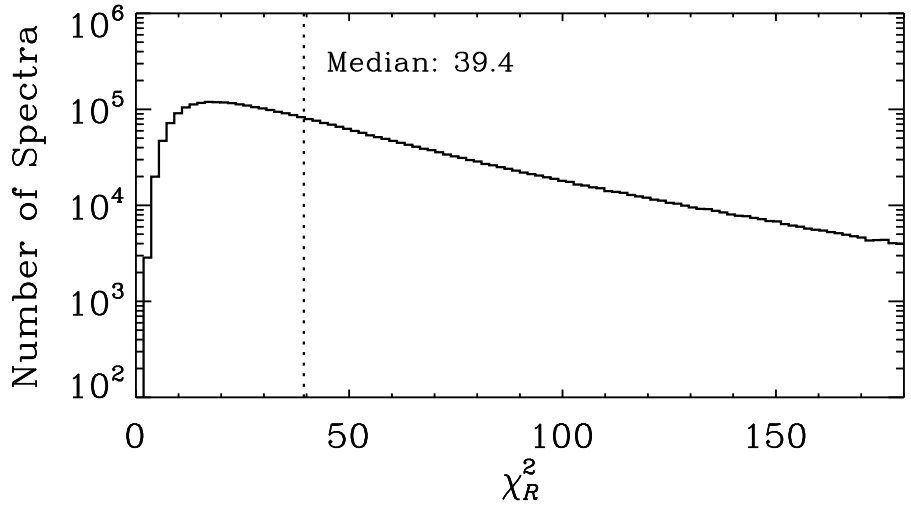

Figure 4.1.— Histogram of χ^2_R for the spectra that met the selection criteria in Section 4.1.1

proton temperature is particularly high, the proton spectral peak can become wide enough to envelop the relatively small α-particle peak.

In all, 3 829 271 spectra (i.e., 79.8% of the total) met these criteria based on spacecraft location and algorithm convergence. Figure 4.1 shows a histogram of χ^2_R-values (Taylor, 1997; Bevington & Robinson, 2003) from the fits of these spectra, which indicates that the typical χ^2_R-values returned by the `dvapbimax` code were quite large: the median was, in fact, 39.4. Ideally, a fit should have a χ^2_R-value of about unity, but this assumes that the fit model adequately captures the underlying physical processes and that the uncertainties in the measurements take into account all sources of error. For several reasons, these assumptions are not entirely valid in the `dvapbimax` analysis, each of which contributes to the inflation of the resultant χ^2_R-values. First, the estimated uncertainties in the measured Faraday cup currents only accounted for the minimum current that could be digitally encoded by the detector. This method neglects, for example, the measurement noise of the detector

as well as uncertainties in the effective collecting area of the cup as a function of particle inflow-direction (see Section 2.3). Second, the `dvapbimax` code relies on the assumption of supersonic flow, which allows the effective collecting area to be removed from the integrand of the model (see Section 2.3.2). While this assumption eliminates the need for numerical integration, it introduces additional uncertainty that is not quantified in the analysis. Third, the calculation of χ^2_R tacitly assumes that the ion VDF's actually are bi-Maxwellian. While a bi-Maxwellian usually provides a reasonable analytic model of an ion distribution's core, deviations, especially in the wings of the distribution, are often evident. Fourth, as previously discussed, approximately 90 seconds are required to produce sufficient data for a typical *Wind*/FC ion spectrum. However, higher-cadence measurements with other in situ instruments have revealed significant variations in ion parameter values on these time scales.

Figures 4.2 and 4.3 together contain a histogram for each of the ten `dvapbimax` fit parameters. The seven parameters shown in Figure 4.2 (i.e., n_p, n_α, v_{xp}, $w_{\perp p}$, $w_{\parallel p}$, $w_{\perp\alpha}$, and $w_{\parallel\alpha}$) are grouped together because a value of zero for any of these would be physically unrealistic; with the exception of v_{xp}, which should always be negative, each of these parameters should always be positive. In contrast, the three parameters considered in Figure 4.2 (i.e., v_{yp}, v_{zp}, and $\Delta v_{\parallel\alpha p}$) can realistically take on positive or negative values.

A histogram of the relative uncertainty in each parameter in Figure 4.2 is shown in Figure 4.4; one for the absolute uncertainty in each parameter in Figure 4.3 is shown in Figure 4.5. Many of these uncertainties (relative and absolute) seem unreasonably large. However, these values do not represent true uncertainties in the fit parameters since, like the χ^2_R-values, they incorporate deviations from the bi-Maxwellian model and rapid variations in plasma conditions. Additionally, each uncertainty has been scaled by χ_R, which further inflates its value.

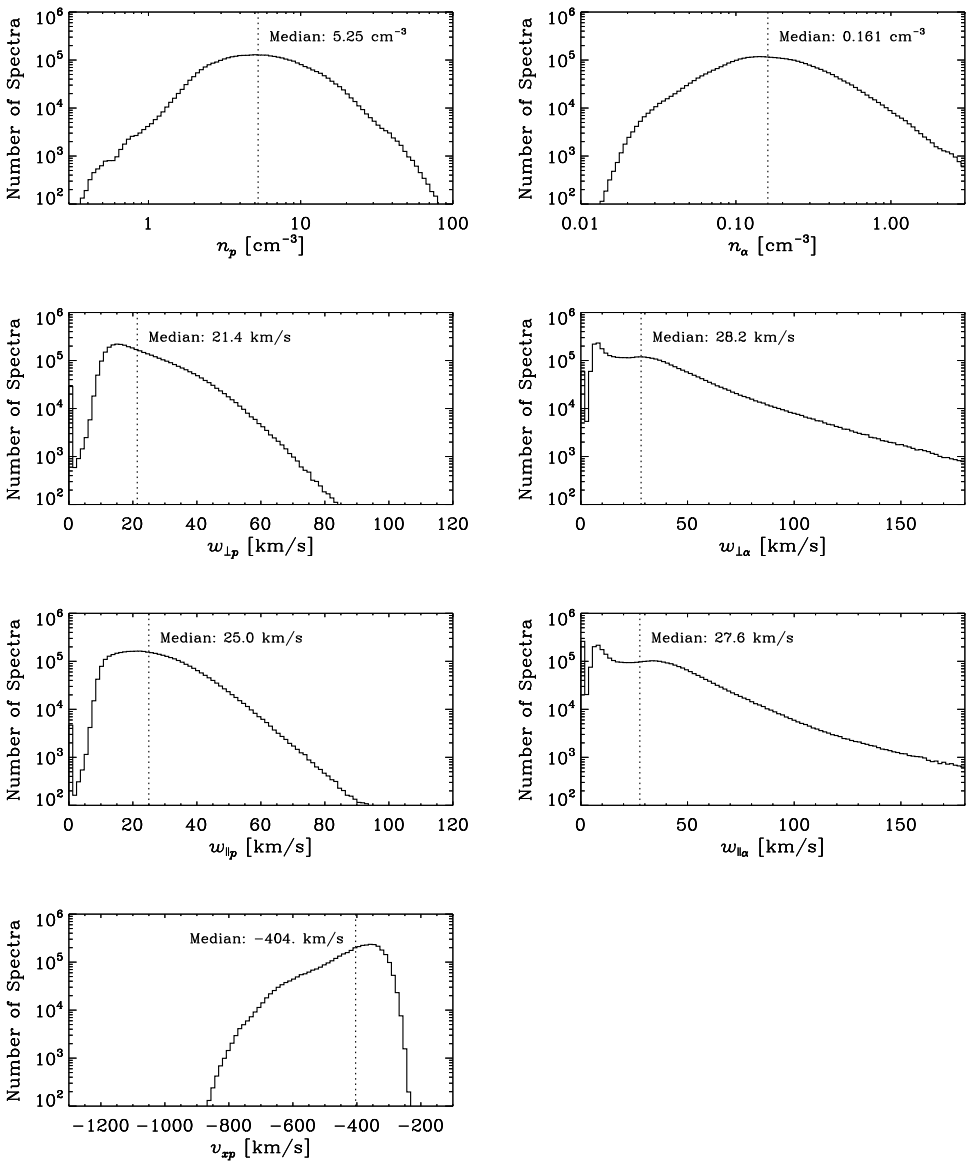

Figure 4.2.— Histograms of seven of the ten `dvapbimax` fit parameters for the spectra that met the selection criteria in Section 4.1.1. These seven fit parameters are distinct from the other three in that values of zero are physically unrealistic. Histograms of the remaining three are given in Figure 4.3. In this figure, the binning of n_p- and n_α-values (top row) is logarithmic, but the other five parameters are binned linearly.

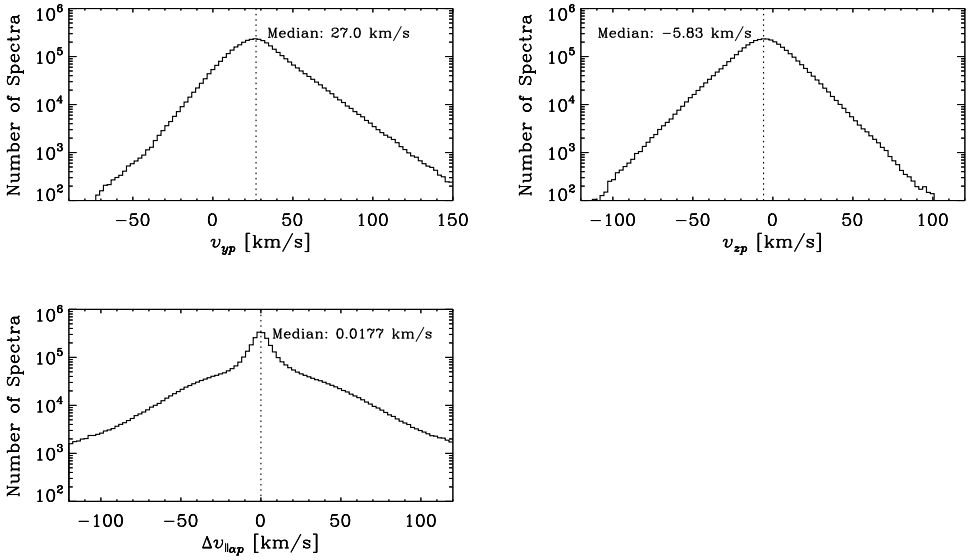

Figure 4.3.— Histograms of three of the ten `dvapbimax` fit parameters for the spectra that met the selection criteria in Section 4.1.1. These three fit parameters are distinct from the other seven in that values of zero are physically realistic. Histograms of the remaining seven are given in Figure 4.2. The median value of v_{yp} (unlike that of v_{xp}) is appreciably different from zero: more so than can be accounted for by the observed spread of values. Rather, this offset resulted from the measurements having been made in the frame of reference of the *Wind* spacecraft, which moves approximately with the Earth as the planet orbits the Sun. On average, Earth's orbital velocity is about 30 km/s in the $\hat{\mathbf{y}}_{\mathrm{GSE}}$-direction.

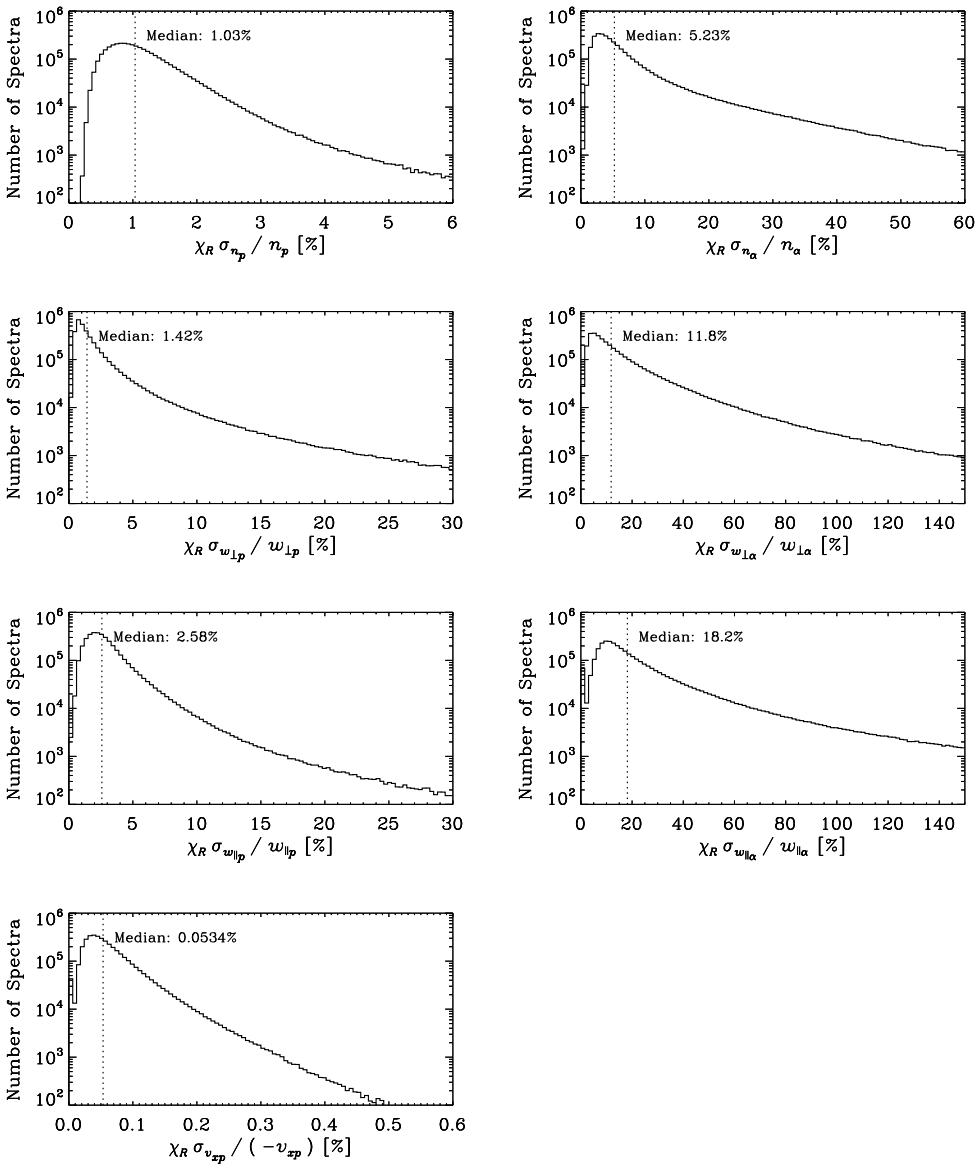

Figure 4.4.— Histograms of uncertainties in seven of the ten `dvapbimax` fit parameters for the spectra that met the selection criteria in Section 4.1.1. Each uncertainty has been scaled by χ_R and is given as a percentage relative to its corresponding parameter. These seven fit parameters are distinct from the other three in that values of zero are physically unrealistic (see Figure 4.2). Histograms of uncertainties in the remaining three are given in Figure 4.5.

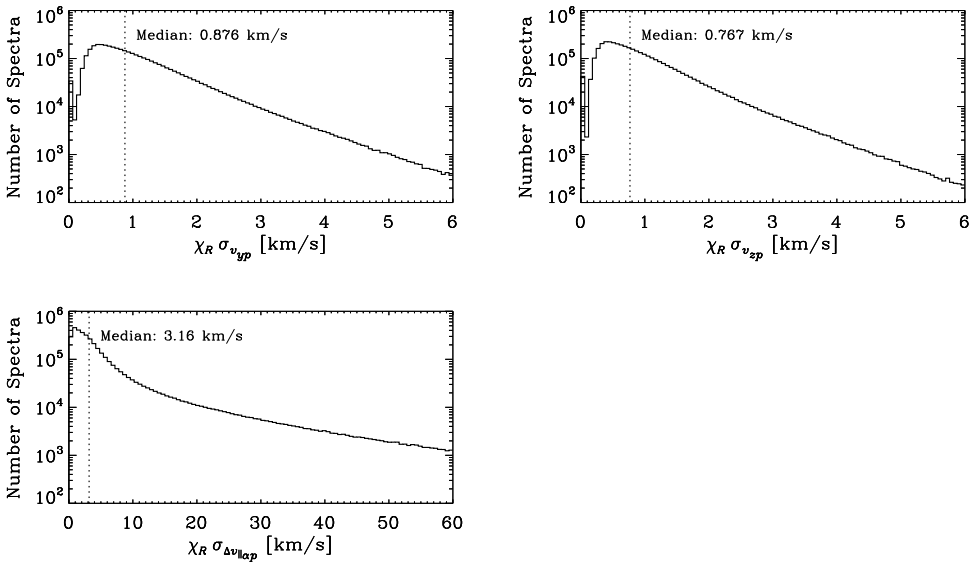

Figure 4.5.— Histograms of uncertainties in three of the ten `dvapbimax` fit parameters for the spectra that met the selection criteria in Section 4.1.1. Each uncertainty has been scaled by χ_R. These three fit parameters are distinct from the other seven in that values of zero are physically realistic (see Figure 4.3). Histograms of uncertainties in the remaining seven are given in Figure 4.4.

4.1.2 Fit Quality

The next set of criteria were based on the quality of each spectrum's fit. Since there were too many spectra for each to be individually studied by human eyes, the assessment of fit quality was based on predefined ranges for χ^2_R, the fit parameters, and the uncertainties in the fit parameters. The `dvapbimax` algorithm has ten fit parameters, so a total of twenty-one quantities were used to assess fit quality for the purposes of data selection. As summarized in Table 4.1, each of these quantities was assigned a minimum and a maximum, which were chosen by studying temporal trends and analyzing a subset of `dvapbimax` output in detail.

As stated in Section 4.1.1, the values of χ^2_R (see Figure 4.1) as well as those of the uncertainties (see Figures 4.4 and 4.5) are unusually high, but such large values do not reflect uncertainty in parameter values for the fits as much as the assumptions of the analysis. Nevertheless, the χ^2_R-values and uncertainty values can still be interpreted as indicators of fit quality. For example, lower χ^2_R-values tended to correspond to indicate better fits of the spectra — even when the χ^2_R-values are significantly greater than unity.

For a few spectra, the `dvapbimax` code returned a near-zero value for one of the seven fit parameters that physically cannot have a value of zero or for one of the uncertainties of any of the ten fit parameters. This phenomenon is manifest in some of the histograms in Figures 4.2, 4.4, and 4.5 as an unexpectedly large number of spectra in the lowest-valued bin. For example, when the `dvapbimax` code had difficulty separating the perpendicular and parallel temperature components of an ion species j, it occasionally returned a near-zero value for either $w_{\perp j}$ or $w_{\parallel j}$. Because of these types of errors, the criteria in Table 4.1 specify both a maximum and a minimum for each of the ten fit parameters and its corresponding uncertainty.

		Quantity	Minimum	Maximum
χ^2_R		χ^2_R	0	150
Fit Parameters		n_p	0.5	50.
		n_α	0.02	2.
		v_{xp}	$-1200.$	$-200.$
		v_{yp}	$-70.$	130.
		v_{zp}	$-100.$	100.
		$\Delta v_{\parallel \alpha p}$	$-100.$	100.
		$w_{\perp p}$	2.	100.
		$w_{\parallel p}$	2.	100.
		$w_{\perp \alpha}$	2.	150.
		$w_{\parallel \alpha}$	2.	150.
Uncertainties	Relative	$\chi_R \, \sigma_{n_p} \, / \, n_p$	0.1%	5.%
		$\chi_R \, \sigma_{n_\alpha} \, / \, n_\alpha$	0.5%	50.%
		$\chi_R \, \sigma_{v_{xp}} \, / \, (-v_{xp})$	0.01%	0.5%
		$\chi_R \, \sigma_{w_{\perp p}} \, / \, w_{\perp p}$	0.2%	25.%
		$\chi_R \, \sigma_{w_{\parallel p}} \, / \, w_{\parallel p}$	0.2%	25.%
		$\chi_R \, \sigma_{w_{\perp \alpha}} \, / \, w_{\perp \alpha}$	1.%	120.%
		$\chi_R \, \sigma_{w_{\parallel \alpha}} \, / \, w_{\parallel \alpha}$	1.%	120.%
	Abs.	$\chi_R \, \sigma_{v_{yp}}$	0.1 km/s	5. km/s
		$\chi_R \, \sigma_{v_{zp}}$	0.1 km/s	5. km/s
		$\chi_R \, \sigma_{\Delta v_{\parallel \alpha p}}$	0.1 km/s	50. km/s

Table 4.1: Selection criteria based on fit quality. As described in Section 4.1.2, minimum and maximum values were specified for twenty-one quantities: χ^2_R, each of the ten `dvapbimax` fit parameters, and each fit parameter's uncertainty. All of the uncertainties are scaled by χ_R, and seven of them are specified as relative (versus absolute) uncertainties. The asymmetry in the range of selected v_{yp}-values is explained in the caption to Figure 4.3

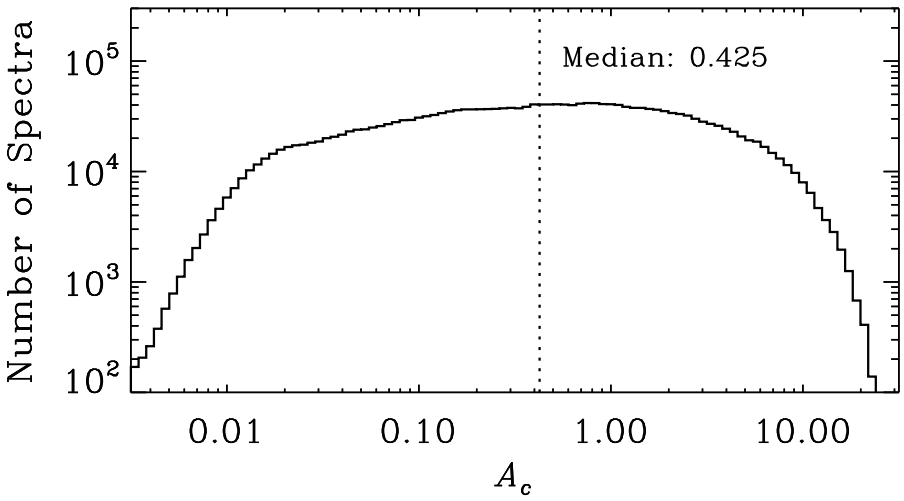

Figure 4.6.— Histogram of A_c for the spectra that met the selection criteria in Sections 4.1.1 and 4.1.2.

In all, 2 148 228 spectra (i.e., 44.8% of the total) met the selection criteria for fit quality listed in Table 4.1 as well as those specified in Section 4.1.1. Figure 4.6 shows a histogram of collisional age, A_c, (see Equation 1.14) for these spectra. The distribution of A_c-values, though quite wide, is roughly centered on a collisional age of unity. Thus, solar wind plasma at 1 AU can range from nearly collisionless to highly collisional.

Figure 4.7, which was generated from the same spectra as Figure 4.6, shows how $|\Delta v_{\alpha p}| \,/\, c_A$, $T_\alpha \,/\, T_p$, and R_p trend as functions of collisional age. Each parameter has its own plot, which was generated by dividing the plot area into a lin-log grid of bins. The spectra were then sorted into these bins, and the bin counts in each column were renormalized so that the most-populated bin had a value of unity. Thus, the color of each bin indicates, for its A_c-range, the relative number of spectra that occur in its range in $|\Delta v_{\alpha p}| \,/\, c_A$, $T_\alpha \,/\, T_p$, or R_p; darker colors correspond to higher rates.

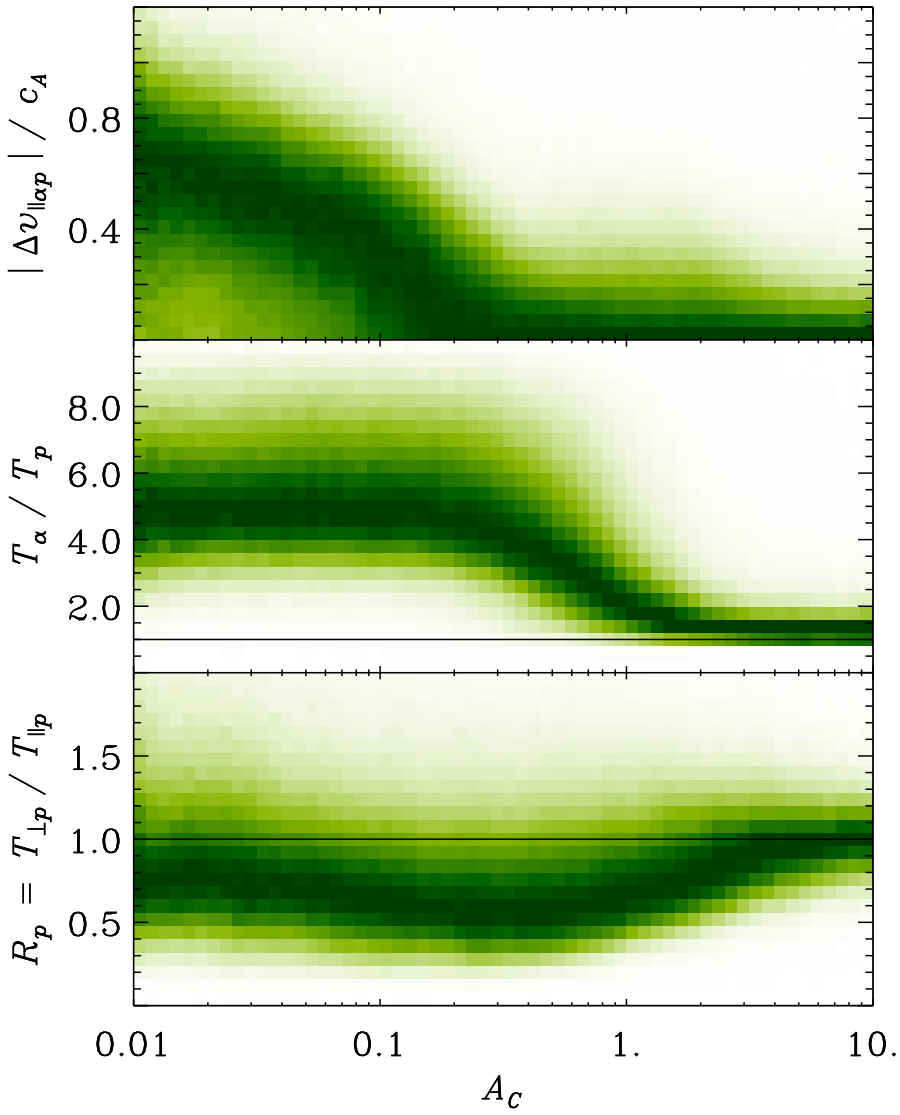

Figure 4.7.— Trends in $\left|\Delta v_{\parallel \alpha p}\right| / c_A$ (top), T_α / T_p (middle), and R_p (bottom) as functions of collisional age A_c for the spectra that met the selection criteria in Sections 4.1.1 and 4.1.2. In each plot, these spectra were sorted into a lin-log grid of bins, and then the bin counts in each column of were renormalized so that the most-populated bin had a value of unity. Larger renormalized values are indicated by darker colors.

Each of the parameters considered in Figure 4.7 (i.e., $|\Delta v_{\alpha p}| \,/\, c_A$, $T_\alpha \,/\, T_p$, and R_p) is an indicator of plasma equilibrium (or, more precisely, the lack thereof). In thermal equilibrium, the plasma would have neither differential flow nor temperature anisotropy, and all species in the plasma would have the same temperature. Based on these indicators, Figure 4.7 suggests that most collisionally old spectra (i.e., those for which $A_c \gg 1$) are close to thermal equilibrium. However, this figure also shows that collisionally young spectra (i.e., those for which $A_c \ll 1$) tend to have the most dramatic non-equilibrium features. In these spectra, $T_\alpha \approx T_p$ is virtually never observed, and $|\Delta v_{\alpha p}| \,/\, c_A \approx 0$ and $R_p \approx 1$ are relatively rare. Figure 4.7 and similar figures produced by Kasper et al. (2008) and Bale et al. (2009) have been interpreted as demonstrating the important role that collisions play in bringing solar wind plasma into thermal equilibrium.

4.1.3 Collisional Age

The final selection criterion was that each *Wind*/FC ion spectrum be collisionally young: i.e., that (based on the fit values of the `dvapbimax` parameters)

$$A_c \leq 0.3 \ . \tag{4.3}$$

The selection of only collisionally young plasma was important for several reasons. First, as discussed in Section 4.1.2, collisional relaxation gradually isotropizes plasma (Kasper et al., 2008; Bale et al., 2009), which can mask any prior effects of anisotropy-driven instabilities. For example, Figure 4.7 clearly shows how R_p tends toward unity as A_c increases. Second, collisional relaxation gradually brings the various particles species into thermal equilibrium. Such coupling of bulk parameters can complicate the identification of the ion species driving an instability. Third, the statistical analysis of collisionally young spectra can be more

Parameter	Median
$n_\alpha \,/\, n_p$	0.0418
$\beta_{\parallel p}$	0.835
$\beta_{\parallel \alpha}$	0.166
R_p	0.746
R_α	0.759
$T_{\parallel\alpha} \,/\, T_{\parallel p}$	5.11
$c_A \,/\, c$	1.64×10^{-4}
$\left\lvert \Delta v_{\parallel \alpha p} \right\rvert \,/\, c_A$	0.330

Table 4.2: Median values of select, dimensionless parameters for the spectra that met all selection criteria specified in Section 4.1.

legitimately compared with the results of linear Vlasov theory, which explicitly assumes a collisionless plasma (see Chapter 5).

In all, 927 711 (i.e., 19.3%) of *Wind*/FC ion spectra satisfied the criterion specified by Equation 4.3 as well as those in Sections 4.1.1 and 4.1.2. These formed the final dataset that was used for the statistical analysis described in the remainder of this dissertation.

4.2 Properties of the Final Dataset

This section gives a general overview of this dataset and introduces a simple model for anisotropy correlation. Particular attention is given to temperature anisotropy correlation because of the strong effects that this phenomenon can have on instabilities (see Chapters 6 and 7).

4.2.1 Typical Parameter Values

Table 4.2 lists the median values of certain important dimensionless parameters for the dataset, most of which are consistent with prior observations of solar wind plasma (both with *Wind* and with other spacecraft). These values formed the basis of the default parameter values used in this study's linear Vlasov calculations (see Table 5.2).

Like prior studies (e.g., Kasper et al., 2008), this project found the α-particle temperature to be significantly higher than the proton temperature in collisionally young solar wind. Table 4.2 lists the median value of $T_{\parallel\alpha} \,/\, T_{\parallel p}$ as 5.21, but in collisionally old wind, this ratio is usually quite close to unity. Thus, while in collisionally old spectra these two species generally have the same temperature, the α-particles in collisionally young plasma tend to have a thermal speed that is approximately equal to (or even slightly greater than) that of the protons[1] (see Figure 4.7).

It is also noteworthy that the median values of the ratios $c_A \,/\, c$ (i.e., the Alfvén speed relative to the speed of light) and $\Delta v_{\parallel\alpha p} \,/\, c_A$ (i.e., the α-proton parallel differential flow relative to the Alfvén speed) were so small. Figure 4.8 shows a histogram of each ratio, and indeed $c_A \,/\, c$ never approaches unity and $\Delta v_{\parallel\alpha p} \,/\, c_A$ only rarely does.

The selection of only collisionally young spectra somewhat biases the final dataset in favor of fast solar wind (see Equation 1.14), which numerous studies have shown to have an origin and evolution that are distinct from those of slow solar wind. A histogram of v_p-values from the final dataset is shown in Figure 4.9. The almost total lack of spectra with $v_p < 300$ km/s confirms a bias in favor of fast solar wind. However, this bias does not seem

[1]Because an α-particle is 4.0 times more massive than a proton, $w_{\parallel\alpha} = w_{\parallel p}$ corresponds to $T_{\parallel\alpha} = 4.0\, T_{\parallel p}$ (see Equation 1.6).

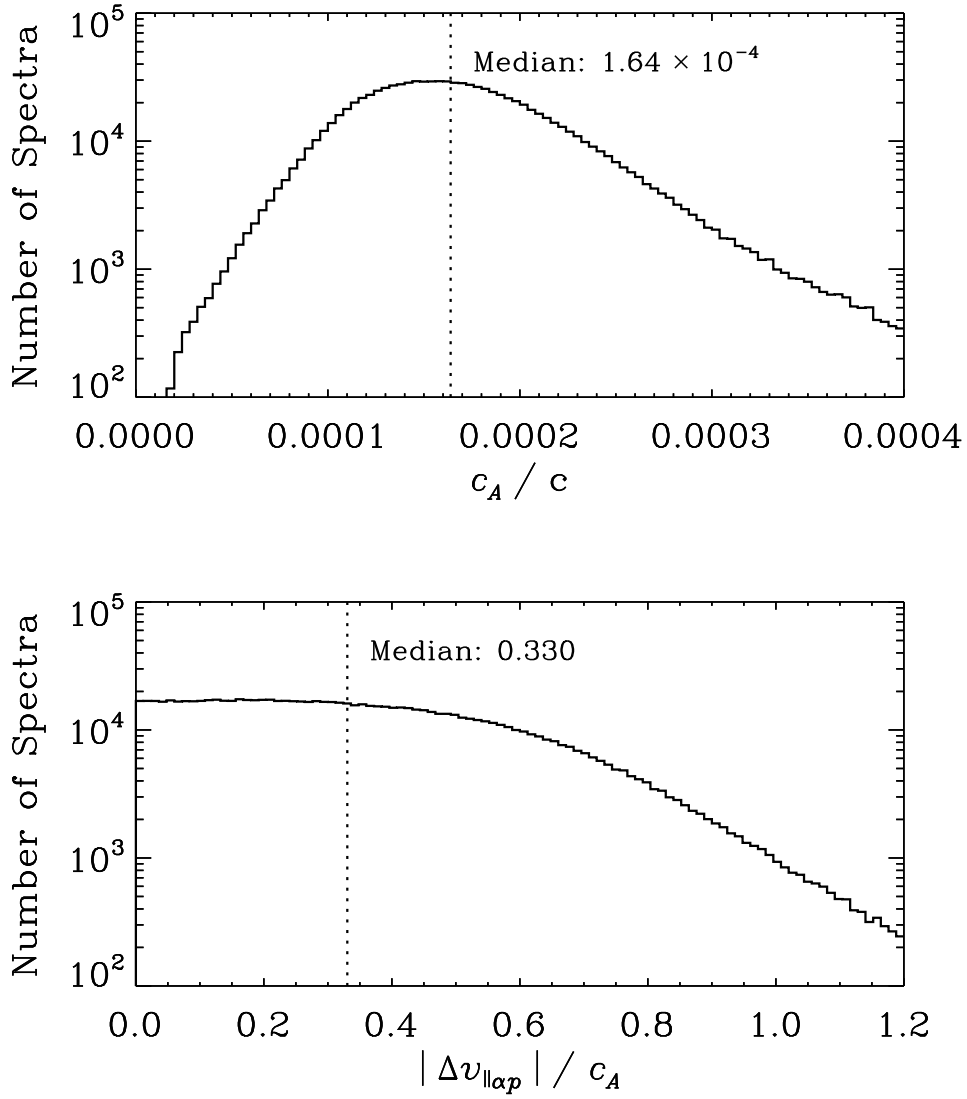

Figure 4.8.— Histograms of $c_A \,/\, c$ (top) and $\left|\Delta v_{\parallel \alpha p}\right| \,/\, c_A$ (bottom) for the spectra that met all selection criteria in Section 4.1.

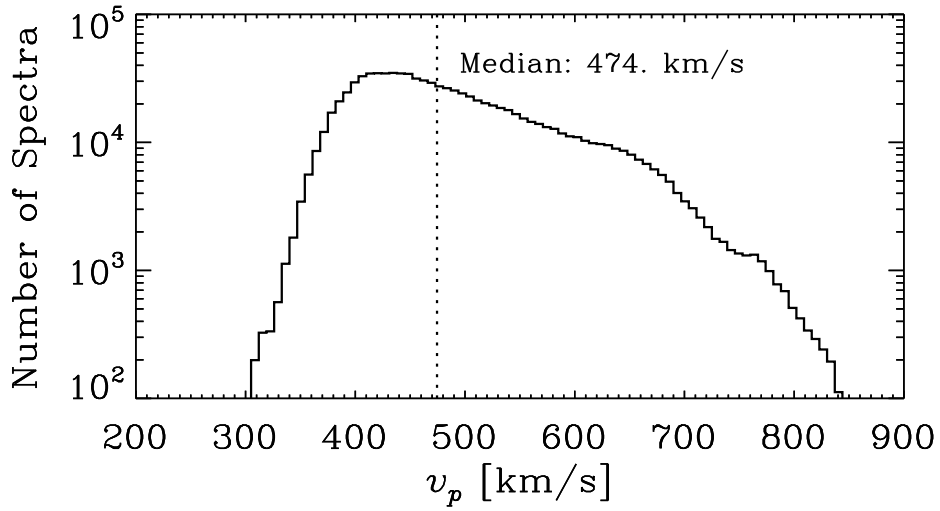

Figure 4.9.— Histogram of v_p for the spectra that met all selection criteria in Section 4.1.

to be particularly strong since the median value of v_p is still only 474 km/s.

4.2.2 Temperature Anisotropy Correlation

Even in collisonless plasma, the bulk parameters of different particle species can still be correlated with each other. Since this study considered instabilities driven by ion temperature anisotropy, an investigation of anisotropy correlation was warranted. For a given value of R_j (where $j = p$ or α), what is the "typical" value of $R_{j'}$ (where $j' = \alpha$ or p)?

Figure 4.10 shows plots of median $R_{j'}$ versus R_j for (a) $j = p$ and (b) $j = \alpha$. To generate each plot, the selected data described above were sorted into logarithmically-spaced R_j-bins. For each of these bins, a blue diamond indicates its median values of R_j and $R_{j'}$, and a vertical blue line indicates the range of the central-68% of its $R_{j'}$-values. Note that the plots are not simply inverses of each other because each has a different binning: Figure 4.10(a)

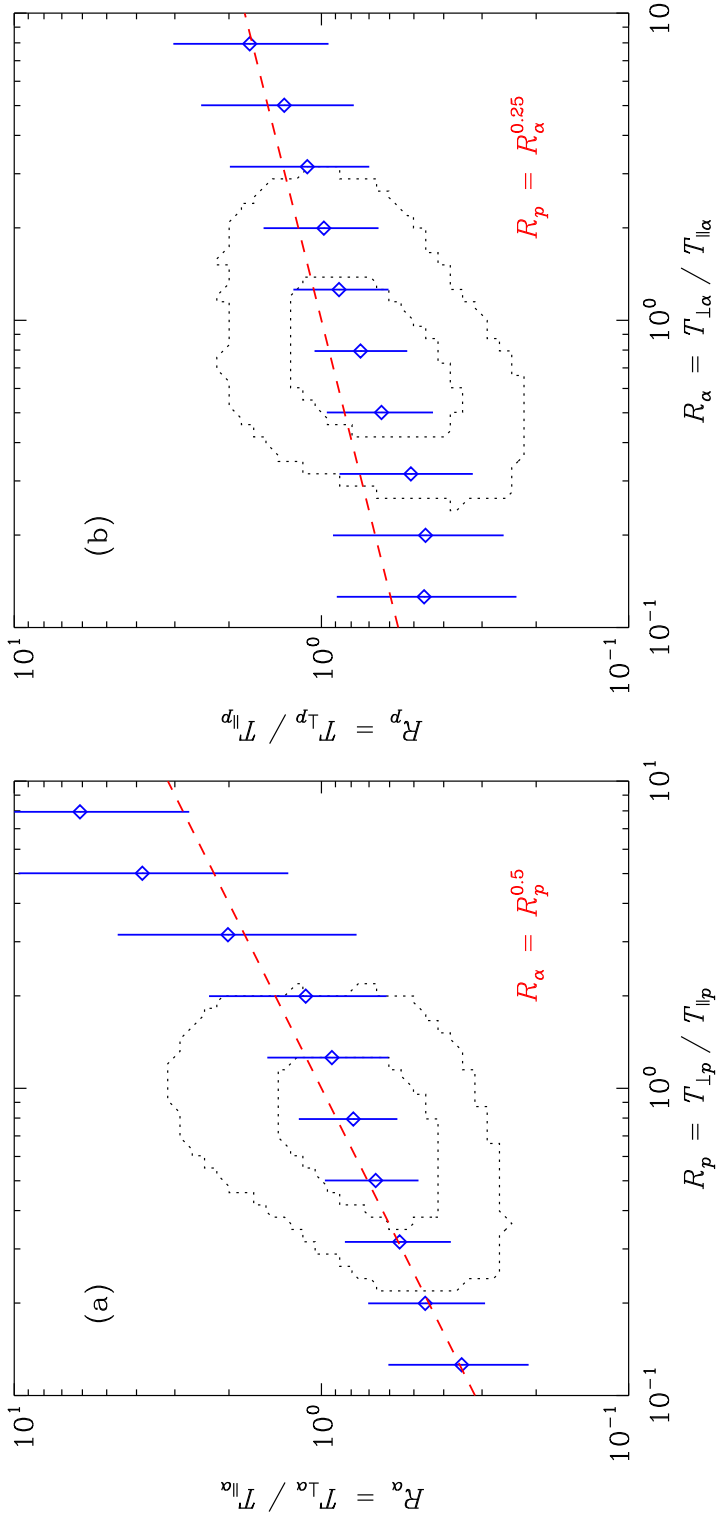

Figure 4.10.— Plots of (a) median R_α-value as a function of R_p and (b) median R_p-value as a function of R_α for the spectra that met all selection criteria in Section 4.1.

shows typical values of R_α for various R_p-values, and Figure 4.10(b) vice versa.

The plots in Figure 4.10 clearly show positive correlation between R_p and R_α: when one species is significantly anisotropic, the other usually is as well. Unfortunately, as is discussed in Chapters 6 and 7, the analysis of anisotropy-driven instabilities becomes complicated when multiple species are anisotropic. If $R_j \neq 1$ and $R_{j'} = 1$, then clearly species j drives any ensuing instability. However, if R_j and $R_{j'}$ are both non-unity, each ion species is contributing internal free energy toward driving an instability. If R_j and $R_{j'}$ are also comparable in value, the formalism of a *driving species* fails altogether.

To facilitate the exploration of this issue, the correlation of $R_{j'}$ to R_j was quantified by ζ, which was defined such that

$$R_{j'} = R_j^{\zeta} \ . \tag{4.4}$$

Obviously, $\zeta = 0$ corresponds to species j' being isotropic for all values of R_j. For values of $\zeta > 0$, though, both species j and species j' are anisotropic. However, so long as $0 \leq \zeta \ll 1$, species j' is far less anisotropic than species j, and j can be safely labeled as the *primary* driver of any temperature anisotropy instability in the plasma.

The definition of ζ in Equation 4.4 was chosen primarily to avoid the complex situation of $R_j \approx R_{j'}$. Nevertheless, this model for anisotropy correlation is reasonably consistent with observations. The red, dashed lines in Figure 4.10 correspond to (a) $\zeta = 0.5$ and (b) $\zeta = 0.25$. These values of ζ are not from a fit and are simply intended to show that the correlation between ion temperature anisotropies can be roughly captured by Equation 4.4.

Chapter 5

Linear Vlasov Theory of Temperature Anisotropy Instabilities

The focus of this dissertation project was on kinetic microinstabilities driven by ion temperature anisotropy, and this chapter provides an introduction to the analysis of these instabilities with linear Vlasov theory. An overview of microinstabilities in general is given in Section 5.1. Section 5.2 discusses the the fundamental principles of linear Vlasov theory, which is used in Section 5.3 to derive the dispersion relation for electromagnetic waves in uniform, magnetized plasma. The four instabilities associated with ion temperature anisotropy are introduced in Section 5.4, and the software used in this study to calculate their growth rates is described in Section 5.5.

5.1 Introduction to Plasma Microinstabilities

In general, many different types of instabilities can develop in plasmas. While some of these are associated with macroscopic phenomena such as gradients in bulk velocity or density, microinstabilities develop from non-equilibrium features of the plasma's VDF's. In thermal equilibrium, each particle species has a Maxwellian VDF and all species share the same temperature and bulk speed. Under these conditions, the plasma is stable to all microinstabilities. However, as discussed in Section 1.2.2, a wide variety of processes (e.g., double adiabatic expansion and the anisotropic dissipation of turbulence) in the solar wind cause the plasma to develop various non-thermal features. These deviations from equilibrium are entropically unfavorable and (if sufficiently strong) can cause instabilities to develop.

Various methods exist for the theoretical study of plasma instabilities. Perhaps the most basic approach is to use magnetohydrodynamics (MHD), which is built upon Maxwell's equations and the fluid conservation equations (Cowling, 1957; Kulsrud, 1983; Baumjohann & Treumann, 1997; Treumann & Baumjohann, 1997). Though MHD is often used in the study of plasma macroinstabilities, it provides, per se, no mechanism for the analysis of microinstabilities (Gary, 1993; Kasper, 2002).

Consequently, this study exclusively employed linear Vlasov analysis, which uses a linear expansion of the Vlasov equation to explore the behavior of small-amplitude, sinusoidal waves in plasma (Gary, 1993; Baumjohann & Treumann, 1997). Unlike MHD, this method explicitly assumes that the plasma is collisionless and can be used to derive the growth rates of kinetic microinstabilities.

Of course, linear theory does have its own fundamental limitations. For example, since

all equations in linear theory are (by definition) only expanded to first order, only small-amplitude perturbations can be considered. Thus, while linear theory can be used to determine the initial growth rate of an instability, it provides no information about the instability's longterm evolution. Consequently, linear theory cannot be used to study how the actions of instabilities affect the bulk parameters of plasma. Instead, more sophisticated methods are necessary, which usually requires the abandonment of analytic methods in favor of numerical ones: e.g., the "brute force" simulation of each particle's position and momentum with time, "hybrid" simulations that model some species as individual particles and others as a bulk fluid, and "particle-in-cell" codes (Gary, 1993; Matteini et al., 2011; Chandran et al., 2011). However, these methods necessitate a great deal of computational power and therefore were eschewed for this study.

5.2 Introduction to Linear Vlasov Theory

This section provides an overview of the Vlasov equation and how it can be linearized to study plasma waves. The specific case of electromagnetic waves in uniform, magnetized plasma is treated in much more detail in Section 5.3.

5.2.1 The Vlasov Equation

For a particle species j with a VDF $f_j = f_j(t, \mathbf{r}, \mathbf{u})$ (where $\mathbf{r}$ is particle position and $\mathbf{u}$ is particle velocity), the Boltzmann transport equation is

$$\frac{df_j}{dt} = \left.\frac{\partial f_j}{\partial t}\right|_{\text{coll}}, \tag{5.1}$$

where the left-hand side denotes the total derivative of f_j and the right-hand side encapsulates the influences of collisions among particles on the evolution of f_j (Gary, 1993). In the absence of collisions, the latter vanishes. Then, applying the chain rule to the former gives

$$\frac{\partial f_j}{\partial t} + \mathbf{u} \cdot \frac{\partial f_j}{\partial \mathbf{r}} + \frac{\mathbf{F}}{m_j} \cdot \frac{\partial f_j}{\partial \mathbf{u}} = 0 \ , \tag{5.2}$$

where $\mathbf{F} = \mathbf{F}(t, \mathbf{r}, \mathbf{u})$ is the net force on the particles. The Vlasov equation comes from assuming that the only forces associated with the electric field, $\mathbf{E} = \mathbf{E}(t, \mathbf{r})$, and the magnetic field, $\mathbf{B} = \mathbf{B}(t, \mathbf{r})$, act on the plasma:

$$\frac{\partial f_j}{\partial t} + \mathbf{u} \cdot \frac{\partial f_j}{\partial \mathbf{r}} + \frac{q_j}{m_j} (\mathbf{E} + \mathbf{u} \times \mathbf{B}) \cdot \frac{\partial f_j}{\partial \mathbf{u}} = 0 \ . \tag{5.3}$$

In general, it is quite challenging to solve the Vlasov equation analytically. The most obvious difficulty is that this differential equation involves seven independent variables: t, the three components of $\mathbf{r}$, and the three components of $\mathbf{u}$. In full generality, f_j is a function of all seven of these variables and the fields $\mathbf{E}$ and $\mathbf{B}$ are functions of the first four. Additionally, because all particles in the plasma contribute to $\mathbf{E}$ and $\mathbf{B}$, the Vlasov equation written for one particle species is implicitly coupled to those written for all other species. Therefore, even though Equation 5.3 is only written for a single species j, any solution must simultaneously consider all of the plasma's species.

The linear analysis of the Vlasov equation mitigates some of these difficulties by assuming that the temporal variations in f_j, $\mathbf{E}$, and $\mathbf{B}$ can be approximated by a plane-wave

perturbation. More formally,

$$\begin{aligned} f_j(t,\mathbf{r},\mathbf{u}) &= f_j^{(0)}(\mathbf{r},\mathbf{u}) + f_j^{(1)}(t,\mathbf{r},\mathbf{u}) \\ &= f_j^{(0)}(\mathbf{r},\mathbf{u}) + f_j^{(1)}(\mathbf{k},\omega,\mathbf{u}) \exp[i\,(\mathbf{k}\cdot\mathbf{x} - \omega\,t)] \ , \\ \mathbf{E}(t,\mathbf{r}) &= \mathbf{E}^{(0)}(\mathbf{r}) + \mathbf{E}^{(1)}(t,\mathbf{r}) \\ &= \mathbf{E}^{(0)}(\mathbf{r}) + \mathbf{E}^{(1)}(\mathbf{k},\omega) \exp[i\,(\mathbf{k}\cdot\mathbf{x} - \omega\,t)] \ , \text{ and} \\ \mathbf{B}(t,\mathbf{r}) &= \mathbf{B}^{(0)}(\mathbf{r}) + \mathbf{B}^{(1)}(t,\mathbf{r}) \\ &= \mathbf{B}^{(0)}(\mathbf{r}) + \mathbf{B}^{(1)}(\mathbf{k},\omega) \exp[i\,(\mathbf{k}\cdot\mathbf{x} - \omega\,t)] \ , \end{aligned} \tag{5.4}$$

where $\mathbf{k}$ is the wavevector and ω is the angular frequency. Under the usual convention, $\mathbf{k}$ is taken to be real-valued, and ω is taken to be complex-valued such that

$$\omega = \omega_r + i\,\gamma \ , \tag{5.5}$$

where $i = \sqrt{-1}$ is the imaginary unit. The imaginary component, γ, is referred to as the *growth rate* and indicates how the wave's amplitude changes in time; the wave decays (exponentially) if $\gamma < 0$ but grows (exponentially) if $\gamma > 0$.

In linear Vlasov analysis, the linear expansions of f_j, $\mathbf{E}$, and $\mathbf{B}$ (see Equation 5.4) are combined with the Vlasov equation (see Equation 5.3) as well as Maxwell's equations:

$$\frac{\partial}{\partial \mathbf{r}} \cdot \mathbf{E} = \frac{\rho}{\epsilon_0} \ , \tag{5.6a}$$

$$\frac{\partial}{\partial \mathbf{r}} \cdot \mathbf{B} = 0 \ , \tag{5.6b}$$

$$\frac{\partial}{\partial \mathbf{r}} \times \mathbf{E} = -\frac{\partial \mathbf{B}}{\partial t} \ , \text{ and} \tag{5.6c}$$

$$\frac{\partial}{\partial \mathbf{r}} \times \mathbf{B} = \mu_0\,\mathbf{J} + \mu_0\,\epsilon_0\,\frac{\partial \mathbf{E}}{\partial t} \ , \tag{5.6d}$$

where $\mathbf{J}$ is current density. The ultimate goal of linear Vlasov analysis is to then use the resultant system of equations to derive the dispersion relation (i.e., the equation relating ω

and $\mathbf{k}$). Section 5.3 overviews the derivation of the dispersion relation for electromagnetic waves in uniform, magnetized plasma.

5.2.2 The Growth Rate of an Instability

For stability analysis, the key quantity is γ (i.e., the imaginary component of ω) because it indicates the initial time-evolution of the wave's amplitude. If $\gamma(\mathbf{k}) > 0$ for at least some values of $\mathbf{k}$, the plasma is considered unstable due to the exponential growth of the associated waves, which eventually causes particles to scatter and drives the plasma toward a more stable state.

Even for relatively mundane plasma conditions, the dispersion relation typically is a very complicated equation and may not even have a closed form. Nevertheless, numerical methods generally can be used to calculate the value of $\omega = \omega_r + i\,\gamma$ corresponding to any given $\mathbf{k}$-value. In this way, the function $\gamma(\mathbf{k})$ can be explored to determine whether or not the plasma is stable.

In practice, the function $\gamma(\mathbf{k})$ often has multiple local maxima, each of which may or may not be greater than zero. Rather than considering the global maximum value, it is generally more useful to associate each maximum with a different instability. Then, an instability's growth rate, $\gamma_{\max}$, is taken to be the growth rate, γ, of its fastest-growing mode, $\mathbf{k}_{\max}$; i.e.,

$$\gamma_{\max} = \gamma(\mathbf{k}_{\max}) = \max_{\mathbf{k}} \gamma(\mathbf{k}) \ , \tag{5.7}$$

where the maximization is taken over all wavevectors, $\mathbf{k}$, that are associated with the instability. Likewise, the instability's real frequency is

$$\omega_{\max} = \omega_r(\mathbf{k}_{\max}) \ . \tag{5.8}$$

When plasma is identified as being unstable to a given instability, it is meant that $\gamma_{\max} > 0$ for that instability.

5.3 Electromagnetic Dispersion Relation for Uniform, Magnetized Plasma

In this section, the Vlasov equation (see Equation 5.3) and Maxwell's equations (see Equation 5.6) are linearized and used to derive the dispersion relation for electromagnetic fluctuations in uniform plasma. For simplicity, this calculation is made in the frame of reference for which the unperturbed plasma has no net current; i.e., that for which

$$\sum_{\forall j} q_j \, n_j \, \mathbf{v}_j = 0 \ . \tag{5.9}$$

Throughout this section, it is assumed that the plasma contains no zeroth-order electric field and that the zeroth-order magnetic field is non-zero, uniform, and constant; i.e.,

$$\mathbf{E}^{(0)}(\mathbf{r}) = 0 \ , \qquad \text{and} \qquad \mathbf{B}^{(0)}(\mathbf{r}) = \mathbf{B}_0 \neq 0 \ , \tag{5.10}$$

where $\mathbf{B}_0$ is the background magnetic field. Without loss of generality, the coordinate system is chosen such that

$$\mathbf{B}_0 = B_0 \, \hat{\mathbf{z}} \ , \tag{5.11}$$

and

$$\mathbf{k} = k_y \, \hat{\mathbf{y}} + k_z \, \hat{\mathbf{z}} \ . \tag{5.12}$$

The propagation angle, θ, of the wave relative to the background magnetic field is defined to satisfy

$$\cos\theta = \frac{k_z}{k} = \frac{k_z}{\sqrt{k_y^2 + k_z^2}} \ , \tag{5.13}$$

where k (i.e., the magnitude of $\mathbf{k}$) denotes the wavenumber.

Initially, only minimal assumptions are made about the particle VDF's. However, in Section 5.3.3, each particle species is taken to have a bi-Maxwellian VDF and, in keeping with observations (see Figure 3.2), the differential flow between any two species is parallel to $\mathbf{B}_0$. This latter assumption, along with Equation 5.9, is equivalent to stating that, for each species j,

$$\mathbf{v}_j = v_{\|j}\,\hat{\mathbf{z}} \ . \tag{5.14}$$

5.3.1 Application of Maxwell's Equations

Based on Equations 5.4 and 5.10, the first-order expansions of $\mathbf{E}$ and $\mathbf{B}$ are

$$\mathbf{E}(t,\mathbf{r}) = \mathbf{E}^{(1)}(t,\mathbf{r}) \ , \qquad \text{and} \qquad \mathbf{B}(t,\mathbf{r}) = \mathbf{B}_0 + \mathbf{B}^{(1)}(t,\mathbf{r}) \ , \tag{5.15}$$

where

$$\begin{aligned} \mathbf{E}^{(1)}(t,\mathbf{r}) &= \mathbf{E}^{(1)}(\omega,\mathbf{k})\exp[i\,(\mathbf{k}\cdot\mathbf{r}-\omega\,t)] \ , \text{ and} \\ \mathbf{B}^{(1)}(t,\mathbf{r}) &= \mathbf{B}^{(1)}(\omega,\mathbf{k})\exp[i\,(\mathbf{k}\cdot\mathbf{r}-\omega\,t)] \ . \end{aligned} \tag{5.16}$$

Per Equation 5.9, the frame of reference is chosen such that the unperturbed plasma has no net current. Thus, the first-order expansion of the current density is

$$\mathbf{J}(t,\mathbf{r}) = \mathbf{J}^{(1)}(t,\mathbf{r}) = \mathbf{J}^{(1)}(\omega,\mathbf{k})\exp[i\,(\mathbf{k}\cdot\mathbf{r}-\omega\,t)] \ . \tag{5.17}$$

Substituting these expressions into Faraday's law and Ampère's law (i.e., Equations 5.6c and 5.6d, respectively) gives

$$\mu_0\,\mathbf{J}^{(1)}(\mathbf{k},\omega) = \frac{i}{\omega}\,\mathbf{k}\times\left[\mathbf{k}\times\mathbf{E}^{(1)}(\mathbf{k},\omega)\right] + \mu_0\,\epsilon_0\,i\,\omega\,\mathbf{E}^{(1)}(\mathbf{k},\omega) \ . \tag{5.18}$$

The particle flux density of species j is

$$\mathbf{\Gamma}_j(t,\mathbf{r}) = \int_{\forall\mathbf{u}} d^3u\,\mathbf{u}\,f_j(t,\mathbf{r},\mathbf{u}) = \int_{-\infty}^{\infty} du_z \int_{-\infty}^{\infty} du_y \int_{-\infty}^{\infty} du_x\,\mathbf{u}\,f_j(t,\mathbf{r},\mathbf{u}) \ , \tag{5.19}$$

where f_j is the species' VDF. Therefore, based on Equation 5.4,

$$\mathbf{J}^{(1)}(\mathbf{k},\omega) = \sum_{\forall j} q_j \, \mathbf{\Gamma}_j^{(1)}(\mathbf{k},\omega) \ , \tag{5.20}$$

where

$$\mathbf{\Gamma}_j^{(1)}(\mathbf{k},\omega) = \int_{-\infty}^{\infty} du_z \int_{-\infty}^{\infty} du_y \int_{-\infty}^{\infty} du_x \, \mathbf{u} \, f_j^{(1)}(\mathbf{k},\omega,\mathbf{u}) \ , \tag{5.21}$$

is the coefficient of the first-order term in the linear expansion of Γ_j.

This species' dimensionless conductivity tensor, S_j, is defined to satisfy the following relationship:

$$\mathbf{\Gamma}_j^{(1)}(\mathbf{k},\omega) = -\frac{i \, \epsilon_0 \, k^2 \, c^2}{q_j \, \omega} \, \mathsf{S}_j(\mathbf{k},\omega) \cdot \mathbf{E}^{(1)}(\mathbf{k},\omega) \ . \tag{5.22}$$

Combining Equations 5.18, 5.20, and 5.22 gives

$$\mathsf{D}(\mathbf{k},\omega) \cdot \mathbf{E}^{(1)}(\mathbf{k},\omega) = 0 \ , \tag{5.23}$$

where

$$\mathsf{D}(\mathbf{k},\omega) = \left(\omega^2 - c^2 \, k^2\right) \mathbf{1} + c^2 \, \mathbf{k}\,\mathbf{k} + c^2 \, k^2 \sum_{\forall j} \mathsf{S}_j(\mathbf{k},\omega) \ , \tag{5.24}$$

is the plasma's dispersion tensor. In this expression, $\mathbf{k}\,\mathbf{k}$ denotes the dyadic product of $\mathbf{k}$ with itself (see Appendix A) and

$$\mathbf{1} = \begin{pmatrix} 1 & 0 & 0 \\ 0 & 1 & 0 \\ 0 & 0 & 1 \end{pmatrix} \ , \tag{5.25}$$

indicates the unit tensor (i.e., the 3×3 identity matrix). The dispersion tensor can be

written more explicitly by expressing its elements individually:

$$
\begin{aligned}
D_{xx}(\mathbf{k},\omega) &= \omega^2 - c^2\,k^2 + c^2\,k^2 \sum_{\forall j} S_{xxj}(\mathbf{k},\omega)\ , \\
D_{xy}(\mathbf{k},\omega) &= c^2\,k^2 \sum_{\forall j} S_{xyj}(\mathbf{k},\omega)\ , \\
D_{xz}(\mathbf{k},\omega) &= c^2\,k^2 \sum_{\forall j} S_{xzj}(\mathbf{k},\omega)\ , \\
D_{yx}(\mathbf{k},\omega) &= c^2\,k^2 \sum_{\forall j} S_{yxj}(\mathbf{k},\omega)\ , \\
D_{yy}(\mathbf{k},\omega) &= \omega^2 - c^2\,k_z^2 + c^2\,k^2 \sum_{\forall j} S_{yyj}(\mathbf{k},\omega)\ , \\
D_{yz}(\mathbf{k},\omega) &= c^2\,k_y\,k_z + c^2\,k^2 \sum_{\forall j} S_{yzj}(\mathbf{k},\omega)\ , \\
D_{zx}(\mathbf{k},\omega) &= c^2\,k^2 \sum_{\forall j} S_{zxj}(\mathbf{k},\omega)\ , \\
D_{zy}(\mathbf{k},\omega) &= c^2\,k_y\,k_z + c^2\,k^2 \sum_{\forall j} S_{zyj}(\mathbf{k},\omega)\ , \text{ and} \\
D_{zz}(\mathbf{k},\omega) &= \omega^2 - c^2\,k_y^2 + c^2\,k^2 \sum_{\forall j} S_{zzj}(\mathbf{k},\omega)\ .
\end{aligned}
\tag{5.26}
$$

Because $\mathbf{E}^{(1)}(\omega,\mathbf{k})$ partially specifies the amplitude of the first-order perturbation, it can never be allowed to vanish to zero: otherwise, the plasma would have no perturbation at all. The combination of this fact and Equation 5.23 gives the dispersion relation for electromagnetic fluctuations in homogeneous plasma:

$$\det\left[\mathbf{D}(\mathbf{k},\omega)\right] = 0\ . \tag{5.27}$$

Since, in general, $\mathbf{D}$ is complex-valued, the determinants of its real and imaginary components must separately equal zero; i.e.,

$$\det(\Re[\mathbf{D}(\mathbf{k},\omega)]) = 0\ , \qquad \text{and} \qquad \det(\Im[\mathbf{D}(\mathbf{k},\omega)]) = 0\ . \tag{5.28}$$

The remainder of this section focuses on the derivation of an expression for $\mathbf{S}$, which enables this dispersion relation actually to be used.

5.3.2 Application of the Vlasov Equation

In order for the plasma to be in a state of equilibrium (stable or otherwise), the Vlasov equation should be satisfied for the zeroth-order (i.e., background) VDF's and fields. Expanding Equation 5.3 to the zeroth order gives

$$\frac{q_j}{m_j}\left(\mathbf{u}\times\mathbf{B}_0\right)\cdot\frac{\partial f_j^{(0)}}{\partial\mathbf{u}}=0\ . \tag{5.29}$$

For the remainder of this section, it is assumed that the criterion specified by Equation 5.29 is met by the zeroth-order VDF of each species j. This is indeed true for bi-Maxwellian VDF's with relative drift parallel to the background magnetic field (see Section 5.3.3) as well as for various other classes of functions.

Now, expanding Equation 5.3 to first order and applying Equation 5.29 gives

$$\frac{\partial f_j^{(1)}}{\partial t}+\mathbf{u}\cdot\frac{\partial f_j^{(1)}}{\partial\mathbf{r}}+\frac{q_j}{m_j}\left(\mathbf{u}\times\mathbf{B}_0\right)\cdot\frac{\partial f_j^{(1)}}{\partial\mathbf{u}}=-\frac{q_j}{m_j}\left(\mathbf{E}^{(1)}+\mathbf{u}\times\mathbf{B}^{(1)}\right)\cdot\frac{\partial f_j^{(0)}}{\partial\mathbf{u}}\ . \tag{5.30}$$

The right-hand side of this equation is the total time derivative of $f_j^{(1)}$. Therefore,

$$\begin{aligned} f_j^{(1)}(t,\mathbf{r},\mathbf{u})=-\frac{q_j}{m_j}\int_{-\infty}^{t}dt' \\ \left(\mathbf{E}^{(1)}[t',\mathbf{r}(t')]+\mathbf{u}(t')\times\mathbf{B}^{(1)}[t',\mathbf{r}(t')]\right)\cdot\frac{\partial f_j^{(0)}[\mathbf{u}(t')]}{\partial\mathbf{u}(t')}\ . \end{aligned} \tag{5.31}$$

In the above equation, $\mathbf{r}$ and $\mathbf{u}$ denote the specific phase-space location of a given particle at the specific time t. However, $\mathbf{r}(t')$ and $\mathbf{u}(t')$ are functions indicating the position and velocity of the particle for all times $t'\leq t$ and are of course subject to the boundary conditions

$$\mathbf{r}(t'=t)=\mathbf{r}\ ,\qquad\text{and}\qquad\mathbf{u}(t'=t)=\mathbf{u}\ . \tag{5.32}$$

The importance of this distinction is exemplified by the following:

$$\frac{d\mathbf{r}(t')}{dt'} = \mathbf{u}(t') \ , \qquad \text{but} \qquad \frac{d\mathbf{r}}{dt'} = 0 \ . \tag{5.33}$$

Essentially, then, the right-hand side of Equation 5.31 calculates the particle's perturbed location in phase space by integrating over all forces that ever acted on it.

Substituting the first-order expansions of $\mathbf{E}$ and $\mathbf{B}$ (i.e., Equations 5.15 and 5.16) into Faraday's law (i.e., Equation 5.6c) gives

$$\mathbf{B}^{(1)}(t, \mathbf{r}) = \frac{1}{\omega} \mathbf{k} \times \mathbf{E}^{(1)}(t, \mathbf{k}) \ . \tag{5.34}$$

Using this expression, Equation 5.31 can be rewritten as

$$\begin{aligned} f_j^{(1)}(t, \mathbf{r}, \mathbf{u}, \mathbf{k}, \omega) = -\frac{q_j}{m_j} \int_{-\infty}^{t} dt' \exp(i\, b_j[t', \mathbf{r}(t'), \mathbf{k}, \omega]) \\ \left[\frac{\partial f_j^{(0)}[\mathbf{u}(t')]}{\partial \mathbf{u}(t')} + \frac{1}{\omega} \mathbf{k} \times \left(\mathbf{u}(t') \times \frac{\partial f_j^{(0)}[\mathbf{u}(t')]}{\partial \mathbf{u}(t')} \right) \right] \\ \cdot \mathbf{E}^{(1)}(\mathbf{k}, \omega) \ , \end{aligned} \tag{5.35}$$

where

$$b_j[t', \mathbf{r}(t'), \mathbf{k}, \omega] = \mathbf{k} \cdot [\mathbf{r}(t') - \mathbf{r}(t)] - \omega\,(t' - t) \ . \tag{5.36}$$

Of course, the difficulty with evaluating the integral in Equation 5.35 is that doing so requires expressions for $\mathbf{r}(t')$ and $\mathbf{u}(t')$ for all values of $t' < t$. In less formal terms, this integration requires knowing the entire history of the particle's path through phase space, of which an exact calculation is impractical. However, the particle's trajectory can be approximated by assuming that, for $t' < t$, only the zeroth-order forces acted on it. Since the only such force results from the background magnetic field, $\mathbf{B}_0$, the particle's motion

was helical. In particular, its velocity (for $t' < t$) was

$$\begin{aligned} u_x(t') &= u_\perp \cos[\Omega_j\,(t'-t) - \phi] \ , \\ u_y(t') &= -u_\perp \sin[\Omega_j\,(t'-t) - \phi] \ , \text{ and} \\ u_z(t') &= u_z \ , \end{aligned} \tag{5.37}$$

where Ω_j is the particle's cyclotron frequency (see Equation 1.8),

$$u_\perp = \sqrt{u_x^2 + u_y^2} \ , \tag{5.38}$$

and

$$\phi = \arctan\left(\frac{u_y}{u_x}\right) \ . \tag{5.39}$$

As with all helical motion, the perpendicular and parallel components of the particle's velocity (i.e., $u_\perp$ and $u_\parallel = u_z$, respectively) are constants (i.e., independent of t'). Integration of Equation 5.37 with respect to t' reveals the particle's position (for $t' < t$) to have been

$$\begin{aligned} r_x(t') &= r_x + \frac{u_\perp}{\Omega_j}\left(\sin[\Omega_j\,(t'-t) - \phi] + \sin\phi\right) \ , \\ r_y(t') &= r_y + \frac{u_\perp}{\Omega_j}\left(\cos[\Omega_j\,(t'-t) - \phi] + \cos\phi\right) \ , \text{ and} \\ r_z(t') &= r_z + u_z\,(t'-t) \ . \end{aligned} \tag{5.40}$$

Applying Equations 5.12, 5.37, and 5.40 to Equations 5.35 and 5.36 gives

$$\begin{aligned} f_j^{(1)}(\mathbf{k},\omega,\mathbf{u}) = -\frac{q_j}{m_j}\int_{-\infty}^{0} d\tau \exp[i\,b_j(\tau,\mathbf{k},\omega,\mathbf{u})] \\ \left[\frac{\partial f_j^{(0)}[\mathbf{u}(\tau)]}{\partial \mathbf{u}(\tau)} + \frac{1}{\omega}\,\mathbf{k}\times\left(\mathbf{u}(\tau)\times\frac{\partial f_j^{(0)}[\mathbf{u}(\tau)]}{\partial \mathbf{u}(\tau)}\right)\right]\cdot\mathbf{E}^{(1)}(\mathbf{k},\omega) \ , \end{aligned} \tag{5.41}$$

and

$$b_j(\tau,\mathbf{k},\omega,\mathbf{u}) = \frac{k_y\,u_\perp}{\Omega_j}\left[\cos(\Omega_j\,\tau - \phi) - \cos\phi\right] + (k_z\,u_z - \omega)\,\tau \ , \tag{5.42}$$

where the variable of integration has been offset from t' to

$$\tau = t' - t \ . \tag{5.43}$$

5.3.3 Assumption of Bi-Maxwellian VDF's and Parallel Bulk Flow

Now, it is explicitly assumed that the zeroth-order VDF of each species is a bi-Maxwellian with a bulk velocity that is parallel to the background magnetic field; i.e.,

$$f_j^{(b0)}(\mathbf{u}) = \frac{n_j}{(2\pi)^{3/2}\, w_\perp^2\, w_\parallel} \exp\left[-\frac{u_x^2}{2\, w_{\perp j}^2} - \frac{u_y^2}{2\, w_{\perp j}^2} - \frac{\left(u_z - v_{\parallel j}\right)^2}{2\, w_{\parallel j}^2}\right] \ . \tag{5.44}$$

Though the left-hand side of this equation indicates that $f_j^{(b0)}$ is a function of $\mathbf{u}$, it's gyrotropy means that it is actually only dependent on $u_\perp$ and $u_\parallel = u_z$. Therefore, Equation 5.44 can equivalently be written as

$$f_j^{(b0)}(u_\perp, u_z) = \frac{n_j}{(2\pi)^{3/2}\, w_\perp^2\, w_\parallel} \exp\left[-\frac{u_\perp^2}{2\, w_{\perp j}^2} - \frac{\left(u_z - v_{\parallel j}\right)^2}{2\, w_{\parallel j}^2}\right] \ . \tag{5.45}$$

Nevertheless, the $\mathbf{u}$-gradient of $f_j^{(b0)}$ in dependent on other components of $\mathbf{u}$:

$$\frac{\partial f^{(b0)}}{\partial \mathbf{u}} = \frac{1}{w_{\perp j}^2}\left[-R_j\, \mathbf{u} + (R_j - 1)\, \mathbf{u}_\perp + R_j\, v_{\parallel j}\, \hat{\mathbf{z}}\right] f_j^{(b0)}(u_\perp, u_z) \ , \tag{5.46}$$

where R_j is the temperature anisotropy of species j (see Equation 1.4).

Substituting Equations 5.45 and 5.46 into Equation 5.41 gives

$$\begin{aligned} f_j^{(b1)}(\mathbf{k}, \omega, \mathbf{u}) = \Bigg(& \frac{q_j}{m_j\, w_{\perp j}^2}\, f_j^{(b0)}(u_\perp, u_z) \int_{-\infty}^{0} d\tau \exp[i\, b_j(\tau, \mathbf{k}, \omega, \mathbf{u})] \\ & \Bigg[R_j\, \mathbf{u}(\tau) - (R_j - 1)\left(1 - \frac{k_z\, u_z}{\omega}\right) \mathbf{u}_\perp(\tau) \\ & - (R_j - 1)\left(\frac{k_y\, u_z}{\omega}\right) u_y(\tau)\, \hat{\mathbf{z}} - v_{\parallel j}\, \frac{R_j\, k_z}{\omega}\, \mathbf{u}_\perp(\tau) \\ & + v_{\parallel j}\, R_j \left(1 + \frac{k_y\, u_y(\tau)}{\omega}\right) \hat{\mathbf{z}}\Bigg]\Bigg) \cdot \mathbf{E}^{(1)}(\mathbf{k}, \omega) \ . \end{aligned} \tag{5.47}$$

Then, by substitution of Equation 5.47 into Equation 5.21,

$$\begin{aligned}\mathbf{\Gamma}_j^{(b1)}(\mathbf{k},\omega) = \Bigg(& \frac{q_j}{m_j\, w_{\perp j}^2} \int_{-\infty}^{\infty} du_z \int_0^{\infty} du_\perp\, u_\perp \int_0^{2\,\pi} d\phi \\ & \mathbf{u}\, f_j^{(b0)}(u_\perp, u_z) \int_{-\infty}^{0} d\tau \exp[i\, b_j(\tau, \mathbf{k}, \omega, \mathbf{u})] \\ & \Bigg[R_j\, \mathbf{u}(\tau) - (R_j - 1) \left(1 - \frac{k_z\, u_z}{\omega}\right) \mathbf{u}_\perp(\tau) \\ & - (R_j - 1) \left(\frac{k_y\, u_z}{\omega}\right) u_y(\tau)\, \hat{\mathbf{z}} - v_{\parallel j}\, \frac{R_j\, k_z}{\omega}\, \mathbf{u}_\perp(\tau) \\ & + v_{\parallel j}\, R_j \left(1 + \frac{k_y\, u_y(\tau)}{\omega}\right) \hat{\mathbf{z}} \Bigg] \Bigg) \cdot \mathbf{E}^{(1)}(\mathbf{k},\omega)\ , \end{aligned} \tag{5.48}$$

where

$$\begin{aligned} u_x(\tau) &= u_\perp \cos(\Omega_j\, \tau - \phi)\ , \\ u_y(\tau) &= -u_\perp \sin(\Omega_j\, \tau - \phi)\ , \\ \mathbf{u}_\perp(\tau) &= u_x(\tau)\, \hat{\mathbf{x}} + u_y(\tau)\, \hat{\mathbf{y}}\ , \text{ and} \\ \mathbf{u}(\tau) &= \mathbf{u}_\perp(\tau) + u_z\, \hat{\mathbf{z}}\ . \end{aligned} \tag{5.49}$$

In Equation 5.48, the integration over $\mathbf{u}$ has been shifted to cylindrical coordinates to take advantage of the cylindrical symmetry of much of the integrand.

Finally, Equation 5.48 can be used with Equation 5.22 to give an expression for the dimensionless conductivity tensor:

$$\begin{aligned}\mathbf{S}_j^{(b)}(\mathbf{k},\omega) = & \frac{i\, q_j^2\, \omega}{\epsilon_0\, m_j\, w_{\perp j}^2\, k^2\, c^2} \int_{-\infty}^{\infty} du_z \int_0^{\infty} du_\perp\, u_\perp\, f_j^{(b0)}(u_\perp, u_z) \\ & \int_0^{2\,\pi} d\phi\, \mathbf{u} \int_{-\infty}^{0} d\tau \exp[i\, b_j(\tau, \mathbf{k}, \omega, \mathbf{u})] \\ & \Bigg[R_j\, \mathbf{u}(\tau) - (R_j - 1) \left(1 - \frac{k_z\, u_z}{\omega}\right) \mathbf{u}_\perp(\tau) \\ & - (R_j - 1) \left(\frac{k_y\, u_z}{\omega}\right) u_y(\tau)\, \hat{\mathbf{z}} - v_{\parallel j}\, \frac{R_j\, k_z}{\omega}\, \mathbf{u}_\perp(\tau) \\ & + v_{\parallel j}\, R_j \left(1 + \frac{k_y\, u_y(\tau)}{\omega}\right) \hat{\mathbf{z}} \Bigg]\ . \end{aligned} \tag{5.50}$$

Though not intractable, evaluating the expression for $\mathsf{S}_j^{(b)}$ in Equation 5.50 is non-trivial. In the most commonly-used approach, the integrand is expanded as an infinite series and the integration is carried out term-by-term. Details on this method are presented by Gary (1993) and by Baumjohann & Treumann (1997).

5.4 Ion Temperature Anisotropy Instabilities

The primary purpose of this study was to explore how instabilities driven by ion temperature anisotropy affect the solar wind. For the theoretical portion of this analysis, then, it was sufficient to consider, as in Section 5.3.3, a uniform, magnetized plasma in which each particle species has a bi-Maxwellian VDF. Consequently, the dispersion relation given in Equation 5.27, along with the dimensionless conductivity tensor specified in Equation 5.50, could be used to numerically compute $\gamma(\mathbf{k})$.

One consequence of these assumptions is that the fields and VDF's are all symmetric about the background magnetic field, $\mathbf{B}_0$, which means that $\gamma(\mathbf{k})$ is also symmetric about $\mathbf{B}_0$. In Section 5.3, this property allows the coordinate system to be chosen such that $k_x = 0$ without loss of generality. Thus, when computing $\gamma(\mathbf{k})$, it is sufficient to consider $\gamma(k, \theta)$, where $k = |\mathbf{k}|$ is the wavenumber and θ is the angle between $\mathbf{k}$ and $\mathbf{B}_0$ (see Equation 5.13). The k and θ values corresponding to a local maximum growth rate value, $\gamma_{\max}$, are denoted $k_{\max}$ and $\theta_{\max}$. More formally,

$$\gamma_{\max} = \gamma(k_{\max}, \theta_{\max}) = \max_{k,\theta} \gamma(t, \theta) \ , \qquad \text{and} \qquad \omega_{\max} = \omega_r(k_{\max}, \theta_{\max}) \ , \tag{5.51}$$

where the maximization is taken over all (k, θ)-values associated with the instability in question (cf. Equations 5.7 and 5.8).

	One-Dimensional $\theta_{\max} = 0°$ $\omega_{\max} > 0$	Two-Dimensional $0° < \theta_{\max} \leq 90°$ $\omega_{\max} = 0$
$R_j > 1$	Cyclotron	Mirror
$R_j < 1$	Parallel Firehose	Oblique Firehose

Table 5.1: Summary of ion temperature anisotropy instabilities. The cyclotron and parallel firehose instabilities are classified as *parallel* or *one-dimensional* since they always have $\theta_{\max} = 0°$. The mirror and oblique firehose instabilities are referred to as *oblique* or *two-dimensional* and always have $\omega_{\max} = 0$. For an ion species j, the cyclotron and mirror instabilities can be triggered by sufficiently-large $R_j > 1$, while the parallel and oblique firehose instabilities can develop for sufficiently small $R_j < 1$.

If only one ion species j is anisotropic, any associated instabilities are commonly referred to as being *driven by* that species. In this case, the function $\gamma(k, \theta)$ usually has at most two local maxima. One of these two maxima only occurs at $\theta = 0°$, and the corresponding instability is referred to as the *parallel firehose* instability if $R_j < 1$ or the *cyclotron* instability if $R_j > 1$. These instabilities can be thought of as being *one-dimensional* or *parallel* since one need only search along the k-axis to locate the associated $\gamma_{\max}$-value. The other maximum only occurs at $\theta \neq 0°$, and the corresponding instability is called the *oblique firehose* instability if $R_j < 1$ or the *mirror* instability if $R_j > 1$. Since locating the $\gamma_{\max}$-value corresponding to these two instabilities requires searching both in k and θ, they can be classified as *two-dimensional* or *oblique*. However, it can be shown that the oblique firehose and mirror instabilities always have $\omega_r = 0$, so (by symmetry) it is sufficient to only consider $\theta \in (0°, 90°]$.

These four types of anisotropy-driven instabilities are summarized in Table 5.1.

5.5 Calculating Instability Growth Rates

For this thesis project, Dr. S. Peter Gary of Los Alamos National Laboratory (LANL) supplied two of his `FORTRAN 77` programs for linear Vlasov calculations: `T3` and `EAN`. Each program models a plasma consisting of multiple species of charged particles, each of which is assumed to have a bi-Maxwellian VDF, and numerically solves the dispersion relation (see Equations 5.27 and 5.50) for the ω-value that corresponds to each user-provided $\mathbf{k}$-value.

In this study, these programs were used to model solar wind plasma, which was assumed to be electrically neutral and to consist of proton, α-particles, and electrons. Consequently, each calculation made with either code had nine free plasma parameters, which are listed in Table 5.2 along with their default values. All `T3` and `EAN` calculations reported in this dissertation were made using these default values unless stated otherwise.

Table 5.2 indicates that alternative values were not considered for three of the nine plasma parameters: R_e, $T_{\|e} \,/\, T_{\|p}$, and $c_A \,/\, c$. Since this study only considered ion-driven instabilities, the electrons, for simplicity, were always taken to be isotropic. Under this assumption of $R_e = 1.00$, both `T3` and `EAN` were found to be quite insensitive to the electron temperature, so $T_{\|e} \,/\, T_{\|p}$ was kept at its default value. Likewise, $c_A \,/\, c$ was never changed from its default value since all values $\ll 1.00$ gave practically identical output.

Despite their similar design and function, `T3` and `EAN` differ in two important ways that necessitated that both of these programs be used in this study. First, `T3` implicitly assumes that $\mathbf{k}$ and $\mathbf{B}_0$ are parallel; in contrast, `EAN` is able to consider non-zero θ-values. Consequently, `T3` is a one-dimensional code in that it calculates

$$\gamma(k) = \gamma(k, \theta = 0^\circ) \ , \tag{5.52}$$

Parameter	Default Value	Comment
$\beta_{\parallel p}$ or $\beta_{\parallel \alpha}$	—	A value need only be specified for one of these.
R_p	1.00	
R_α	1.00	
R_e	1.00	No alternative values were considered.
$T_{\parallel \alpha} \,/\, T_{\parallel p}$	4.00	
$T_{\parallel e} \,/\, T_{\parallel p}$	1.00	No alternative values were considered.
$n_\alpha \,/\, n_p$	0.05	
$c_A \,/\, c$	2.00×10^{-4}	No alternative values were considered.
$\Delta v_{\parallel \alpha p} \,/\, c_A$	0.00	`EAN` cannot consider alternative values.

Table 5.2: List of the nine physical parameters that can be adjusted in the `T3` and `EAN` codes. In reality, these programs have other parameters (e.g., n_e), but they are restricted by the assumptions (used throughout this study) that the plasma has no net charge and consists only of protons, α-particle, and electrons (see Section 5.5). There is no need to specify both $\beta_{\parallel p}$ and $\beta_{\parallel \alpha}$ since one can be calculated from the other using $T_{\parallel \alpha} \,/\, T_{\parallel p}$ and $n_\alpha \,/\, n_p$ (see Equation 1.9). The second column lists each parameter's default value. Unless stated otherwise, any calculation described in this dissertation was made using these values.

while EAN is two-dimensional in that it calculates $\gamma(k, \theta)$ in general. Thus, EAN was needed to calculate the growth rates of the two-dimensional (i.e., mirror and oblique firehose) instabilities, while T3 was used to calculate the growth rates of the one-dimensional (i.e., cyclotron and parallel firehose) instabilities. Second, the EAN code implicitly assumes that the α-proton differential flow, $\Delta\mathbf{v}_{\alpha p}$, is zero, but T3 has $\Delta v_{\parallel \alpha p}$ as a free parameter (though $\Delta v_{\perp \alpha p}$ is still fixed at zero). Essentially, while T3 has all of the nine free parameters listed in Table 5.2, EAN has only eight since it has $\Delta v_{\parallel \alpha p} \,/\, c_A$ effectively locked to its default value of 0.00. Consequently, this study could only explore the effects of differential-flow on the one-dimensional instabilities.

For this thesis project, T3 and EAN themselves were left largely unmodified and were used to generate the dispersion plots shown in Chapters 6 and 7. However, in order to compare theory and observation, this study primarily used these programs to evaluate (under various plasma conditions) the instability growth rate, $\gamma_{\max}$, for each point in a fine grid over the $(\beta_{\parallel j}, R_j)$-plane. Since this grid contained no many points, the wrapper program SRCH was written to automatically and repeatedly execute T3 and EAN. As detailed in Section 6.4, a certain degree of care was needed in constructing SRCH because, due to the complexity of the equations involved, both T3 and EAN are highly sensitive to the initial guesses passed to them. Additionally, SRCH had to be able to handle various numerical problems as well as the complications that arise from having multiple ions in the plasma (see Sections 6.2 and 7.4).

Chapter 6

Instability Constraints on Proton Temperature Anisotropy

This thesis project used the theoretical techniques introduced in Chapter 5 and the *Wind*/FC dataset described in Chapter 4 to study the effects of ion temperature anisotropy instabilities on solar wind plasma. This chapter focuses specifically on proton instabilities; α-particle instabilities are discussed in Chapter 7.

Section 6.1 introduces the dispersion plot as a tool for stability analysis and presents example plots for the four proton temperature anisotropy instabilities (see Table 5.1). Some of the complications that can arise from having multiple ion species in the plasma are explored in Section 6.2. The concept of an instability threshold is introduced in Section 6.3, and the method used in this thesis project to calculate them is described in Section 6.4. Section 6.5 presents thresholds for the proton instabilities under the default plasma conditions and compares these to the *Wind*/FC dataset. Alternative plasma conditions are explored in Section 6.6.

6.1 Dispersion Plots for Proton Temperature Anisotropy Instabilities

One of the most common ways to assess the theoretical stability of a given plasma configuration is a dispersion plot: i.e., a plot, based on the appropriate dispersion relation, of complex angular frequency, $\omega = \omega_r + i\,\gamma$, as a function of wavevector, $\mathbf{k}$ (see Chapter 5). From such a plot, it is possible to discern which (if any) $\mathbf{k}$-values are growing (i.e., have a growth rate, γ, that is positive).

The logistics of plotting ω versus $\mathbf{k}$ can be problematic if for no other reason than $\mathbf{k}$ is a three-dimensional vector. However, temperature anisotropy instabilities are usually studied by assuming that each particle species' VDF is a bi-Maxwellian (see Equation 1.5), which is radially symmetric about the background magnetic field, $\mathbf{B}_0$. As discussed in Section 5.4, this means that $\omega(\mathbf{k})$ shares this symmetry. Therefore, it is sufficient to plot $\omega_r(k,\theta)$ and $\gamma(k,\theta)$, where $k = |\mathbf{k}|$ is the wavenumber and θ is the angle between $\mathbf{k}$ and $\mathbf{B}_0$.

Table 5.1 reveals that this dispersion analysis can be further simplified. Two of the four instabilities listed therein, the cyclotron and parallel firehose instabilities, are *one-dimensional* in that their fastest-growing mode, $\mathbf{k}_{\max}$, always occurs parallel to $\mathbf{B}_0$. Thus, to calculate $\gamma_{\max}$ and $\omega_{\max}$ for these two instabilities, it is sufficient to plot

$$\omega_r(k) = \omega_r(k, \theta = 0^\circ) \qquad \text{and} \qquad \gamma(k) = \gamma(k, \theta = 0^\circ)\ . \tag{6.1}$$

The remaining two instabilities, the mirror and oblique firehose, are *two-dimensional* and have been shown to always have $\omega_{\max} = 0$. Therefore, for these two instabilities, only $\gamma(k,\theta)$ need be plotted.

Figures 6.1, 6.2, 6.3, and 6.4 respectively show examples of dispersion plots for the

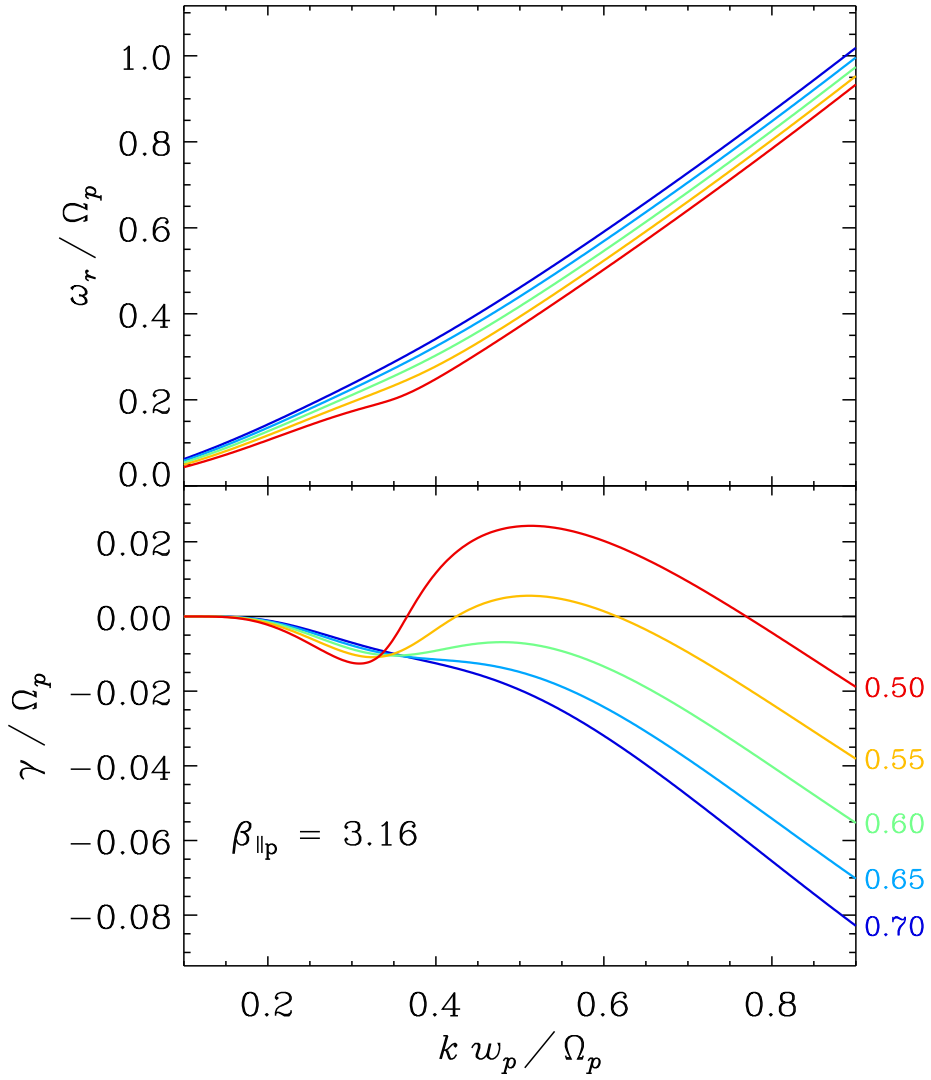

Figure 6.1.— Plots of ω_r (top) and γ (bottom) as functions of k for the proton-driven parallel firehose instability for $\beta_{\parallel p} = 3.16$. Each γ-curve is labeled with the R_p-value that was used in `T3` to generate it along with its corresponding ω_r-curve. As the value of $R_p < 1$ decreases, the value of $\gamma_{\rm max}$ increases, which indicates that the plasma is more unstable.

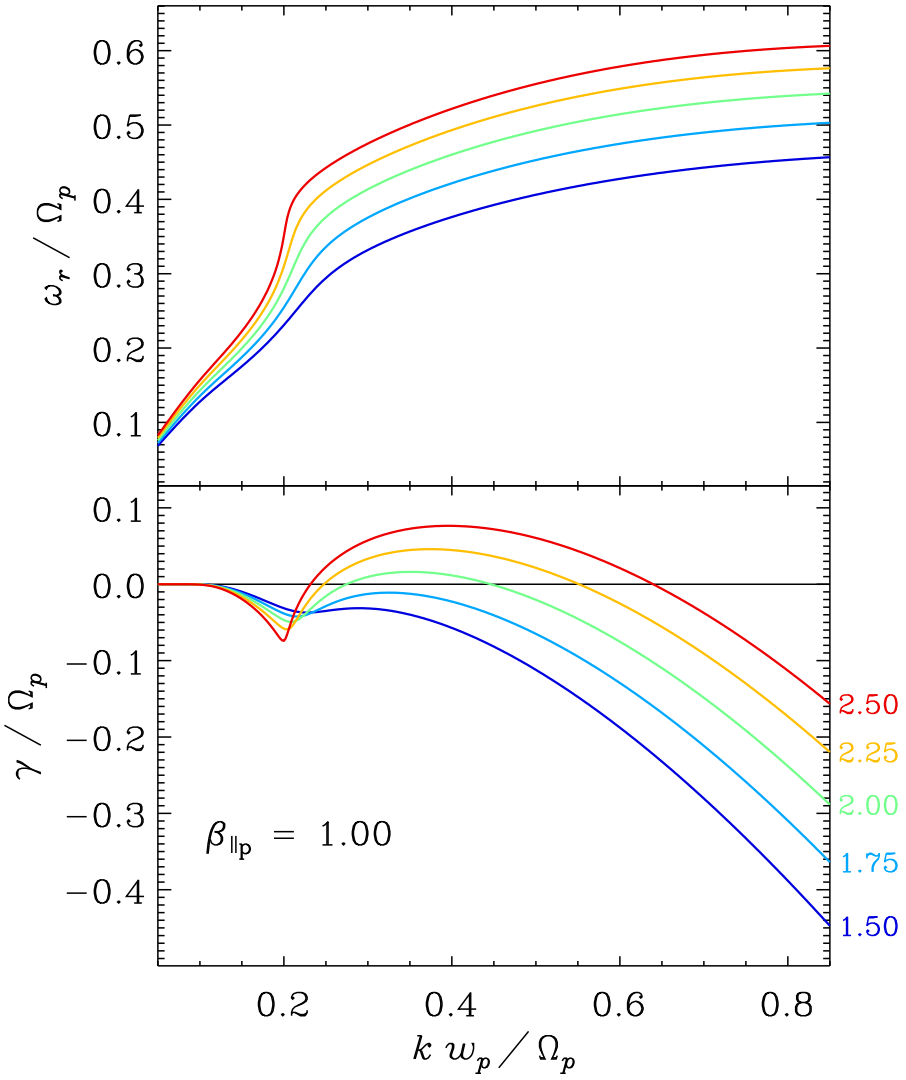

Figure 6.2.— Plots of ω_r (top) and γ (bottom) as functions of k for the proton-driven cyclotron instability for $\beta_{\|p} = 1.00$. Each γ-curve is labeled with the R_p-value that was used in `T3` to generate it along with its corresponding ω_r-curve. As the value of $R_p > 1$ increases, the value of $\gamma_{\max}$ also increases, which indicates that the plasma is more unstable.

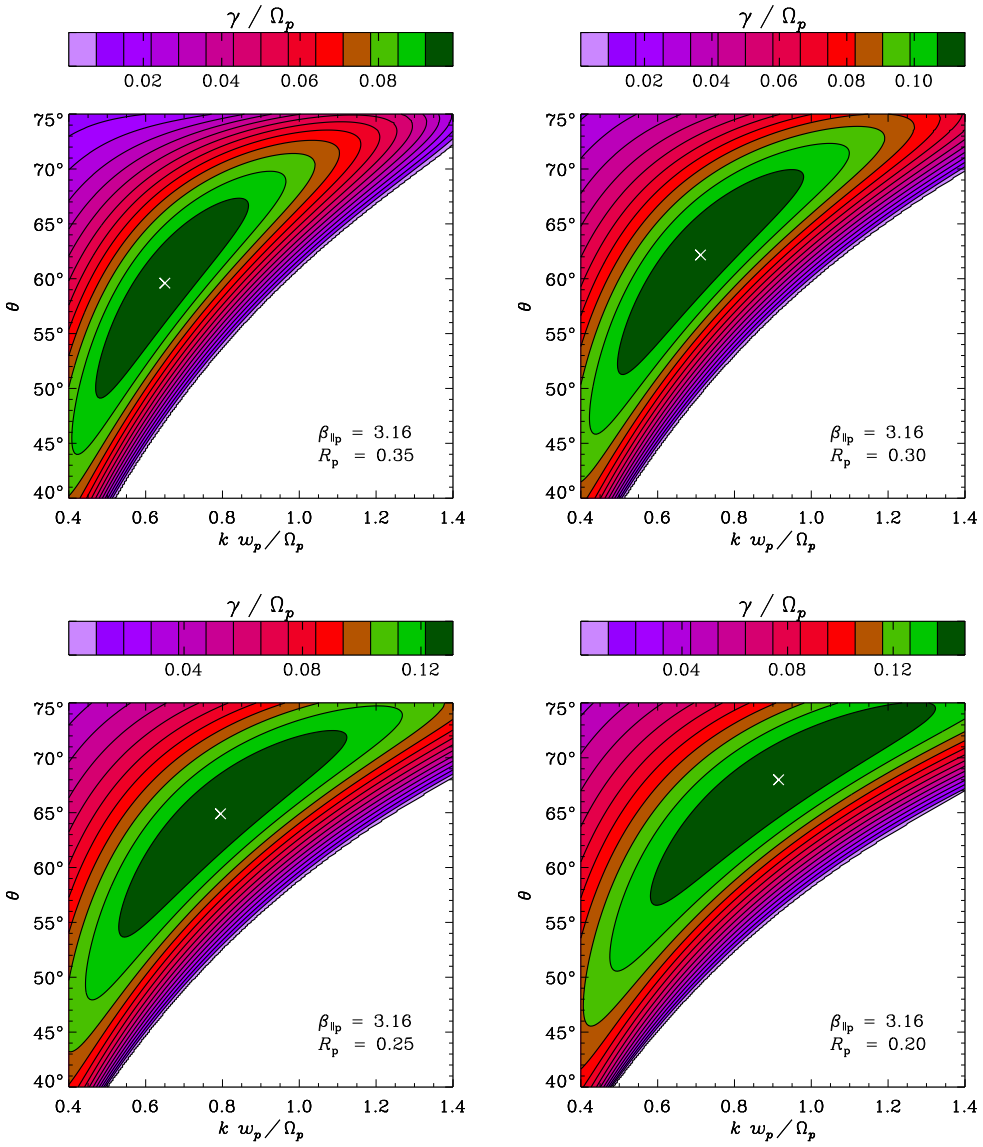

Figure 6.3.— Plots of γ as a function of k and θ for the proton-driven oblique firehose instability for $\beta_{\|p} = 3.16$. Values of $\gamma < 10^{-3}\,\Omega_p$ are not shown. Each plot was generated with `EAN` and assuming a different R_p-value: 0.35 (upper-left), 0.30 (upper-right), 0.25 (lower-left), and 0.20 (lower-right). As the value of $R_p < 1$ decreases, the values of $\gamma_{\rm max}$, $k_{\rm max}$, and $\theta_{\rm max}$ all increase.

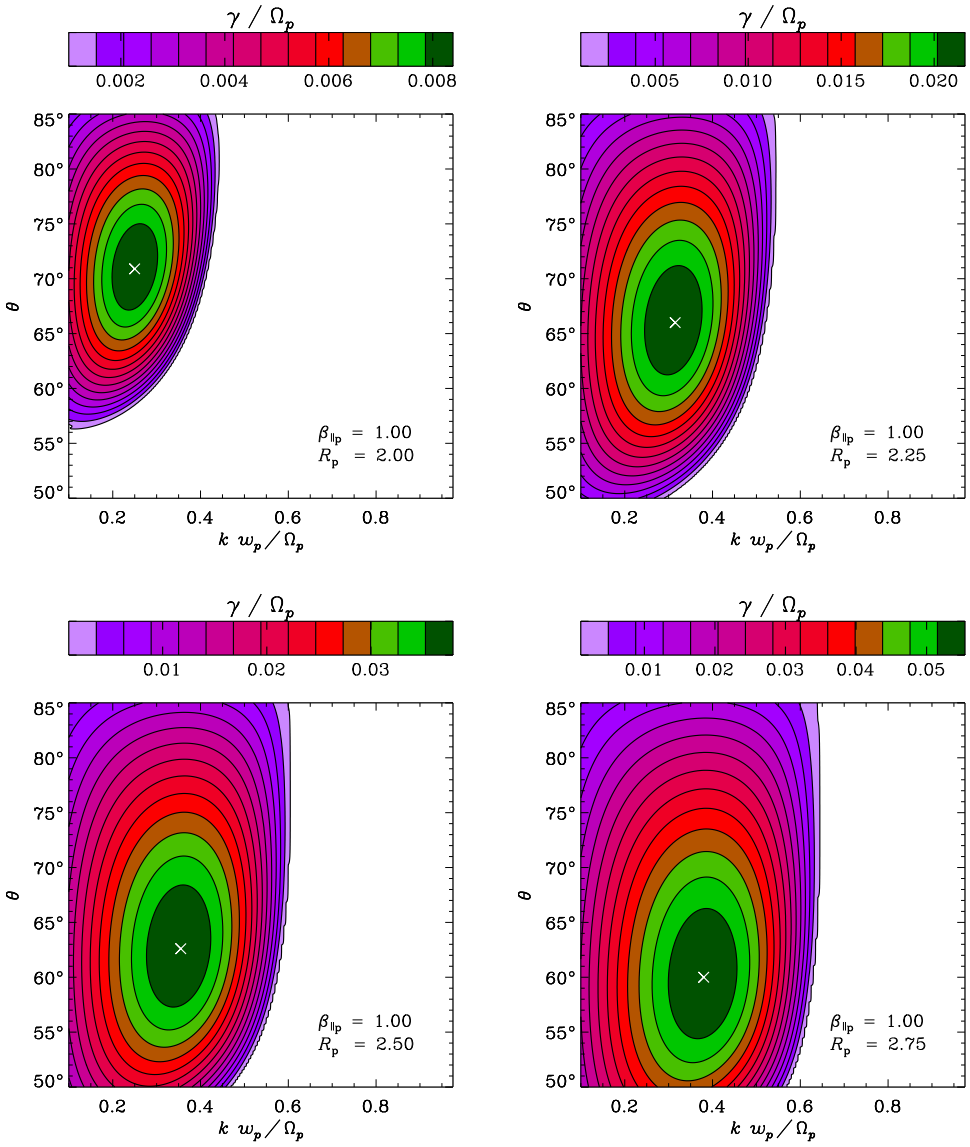

Figure 6.4.— Plots of γ as a function of k and θ for the proton-driven mirror instability for $\beta_{\|p} = 1.00$. Values of $\gamma < 10^{-3}\,\Omega_p$ are not shown. Each plot was generated with `EAN` and assuming a different R_p-value: 2.00 (upper-left), 2.25 (upper-right), 2.50 (lower-left), and 2.75 (lower-right). As the value of $R_p > 1$ increases, the values of $\gamma_{\max}$ and $k_{\max}$ increase, but the value of $\theta_{\max}$ decreases.

proton-driven parallel firehose, cyclotron, oblique firehose, and mirror instabilities. The first two plots were generated using output from `T3`, while the latter two show output from `EAN` (see Section 5.5). In all four plots (as well as in all similar plots in the remainder of this dissertation), γ and (where applicable) ω_r are normalized to the proton cyclotron frequency, Ω_p, (see Equation 1.8). Likewise, k is normalized to $\Omega_p \,/\, w_{\parallel p}$ (where $w_{\parallel p}$ is the proton parallel thermal speed), and θ (where applicable) is given in units of degrees.

The plots in Figure 6.1 of ω_r and γ as functions of k for the proton-driven parallel firehose instability were generated using a fixed value of $\beta_{\parallel p} = 3.16$ and five representative R_p-values: 0.75, 0.70, 0.65, 0.60, and 0.55. For relatively large values of $R_p < 1$, $\gamma(k)$ is negative for all k, so the plasma is stable (at least to parallel-propagating modes). However, as R_p decreases, $\gamma(k)$ becomes positive for some k values, which means that the plasma is unstable to those modes.

Figure 6.2 shows the corresponding plots for the proton-driven cyclotron instability. The value of $\beta_{\parallel p}$ was kept fixed at 1.00, but five different values of R_p were considered: 1.50, 1.75, 2.00, 2.25, and 2.50. For sufficiently low values of $R_p > 1$, the value of $\gamma(k)$ remains negative for all values of k, and the plasma is stable to the proton-driven cyclotron instability. However, as R_p increases, $\gamma(k)$ becomes positive for a finite domain of k-values, which indicates that the plasma is unstable to these modes. Additionally, as R_p grows, $k_{\max}$ grows along with $\gamma_{\max}$.

Figure 6.3 shows plots of γ as a function of k and θ for the proton-driven oblique firehose instability for $\beta_{\parallel p} = 3.16$. Each plot was generated for a different R_p-value: 0.35, 0.30, 0.25, and 0.20. As the value of $R_p < 1$ decreases, the value of $\gamma_{\max}$ increases, which indicates that the plasma is becoming more active. As $\gamma_{\max}$ increases, so do both $k_{\max}$ and $\theta_{\max}$.

Finally, Figure 6.4 shows plots of $\gamma(k, \theta)$ for the proton-driven mirror instability for $\beta_{\|p} = 1.00$, each of which was generated for a different R_p-value: 2.00, 2.25, 2.50, and 2.75. As the value of $R_p > 1$ increases, so does the value of $\gamma_{\max}$, which corresponds to the plasma becoming progressively more unstable. While $k_{\max}$ increases with $\gamma_{\max}$, $\theta_{\max}$ decreases.

Since the plots for the proton-driven cyclotron and mirror instabilities (Figures 6.2 and 6.4, respectively) were all generated with $\beta_{\|p} = 1.00$, they can be used to compare the relative action of these two instabilities in limiting $R_p > 1$ at that particular $\beta_{\|p}$-value. Even by visual inspection, for a given R_p-value (e.g., $R_p = 2.50$), $\gamma_{\max}$ for the cyclotron instability is greater than that for the mirror instability. This is consistent with past theoretical results which suggest that (under typical solar wind conditions) the proton-driven cyclotron instability has a higher growth rate than the proton-driven mirror instability for $\beta_{\|p} \lesssim 6.0$ (Gary et al., 1976). However, recently-published observational results by Hellinger et al. (2006) and Bale et al. (2009) as well as the results reported in this chapter suggest that the mirror instability is more active than the cyclotron instability in limiting $R_p > 1$ in the solar wind at 1 AU.

One consistent feature of all of these plots is that the peaks in γ are all quite broad. This means that an accurate value of $\gamma_{\max}$ can usually be established with relative ease. However, evaluating $k_{\max}$ and (where applicable) $\theta_{\max}$ is complicated by even relatively small rounding or floating-point errors made over the course of the calculation.

6.2 Effects of Stationary, Isotropic α-Particles

For default calculations of proton instabilities, $n_\alpha/n_p = 0.05$, $\Delta v_{\|\alpha p} = 0$, and $R_\alpha = 1$ (see Table 5.2). However, even this relatively-small, stationary, and isotropic population of α-

particles can significantly impact the growth rates of the proton instabilities. Under certain plasma conditions, these effects can even dramatically change the morphology of $\gamma(\mathbf{k})$.

For example, Figure 6.5 shows plots for the proton parallel firehose instability of $\omega_r(k)$ and $\gamma(k)$ for $\beta_{\parallel p} = 6.51$ and five different values of R_p: 0.715, 0.720, 0.725, 0.730, and 0.735. For all of these R_p-values, $\gamma_{\max} > 0$, and (as expected) the value of $\gamma_{\max}$ decreases as that of R_p increases. However, for the higher R_p-values, the $\gamma(k)$-curves have a distinct "notch." This feature has been found to be absent in similar plots for lower values of $n_\alpha \,/\, n_p$, so it has been interpreted as the isotropic α-particles stabilizing the plasma against the anisotropic protons. Surprisingly, this notch is so narrow and deep that it causes $\gamma(k)$ to develop two, distinct peaks and therefore two local maxima. This complicates the calculation of $\gamma_{\max}$ (especially using automated algorithms) since a second peak in $\gamma(k)$ can easily be missed. Furthermore, as this figure shows, the relative heights of the peaks can change: for $R_p = 0.730$, the high-k peak is higher, but, for $R_p = 0.735$, the low-k peak is higher. Figure 6.6, which is introduced in Section 6.5, reveals that this *double-peak* effect causes a discontinuity in the trends of $\gamma_{\max}$, $k_{\max}$, and $\omega_{\max}$ over the $(\beta_{\parallel p}, R_p)$-plane for the proton parallel firehose instability.

The occurrence of double peaks in γ is not limited to the proton parallel firehose instability. As can be seen in Figure 6.8, this effect has an even more dramatic impact on the proton oblique firehose instability. Each plot in this figure clearly shows a "hook" in the region around $(\beta_{\parallel p}, R_p) \approx (3.0, 0.6)$. This double-peak phenomenon also manifests itself, albeit more subtly, with the proton mirror instability in the region around $(\beta_{\parallel p}, R_p) \approx (10., 3.)$ (see Figure 6.9). However, because the double-peak phenomenon in the mirror instability is even more pronounced when α-particles are the driving species (i.e., when protons are isotropic and α-particles are anisotropic), a more complete discussion is reserved for Section 7.4.

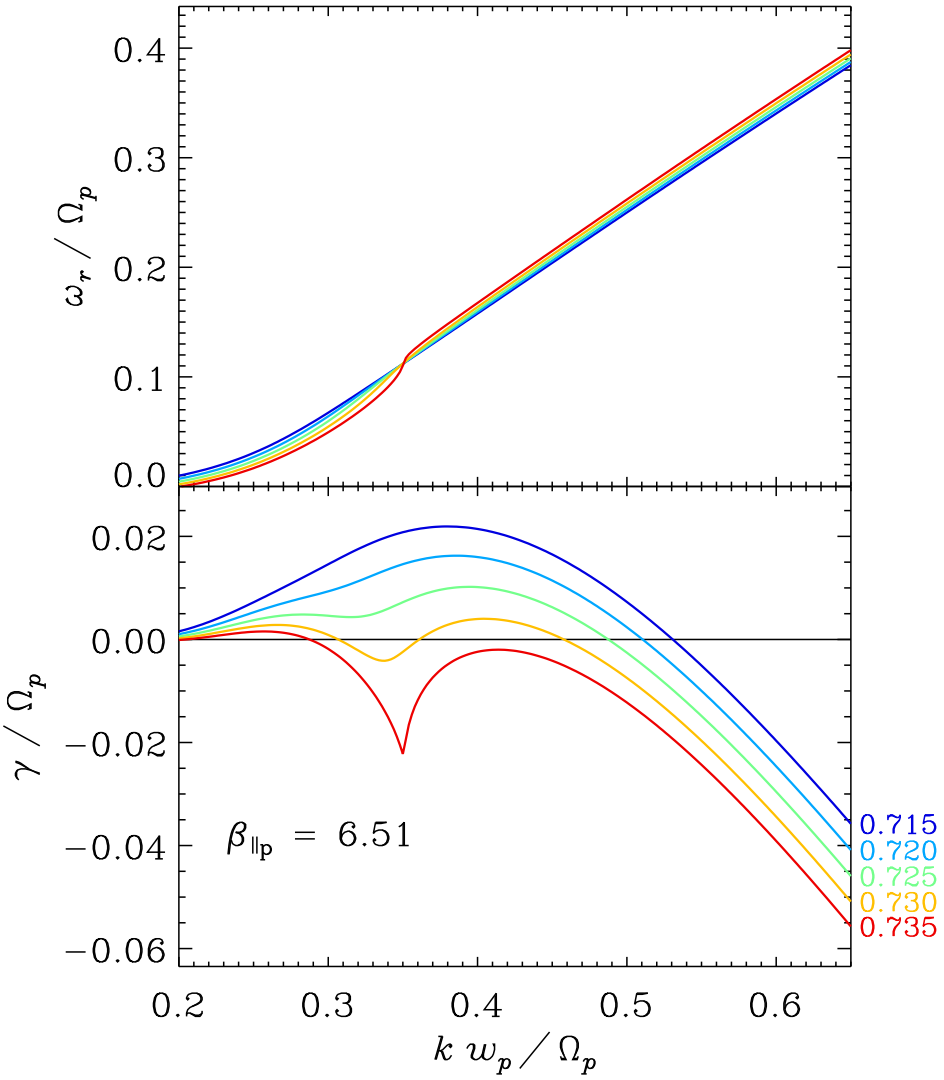

Figure 6.5.— Plots of ω_r (top) and γ (bottom) as functions of k for the proton-driven parallel firehose instability for $\beta_{\parallel p} = 6.51$. Each γ-curve is labeled with the R_p-value that was used in `T3` to generate it along with its corresponding ω_r-curve. At the larger values of R_p, $\gamma(k)$ has a distinct "notch," which results from the plasma's small population of isotropic α-particles (i.e., $n_\alpha \,/\, n_p = 0.05$ and $\zeta = 0.00$) and causes discontinuities in $k_{\max}(\beta_{\parallel p}, R_p)$ and $\omega_{\max}(\beta_{\parallel p}, R_p)$ (see Figure 6.6).

These occurrences of double peaks in $\gamma(k)$ and $\gamma(k, \theta)$ for proton instabilities should not be interpreted as the development of separate instabilities driven by the α-particles. For each of the plots mentioned in this section, the α-particles were assumed to be isotropic and stationary (relative to the protons), so they had no free energy associated with them to drive such an instability. Rather, it would be more accurate to classify the double-peak effect a perturbation of the proton instabilities caused by the presence of another ion species.

The various examples in this section (as well as those in Sections 7.2 and 7.4) suggest some limitations to using $\gamma_{\max}$ as a proxy for the overall activity of an instability. A potentially more accurate measure of an instability's growth rate might consist of an integral of $\gamma(\mathbf{k})$ (or some function thereof) over all $\mathbf{k}$ or over all $\mathbf{k}$ for which $\gamma(\mathbf{k}) > 0$. Developing the theoretical framework for such a metric is beyond the scope of this study. Additionally, such a definition would present numerous computation problems since it would necessitate accurate calculations of $\gamma(\mathbf{k})$ over a wide domain of $\mathbf{k}$-values rather than just the limited domain near $\mathbf{k}_{\max}$.

6.3 Introduction to Instability Thresholds

The function $\gamma(\mathbf{k})$ for an instability driven by the temperature anisotropy of an ion species j is dependent on all of the plasma's various bulk parameters (e.g., the density and temperature of each species) but is particularly sensitive to two dimensionless parameters: $\beta_{\parallel j}$ and R_j. Consequently, such an instability is commonly analyzed by calculating its $\gamma_{\max}$ as a function of $\beta_{\parallel j}$ and R_j. This partitions the $(\beta_{\parallel j}, R_j)$-plane into two regions: one unstable, where $\gamma_{\max}(\beta_{\parallel j}, R_j) > 0$, and the other stable. Formally, the instability threshold is the curve that separates these two regions and thereby defines the onset of the instability. However,

for $\gamma_{\max} > 0$, the value of $\gamma_{\max}^{-1}$ can be interpreted as roughly the amount of time that the instability takes to significantly effect the plasma. Thus, because the high variability of solar wind bulk parameters renders the use of the threshold criterion $\gamma_{\max} = 0$ to be impractical, this study instead used

$$\gamma_{\max} = 10^{-2}\,\Omega_p \ . \tag{6.2}$$

Intuitively, the threshold of an anisotropy-driven instability should be a monotonic curve in the $(\beta_{\parallel j}, R_j)$-plane and is customarily analyzed as a threshold temperature anisotropy, $\mathcal{R}_j$, that varies as a function of $\beta_{\parallel j}$. Because $R_j = 1$ is inherently stable for all anisotropy-driven instabilities, the instability threshold can never cross $R_j = 1$, but

$$\lim_{\beta_{\parallel j}\to\infty} \mathcal{R}_j(\beta_{\parallel j}) = 1 \ . \tag{6.3}$$

Various analytic approximations for $\mathcal{R}_j(\beta_{\parallel j})$ have been developed, but one that has recently gained popularity (and is used in through the remainder of this dissertation) is

$$\mathcal{R}_j(\beta_{\parallel j}) = 1 + \frac{a}{\left(\beta_{\parallel j} - \beta_0\right)^b} \ , \tag{6.4}$$

where a, b, and β_0 are fit parameters with values that are specific to the instability in question (Hellinger et al., 2006).

However, as described in Sections 6.2 and 7.4, the double-peak effect can result in irregularities (some physical but others merely computational) in the trends of $\gamma_{\max}(\beta_{\parallel j}, R_j)$ for some instabilities in certain regions of the $(\beta_{\parallel j}, R_j)$-plane. In the case of the proton and α-particle mirror instabilities, the double-peak effect only seems to appear at relatively high $\gamma_{\max}$-values: far away from from the threshold criterion specified by Equation 6.2. For each of the proton firehose instabilities, though, this effect manifests itself very near to the threshold (see Figures 6.6 and 6.8). Consequently, for these instabilities, the affected regions were suppressed in fits of Equation 6.4 to the $\gamma_{\max}$-contour specified by Equation 6.2.

6.4 Calculating $\gamma_{\max}$ Across the $(\beta_{\parallel j}, R_j)$-Plane

In order to actually calculate an instability threshold (i.e, derive best-fit values for the parameters a, b, and β_0 from Equation 6.4), $\gamma_{\max}$ must be calculated for various $(\beta_{\parallel j}, R_j)$-values while the values of all other plasma parameters remain fixed. To this end, the wrapper program `SRCH` was written for the `T3` and `EAN` programs. The `SRCH` code begins by prompting the user to select a primary driving species j (i.e., protons or α-particles) and an instability (i.e., parallel firehose or cyclotron for `T3` or oblique-firehose or mirror for `EAN`). Then, the program partitions a portion of the $(\beta_{\parallel j}, R_j)$-plane into a fine grid. A starting point in the grid and various settings for the linear analysis code are automatically generated by adapting a table of results from prior, successful runs. The `SRCH` program then proceeds to repeatedly call the appropriate linear analysis code (i.e., `T3` or `EAN`) on the various grid points. It begins with the starting point, and then continues on to other points by using the successful results (if any) of its neighbors as a guide for executing the linear analysis code on that point. For each point, `SRCH` attempts to identify values for $\gamma_{\max}$, $k_{\max}$, and either $\omega_{\max}$ (for `T3`) or $\theta_{\max}$ (for `EAN`). In doing so, the code verifies that these values correspond to a valid local maximum.

In addition to specifying j (i.e., the driving species) and the particular instability, the user is left to assign values to the `SRCH` code's four physical parameters, which are listed in Table 6.1 along with their default values. However, the last parameter in Table 6.1, $\Delta v_{\parallel \alpha p} \,/\, c_A$, is only applicable if `SRCH` is used to run the `T3` code since the `EAN` code implicitly assumes that $\Delta v_{\parallel \alpha p} = 0$.

Section 6.5 describes instability thresholds generated for the protons using the default values in Table 6.1 and compares these theoretical limits on R_p with the dataset described in

Parameter	Default Value	Alternative Values
$n_\alpha \,/\, n_p$	0.05	0.10, 0.20
$T_{\parallel\alpha} \,/\, T_{\parallel p}$	4.00	2.00, 8.00
ζ	0.00	0.05, 0.25, 0.50
$\Delta v_{\parallel\alpha p} \,/\, c_A$	0.00	-0.50, $+0.50$

Table 6.1: List of the four physical parameters that can be adjusted in the `SRCH` code. The second column lists each parameter's default value, and the third column lists the alternative values that were considered in this study. Note that the last parameter, $\Delta v_{\parallel\alpha p} \,/\, c_A$, is only relevant if `SRCH` is used to run the `T3` linear analysis code; the `EAN` code always implicitly assumes that the value of this parameter is zero.

Chapter 4. Section 6.6 explores how varying the four `SRCH` parameters affects the instability thresholds.

6.5 Default Instability Thresholds

This section describes the investigation of proton temperature anisotropy instabilities for the default parameter values listed in Table 6.1. The `SRCH` code was run for each of the four instabilities listed in Table 5.1, and the corresponding results are shown graphically in Figure 6.6 for the parallel firehose instability, Figure 6.7 for the cyclotron instability, Figure 6.8 for the oblique firehose instability, and Figure 6.9 for the mirror instability. All four figures contain plots of $\gamma_{\max}$ and $k_{\max}$ over the $(\beta_{\parallel p}, R_p)$-plane. Figures 6.6 and 6.7 also contain plots of $\omega_{\max}$ but no plots of $\theta_{\max}$; since the parallel firehose and cyclotron instabilities are one-dimensional, $\theta_{\max} = 0^\circ$ by definition. Conversely, Figures 6.8 and 6.9 include plots of $\theta_{\max}$ but not $\omega_{\max}$ since $\omega_{\max} = 0$ for these two-dimensional instabilities.

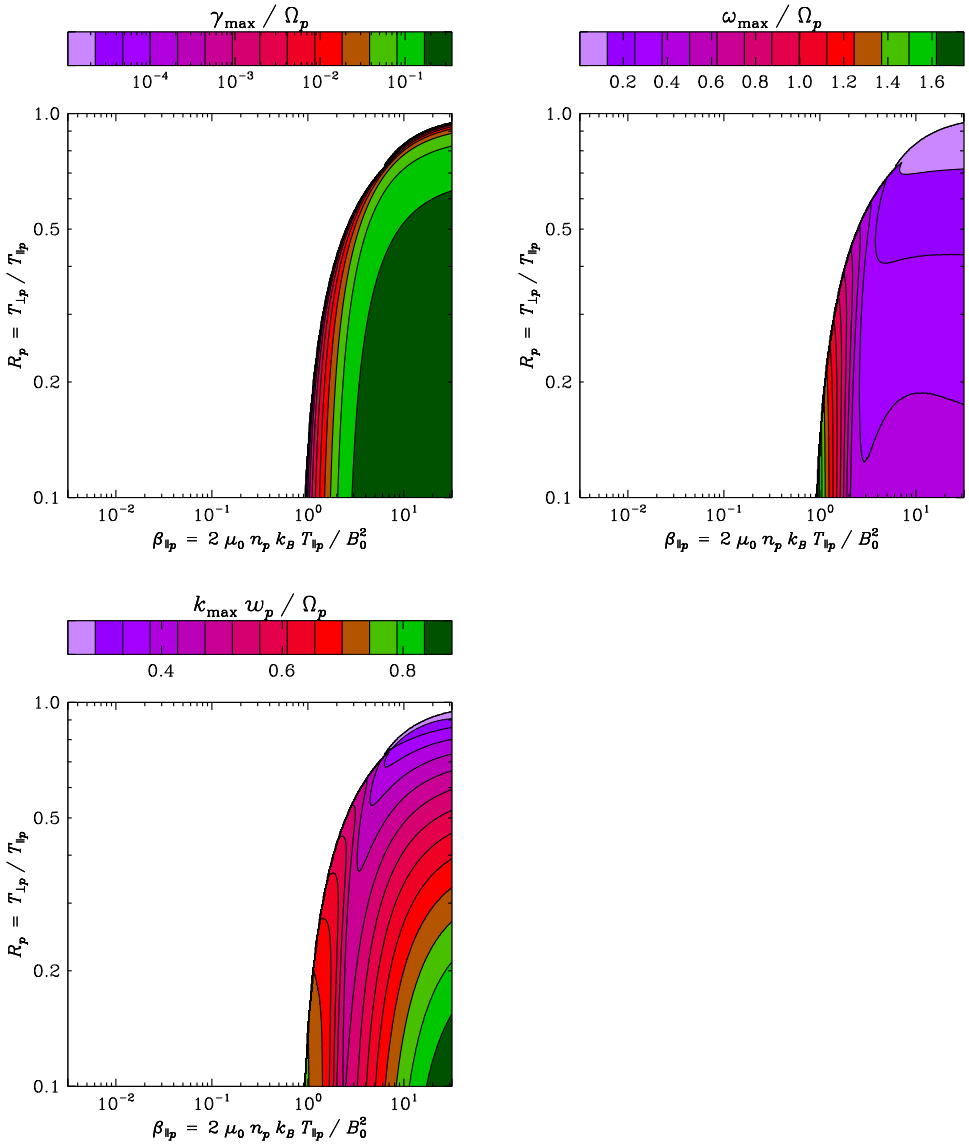

Figure 6.6.— Plots of $\gamma_{\max}$ (upper-left), $\omega_{\max}$ (upper-right), and $k_{\max}$ (lower-left) as functions of $\beta_{\parallel p}$ and R_p for the proton-driven parallel firehose instability. These plots were generated by using the default value for each of the four `SRCH` parameters (see Table 6.1). No plot of $\theta_{\max}$ was necessary since, being one-dimensional, the parallel firehose instability always has $\theta_{\max} = 0^\circ$ by definition.

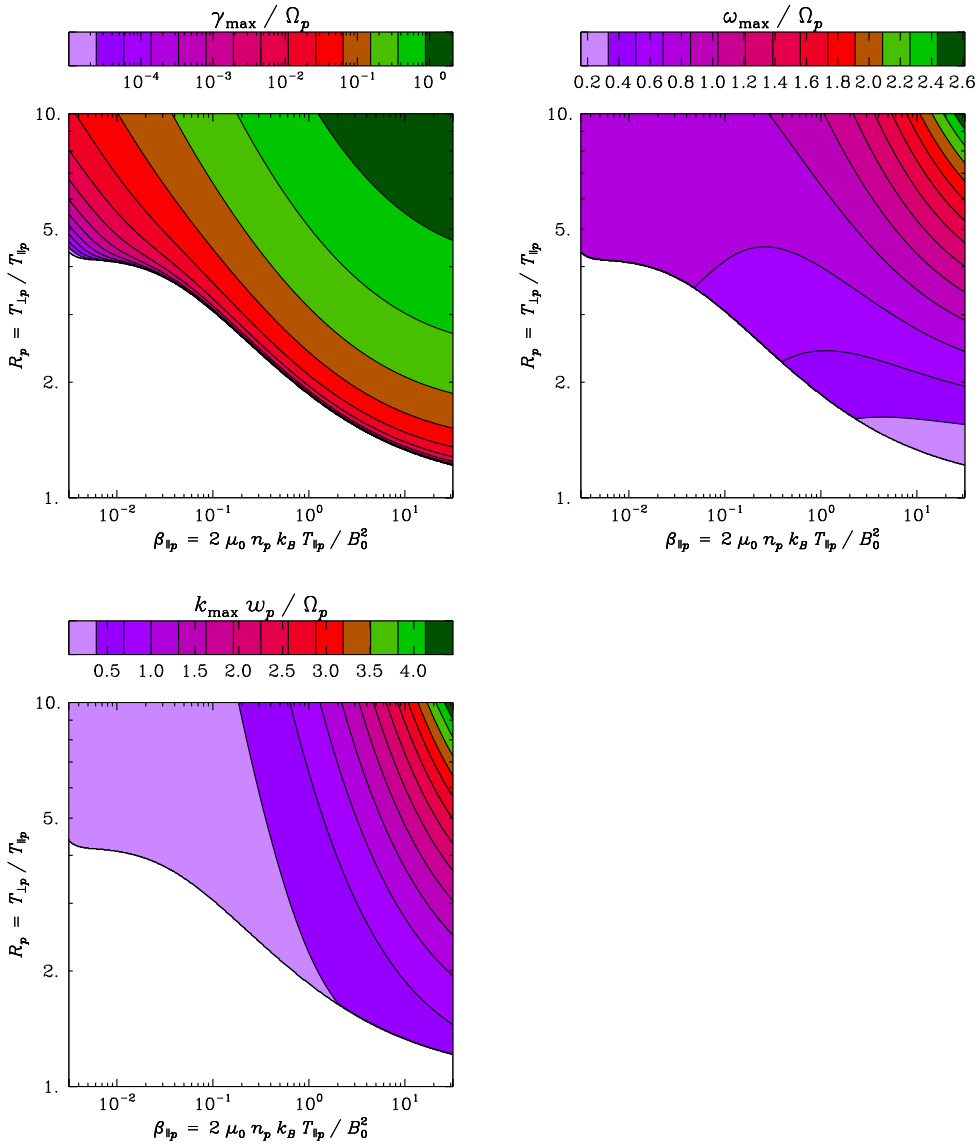

Figure 6.7.— Plots of $\gamma_{\max}$ (upper-left), $\omega_{\max}$ (upper-right), and $k_{\max}$ (lower-left) as functions of $\beta_{\|p}$ and R_p for the proton-driven cyclotron instability. These plots were generated by using the default value for each of the four `SRCH` parameters (see Table 6.1). No plot of $\theta_{\max}$ was necessary since, being one-dimensional, the cyclotron instability always has $\theta_{\max} = 0°$ by definition.

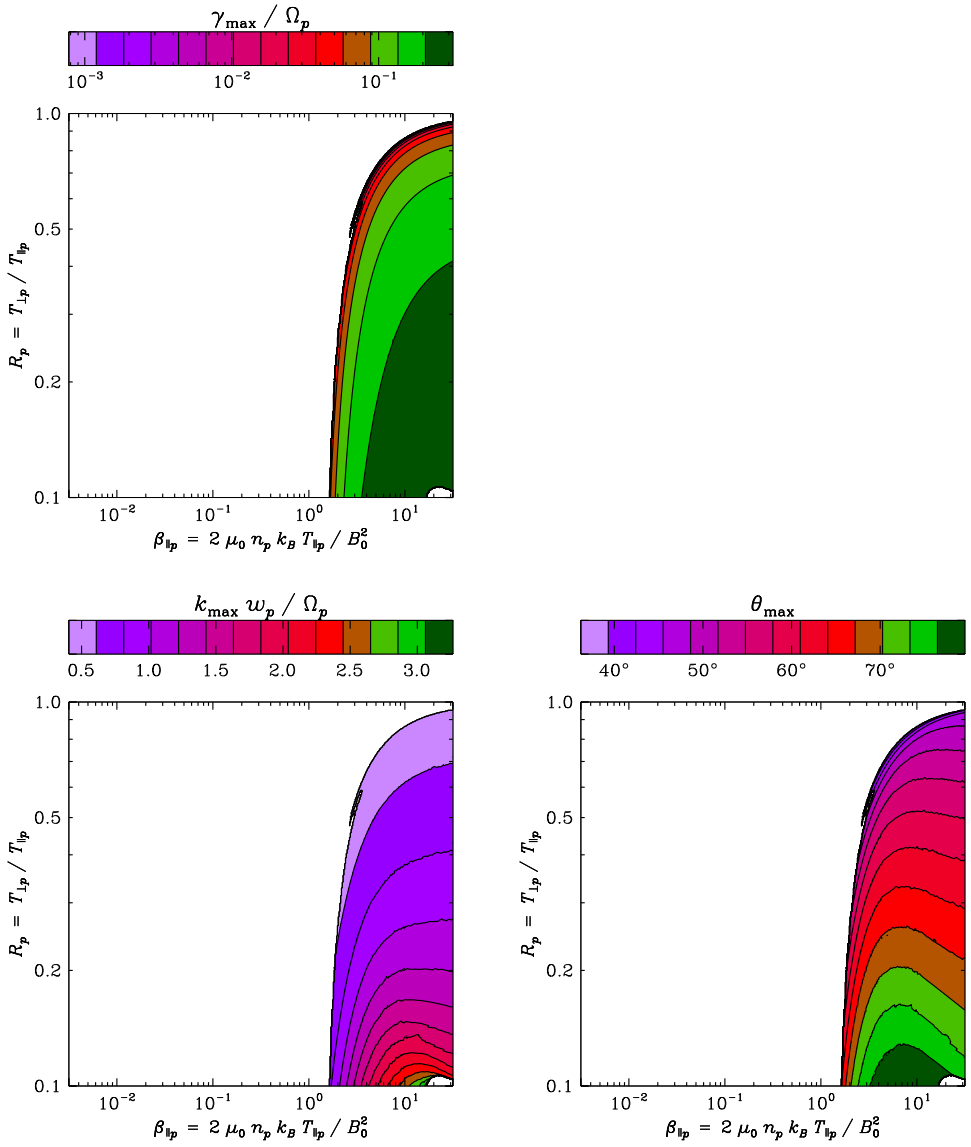

Figure 6.8.— Plots of $\gamma_{\max}$ (upper-left), $k_{\max}$ (lower-left), and $\theta_{\max}$ (lower-right) as functions of $\beta_{\|p}$ and R_p for the proton-driven oblique-firehose instability. These plots were generated by using the default value for each of the four `SRCH` parameters (see Table 6.1). No plot of $\omega_{\max}$ was necessary since, being two-dimensional, the oblique firehose instability always has $\omega_{\max} = 0$.

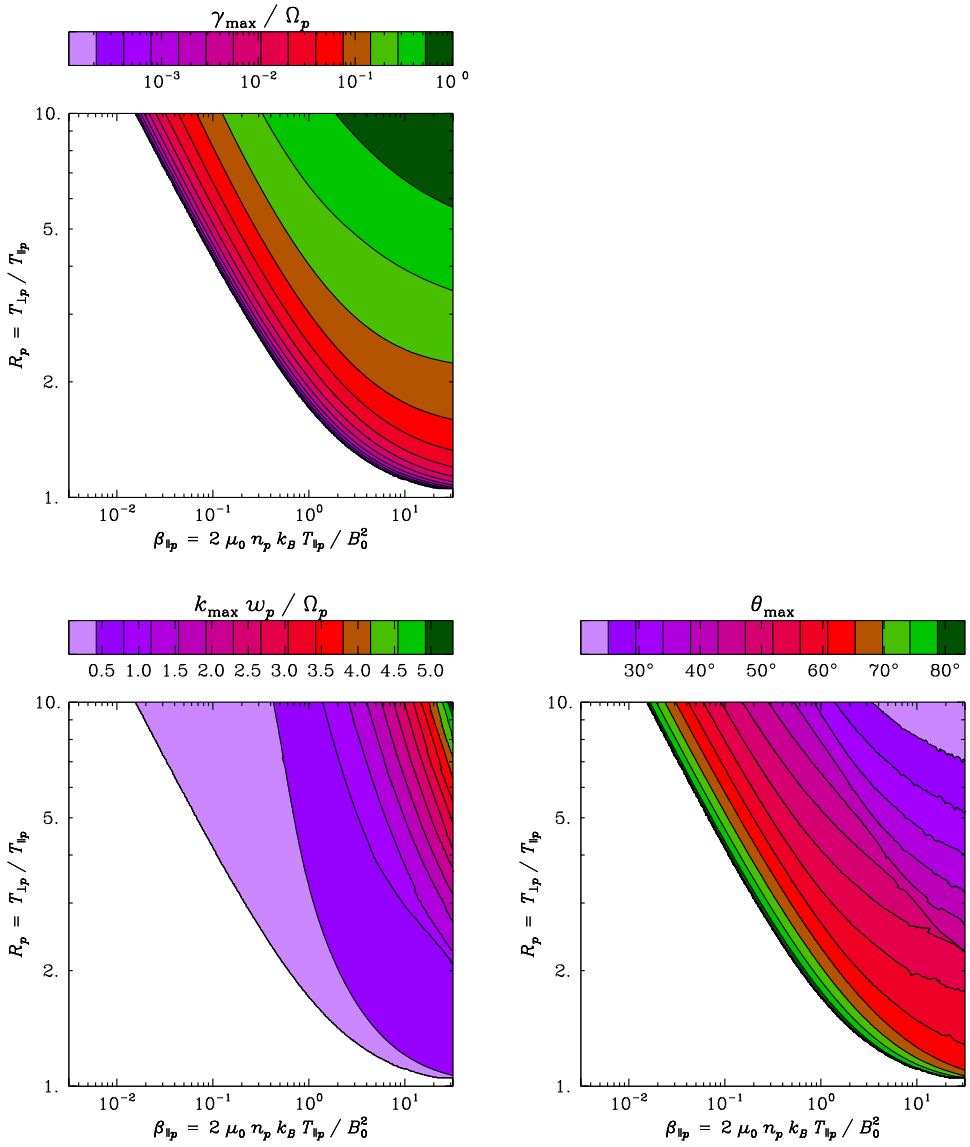

Figure 6.9.— Plots of $\gamma_{\max}$ (upper-left), $k_{\max}$ (lower-left), and $\theta_{\max}$ (lower-right) as functions of $\beta_{\parallel p}$ and R_p for the proton-driven mirror instability. These plots were generated by using the default value for each of the four `SRCH` parameters (see Table 6.1). No plot of $\omega_{\max}$ was necessary since, being two-dimensional, the mirror instability always has $\omega_{\max} = 0$.

Instability	Fit Parameters		
	a	b	β_0
Parallel Firehose	-1.144	0.774	-0.0619
Cyclotron	$+1.001$	0.330	-0.0000
Oblique Firehose	-1.134	0.910	$+0.3617$
Mirror	$+1.054$	0.600	-0.0031

Table 6.2: Thresholds for one- and two-dimensional instabilities driven by proton temperature anisotropy. In deriving these thresholds, only the default values of the `SRCH` parameters were used (see Table 6.1). These thresholds correspond to the instability growth rate contour $\gamma_{\max} = 10^{-2}\,\Omega_p$ (see Equation 6.2) as fit to the model given in Equation 6.4.

As stated above (see Equation 6.2), an instability's threshold was taken to be the contour of $\gamma_{\max} = 10^{-2}\,\Omega_p$ in the $(\beta_{\parallel p}, R_p)$-plane. For each of these four instabilities, this contour was extracted from its corresponding plot of $\gamma_{\max}(\beta_{\parallel p}, R_p)$ and fit to the model specified by Equation 6.4. The results of these fits are listed in Table 6.2.

Figure 6.10 shows how these theoretical instability thresholds compare to the observed distribution of $(\beta_{\parallel p}, R_p)$-values from the *Wind*/FC ion spectra. The distribution was generated by sorting the selected observations (see Chapter 4) into a 50×50 grid of logarithmically-spaced bins in the $(\beta_{\parallel p}, R_p)$-plane. The number of observations, n, in each bin was tallied, and bins with $n < 16$ were discarded as statistically insignificant. The value of the probability distribution $p(\beta_{\parallel p}, R_p)$ was estimated for each bin by dividing n by the bin's widths, $\Delta\beta_{\parallel p}$ and ΔR_p, and by the total number of spectra, N. The theoretical thresholds specified in Table 6.2 for the proton temperature anisotropy instabilities are plotted over this empirical distribution.

Figure 6.10, like similar figures presented by Hellinger et al. (2006) and Bale et al. (2009), provides strong evidence that instabilities driven by proton temperature anisotropy limit the

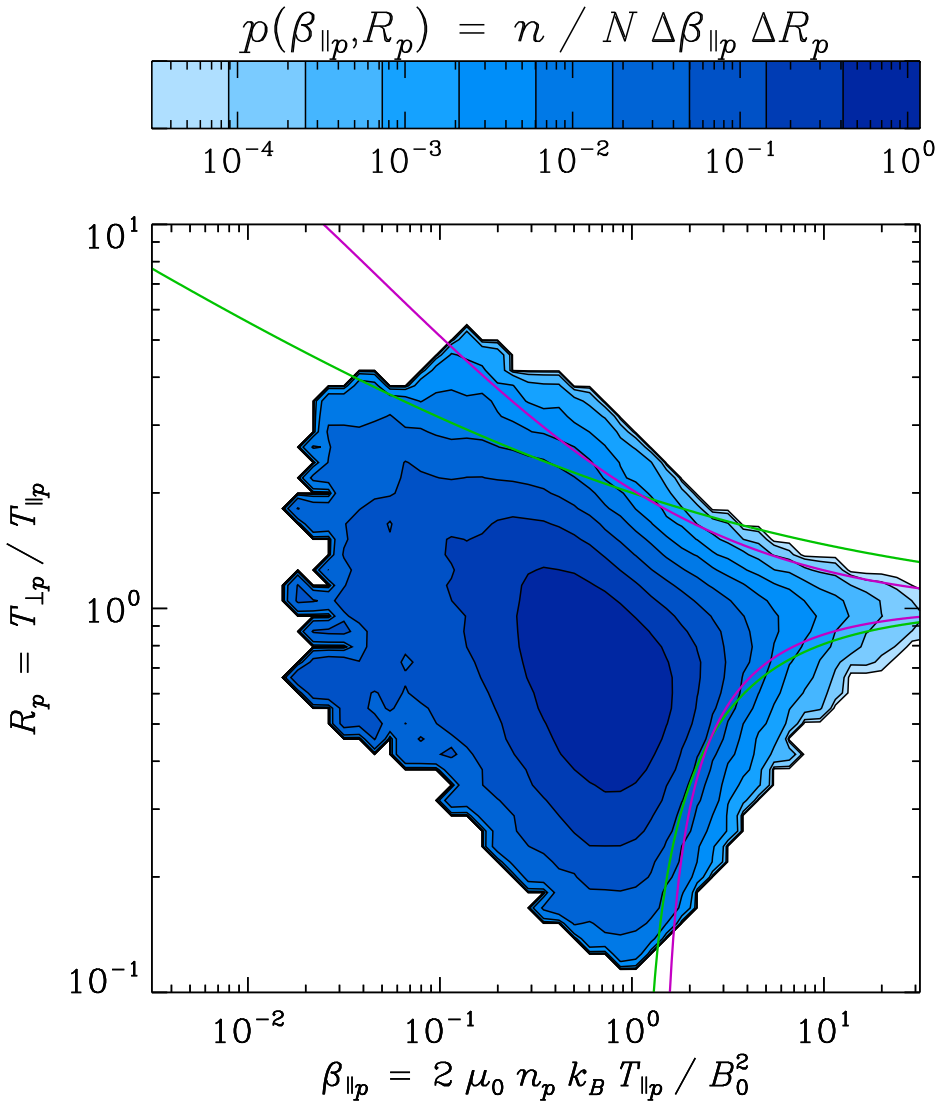

Figure 6.10.— Probability distribution of $(\beta_{\parallel p}, R_p)$-values from *Wind*/FC ion spectra (see Chapter 4). Overlaid curves show the thresholds of the proton temperature anisotropy instabilities given in Table 6.2, all of which were generated using the default values of the four `SRCH` parameters (see Table 6.1). The green curves correspond to the one-dimensional (i.e., parallel firehose and cyclotron) instabilities, and the magenta curves to the two-dimensional (i.e., oblique firehose and mirror) instabilities.

range of R_p-values observed in the solar wind. As the value of $\beta_{\parallel p}$ increases, the observed range of R_p-values narrows and the theoretical instability thresholds likewise converge toward $R_p = 1$. However, both studies noted that the distribution of proton observations is more consistent with the thresholds of the two-dimensional instabilities than with those of the one-dimensional instabilities. In Figure 6.10, this effect is borne out especially for $R_p > 1$, where the contours of $p(\beta_{\parallel p}, R_p)$ are more closely aligned with the mirror instability threshold than with the cyclotron instability threshold. Curiously, this holds true even at $\beta_{\parallel p}$-values for which the cyclotron instability theoretically places a stricter limit on $R_p > 1$ than the mirror instability. The cause of this apparent inconsistency remains a mystery. One possible explanation is that the preceding analysis only considered the thermal cores of the ion VDF's and explicitly assumed them to be bi-Maxwellian. Numerous studies (e.g., Hellinger & Trávníček, 2011, and references therein) have shown that other non-Maxwellian features in ion VDF's (e.g., beams and halos) can significantly impact the overall stability of the plasma. Alternatively, Bale et al. (2009) has speculated that two-dimensional instabilities may be more efficient at scattering particles in phase space despite their potentially lower growth rates because they are associated with non-propagating modes (i.e., $\omega_{\max} = 0$). Since these waves, by definition, have zero phase speed, they resonate with the thermal core of the VDF, which contains the majority of particles. In contrast, modes associated with one-dimensional instabilities generally have large phase speeds, so they resonate with the less-populated superthermal portion of the VDF. Hybrid expanding box simulations of the proton parallel and oblique firehose instabilities by Matteini et al. (2006) and Matteini et al. (2011) seem to support this interpretation; the former instability was found primarily to deform the wings of the proton VDF while the latter had a much greater impact on the plasma's overall trajectory through the $(\beta_{\parallel p}, R_p)$-plane.

6.6 Dependence of Thresholds on Plasma Parameters

This thesis project also explored how changes to the values of the four SRCH parameters listed in Table 6.1 affected the theoretical instability thresholds. These parameters were varied one at a time, and the results are shown in Figure 6.11, which contains four versions of the plot shown in Figure 6.10. Each one shows the probability distribution $p(\beta_{\parallel p}, R_p)$ and the default instability thresholds from Figure 6.10. However, each plot also shows additional instability thresholds (represented with dashed, dotted, and dash-dotted curves) where the value of one of the SRCH parameters in Table 6.1 was changed from its default value. The upper-left plot of Figure 6.10 considers variations in the value of $n_\alpha \,/\, n_p$, the upper-right plot $T_{\parallel\alpha} \,/\, T_{\parallel p}$, the lower-left plot ζ, and the lower-right plot $\Delta v_{\parallel\alpha p} \,/\, c_A$. The parameterizations (based on Equation 6.4) of these instability thresholds are listed in Table 6.3 for the one-dimensional instabilities and Table 6.4 for their two-dimensional counterparts. However, as noted in Section 5.5, variations in $\Delta v_{\parallel\alpha p} \,/\, c_A$ could only be considered for the one-dimensional instabilities since $\Delta v_{\parallel\alpha p} \,/\, c_A$ is essentially locked to zero (its default value) in the EAN code.

The effects that varying the values of the four SRCH parameters had on the instability thresholds were non-trivial; some thresholds were quite insensitive to the value of one parameter but much more affected by the value of another. However, a visual inspection of Figure 6.11 reveals that the threshold of none of the instabilities was particularly dependent on any of these four parameters. The parameters in Table 6.1 all relate the bulk properties of the α-particles to those of the protons, so presumably the α-particles have relatively little overall impact on the instability thresholds of the far more abundant protons. Indeed, Figure 6.11 reveals virtually no variation in the two-dimensional instability thresholds. Changes to the SRCH parameters had a greater effect on the one-dimensional instability thresholds, which

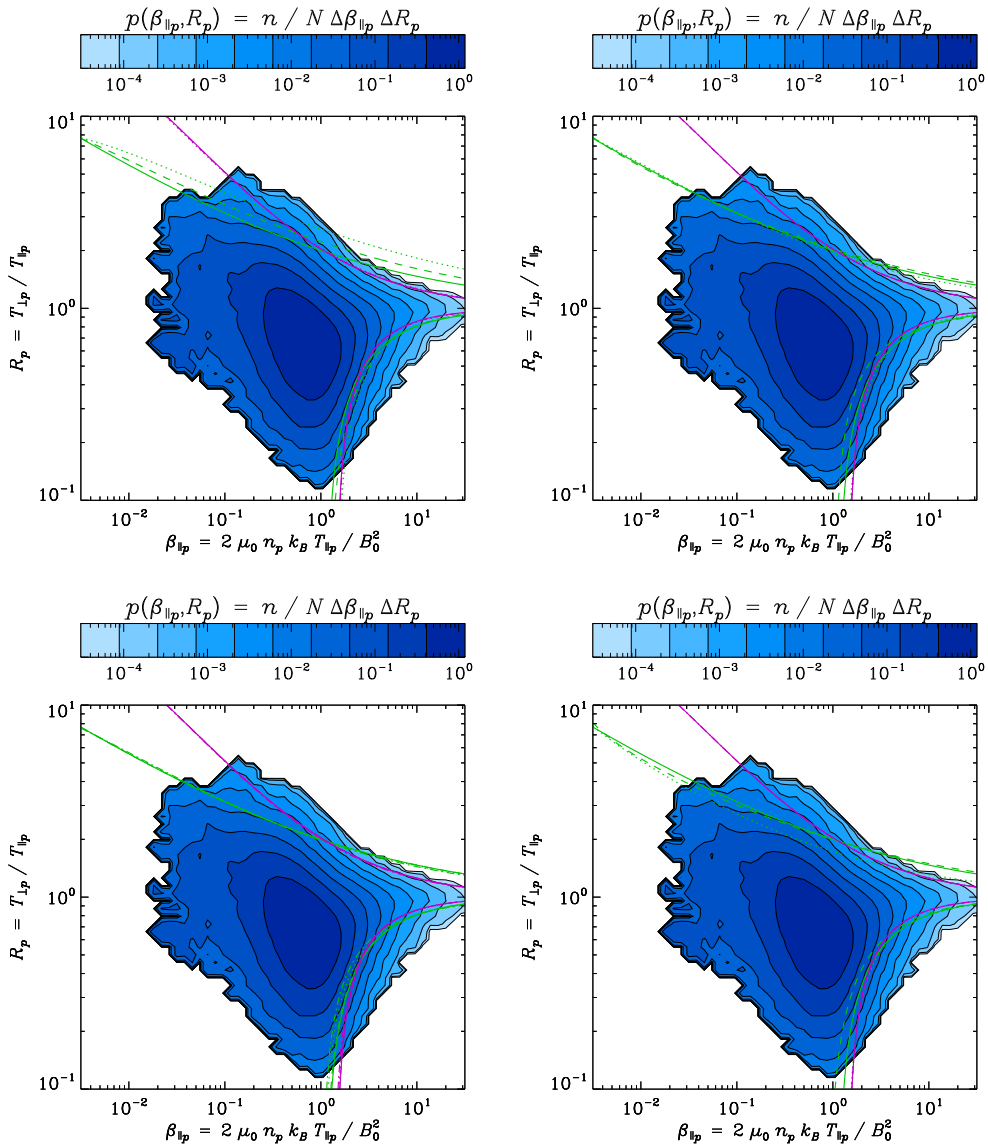

Figure 6.11.— Plots of $p(\beta_{\parallel p}, R_p)$ from *Wind*/FC ion spectra and the thresholds given in Tables 6.3 and 6.4 (green for one-dimensional, magenta for two-dimensional). The solid curves were generated with default values for all four `SRCH` parameters, but, for the others, one parameter had an alternative value. In the upper-left, $n_\alpha/n_p = 0.10$ (dashed) and 0.20 (dotted). In the upper-right, $T_\alpha / T_p = 2.00$ (dashed) and 8.00 (dotted). In the lower-left, $\zeta = 0.05$ (dashed), 0.25 (dotted), and 0.50 (dash-dotted). In the lower-right, $\Delta v_{\parallel \alpha p} / c_A = -0.50$ (dashed) and $+0.50$ (dotted).

SRCH Parameters				Proton Parallel Firehose			Proton Cyclotron		
$n_\alpha \,/\, n_p$	$T_{\parallel\alpha} \,/\, T_{\parallel p}$	ζ	$\Delta v_{\parallel\alpha p} \,/\, c_A$	a	b	β_0	a	b	β_0
0.05	4.00	0.00	0.00	−1.144	0.774	−0.0619	+1.001	0.330	−0.0000
0.10	4.00	0.00	0.00	−1.586	0.900	−0.4623	+1.228	0.305	−0.0007
0.20	4.00	0.00	0.00	−1.566	0.916	−0.1769	+1.587	0.283	−0.0029
0.05	**2.00**	0.00	0.00	−0.682	0.563	+0.5493	+1.046	0.311	+0.0007
0.05	**8.00**	0.00	0.00	−1.300	0.863	−0.0031	+0.938	0.353	−0.0007
0.05	4.00	**0.05**	0.00	−1.112	0.762	−0.0506	+1.000	0.330	−0.0000
0.05	4.00	**0.25**	0.00	−0.973	0.714	+0.0774	+0.990	0.336	−0.0003
0.05	4.00	**0.50**	0.00	−0.787	0.627	+0.3417	+0.976	0.345	−0.0008
0.05	4.00	0.00	**−0.50**	−0.829	0.703	+0.2340	+0.996	0.304	+0.0016
0.05	4.00	0.00	**+0.50**	−0.963	0.708	+0.4484	+0.729	0.371	+0.0007

Table 6.3: Thresholds for one-dimensional proton temperature anisotropy instabilities for different values of the SRCH parameters. Any SRCH parameter value that is not its default is printed in **boldface**. The first row of this table corresponds to the case where all SRCH parameters were set to their default values, so these thresholds also appear in Table 6.2. All thresholds in this table correspond to the instability growth rate contour $\gamma_{\max} = 10^{-2}\,\Omega_p$ (see Equation 6.2) as fit to the model given in Equation 6.4.

SRCH Parameters			Proton Oblique Firehose			Proton Mirror		
$n_\alpha \,/\, n_p$	$T_{\parallel\alpha} \,/\, T_{\parallel p}$	ζ	a	b	β_0	a	b	β_0
0.05	4.00	0.00	−1.134	0.910	+0.3617	+1.054	0.600	−0.0031
0.10	4.00	0.00	−1.096	0.889	+0.4154	+1.058	0.595	−0.0027
0.20	4.00	0.00	−1.060	0.857	+0.4140	+1.064	0.587	−0.0022
0.05	**2.00**	0.00	−1.195	0.931	+0.2444	+1.051	0.600	−0.0030
0.05	**8.00**	0.00	−1.127	0.910	+0.3913	+1.057	0.600	−0.0031
0.05	4.00	**0.05**	−1.147	0.914	+0.3248	+1.052	0.600	−0.0031
0.05	4.00	**0.25**	−1.178	0.924	+0.2483	+1.045	0.603	−0.0032
0.05	4.00	**0.50**	−1.204	0.933	+0.1737	+1.028	0.607	−0.0034

Table 6.4: Thresholds for two-dimensional proton temperature anisotropy instabilities for different values of the SRCH parameters. The first row of this table corresponds to the case where all SRCH parameters were set to their default values, so these thresholds also appear in Table 6.2. All thresholds in this table correspond to the instability growth rate contour $\gamma_{\max} = 10^{-2}\,\Omega_p$ (see Equation 6.2) as fit to the model given in Equation 6.4. Each threshold was calculated assuming $\Delta v_{\parallel\alpha p} \,/\, c_A = 0.00$ since the EAN code cannot consider any other value for this parameter.

seem to have been most sensitive to the values of n_α / n_p and $\Delta v_{\parallel \alpha p} / c_A$. Increasing the value of n_α / n_p caused the one-dimensional instability thresholds to move farther from $R_p = 1$ for all $\beta_{\parallel p}$-values; presumably, the presence of a greater abundance of isotropic α-particles has a stabilizing effect on the plasma. While the one-dimensional instability thresholds were also significantly effected by variations in $\Delta v_{\parallel \alpha p} / c_A$, the nature of these changes cannot be so easily characterized or intuitively explained.

Chapter 7

Instability Constraints on α-Particle Temperature Anisotropy

The structure of this chapter is very similar to that of Chapter 6. While that chapter focuses on proton temperature anisotropy instabilities, this chapter discusses those associated with α-particles.

Section 7.1 introduces the concept of α-particle temperature anisotropy instabilities, and Sections 7.2 and 7.3 explore how anisotropy correlation and differential flow, respectively, affect them. Some of the complications that arise from the presence of protons in the plasma are discussed in Section 7.4. Section 7.5 presents thresholds for the α-particle instabilities for the default plasma conditions, while Section 7.6 considers other values for these parameters.

7.1 Overview of α-Particle Instabilities

Given the strong evidence in Chapter 6 that instabilities limit the observed distribution of R_p-values in the solar wind, do similar limits exist on R_α-values? The excitation of instabilities driven by α-particle temperature anisotropy has received relatively little attention in the literature. Some studies, such as those of Gary & Winske (1993) and Liu et al. (2007), have considered how anisotropic α-particles affect plasma already unstable due to the proton-driven cyclotron instability, which is similar to the discussion of the ζ-parameter in Chapter 6. A more extensive theoretical and observational analysis of the α-particle cyclotron instability was carried out by Gary et al. (2003). The simulations of Hellinger et al. (2005) and Lu et al. (2006) modeled a plasma with anisotropic α-particles and incorporated the propagation of both parallel and oblique electromagnetic fluctuations, but their analyses were limited to only a few sets of initial conditions.

In some circles, the very notion of α-particle temperature anisotropy instabilities has been dismissed as unlikely. Even though the α-particles are typically hotter than the protons (see Figure 4.7), their low relative abundance means that they generate a much smaller fraction of the solar wind's particle pressure. From the standpoint of a single-fluid (e.g., MHD) model of the solar wind, this means that the α-particles would be incapable of destabilizing the plasma as a whole. However, in a collisionless regime, protons and α-particles resonate with different modes. Consequently, a sufficiently large departure of R_α from unity (even in the presence of isotropic protons) could cause some waves to grow and thereby trigger an instability.

The separate resonance conditions for protons and α-particles are exemplified in Figure 7.1, which shows plots for the cyclotron instability of $\omega_r(k)$ and $\gamma(k)$ for different values of

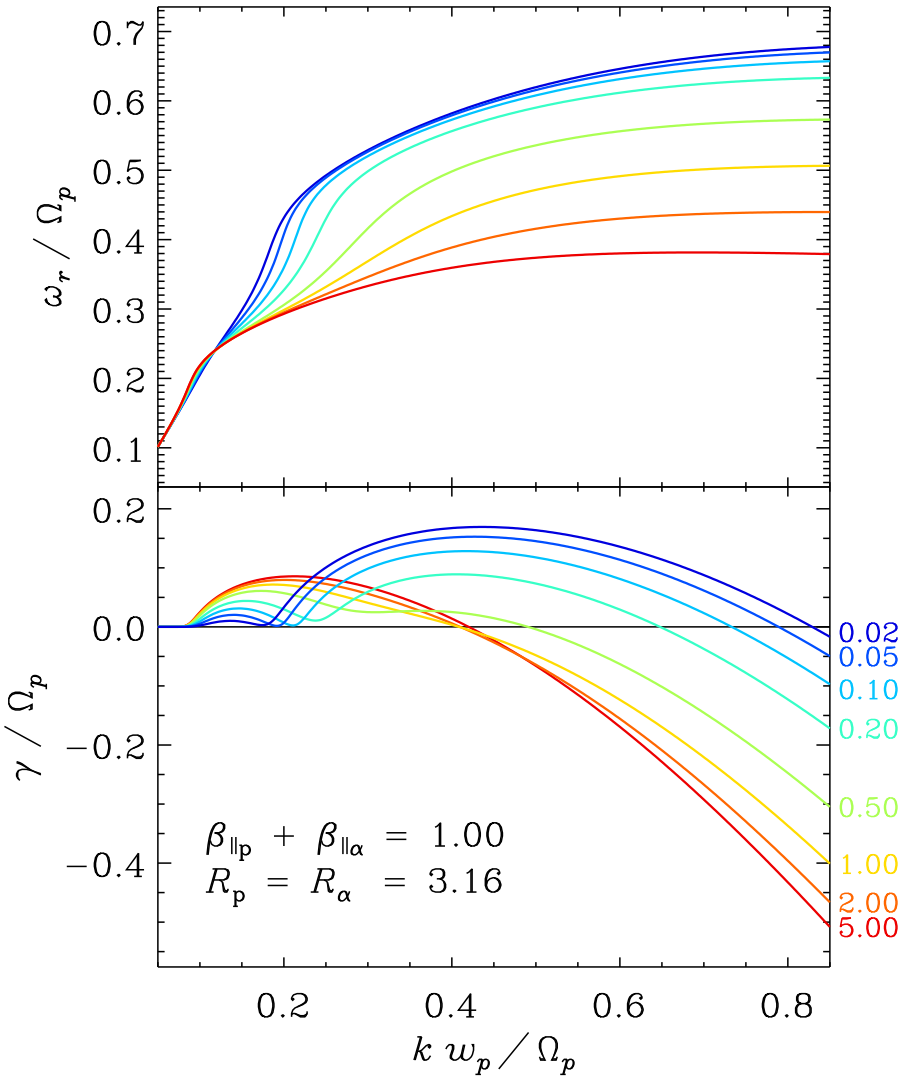

Figure 7.1.— Plots of ω_r (top) and γ (bottom) as functions of k for the cyclotron instability for $\beta_{\|p} + \beta_{\|\alpha} = 1.00$ and $R_p = R_\alpha = 3.16$. Each γ-curve is labeled with the value of $n_\alpha \,/\, n_p$ that was used in `T3` to generate it along with its corresponding ω_r-curve. The γ-curves for which the proton and α-particle number densities are comparable clearly show two peaks of similar heights, which indicates an instability driven by both particle species.

n_α / n_p. The values of R_p and R_α were kept equal and fixed to 3.16 and the value of the sum $\beta_{\parallel p} + \beta_{\parallel \alpha}$ was fixed at 1.00. Since both protons and α-particles are anisotropic, both contribute to destabilizing the plasma, but the relative influence of the two species depends on their relative abundance. For intermediate values of n_α / n_p, $\gamma(k)$ has two distinct peaks that are of comparable height: one at low-k corresponding to the α-particles and one at high-k for the protons. At small values of n_α / n_p, the peak at high-k is significantly higher than that at low-k, which suggests that the protons are primarily driving the instability. However, as the value of n_α / n_p increases, the low-k peak begins to dominate, which indicates that the α-particles become the driving species.

Separate proton and α-particle resonances also occur with two-dimensional instabilities. Figure 7.2 contains four plots of $\gamma(k, \theta)$ for the oblique firehose instability. While $\beta_{\parallel \alpha} = 3.00$ and $R_\alpha = 0.866$ for all plots, each was generated using a different R_p-value: 0.914, 0.911, 0.907, and 0.904. For the largest of the R_p-values (i.e., when the protons are most isotropic), the corresponding plot of $\gamma(k, \theta)$ contains only one peak, which is the result of the α-particle temperature anisotropy. As R_p decreases (i.e., as the protons becomes more anisotropic), though, a second, higher-k peak emerges, which indicates the action of the anisotropic protons. Decreasing the value of R_p causes the growth of not only the proton peak but the α-particle peak as well: even before the distinct proton peak emerges, making the protons more anisotropic causes $\gamma_{\max}$ to increase. Eventually, for sufficiently small $R_p < 1$, the proton peak completely overtakes the α-particle peak.

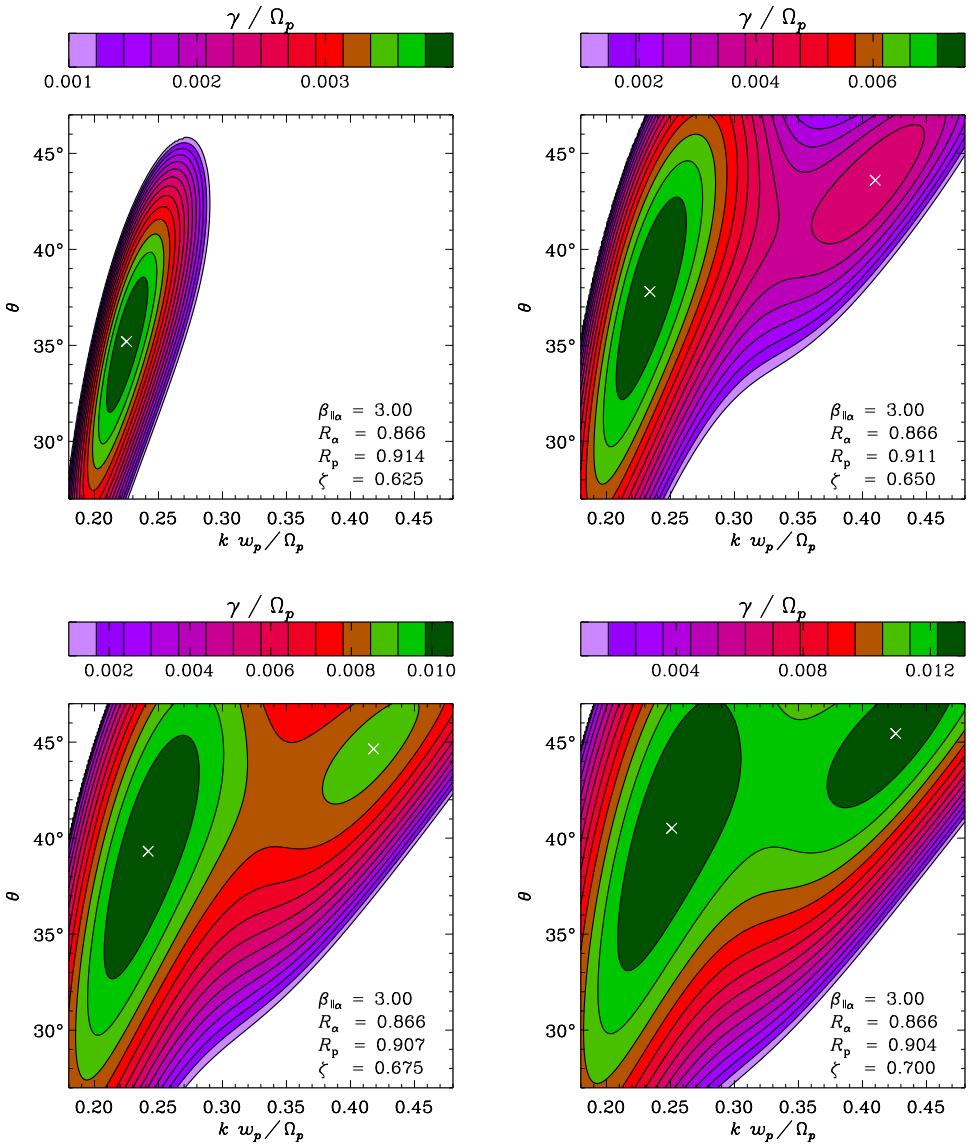

Figure 7.2.— Plots of γ as a function of k and θ for the oblique firehose instability for $\beta_{\parallel\alpha} = 3.00$ and $R_\alpha = 0.866$. Values of $\gamma < 10^{-3}\,\Omega_p$ are not shown. Each plot was generated with `EAN` and assuming a different R_p-value: 0.914 (upper-left), 0.911 (upper-right), 0.907 (lower-left), and 0.904 (lower-right). The corresponding ζ-values are respectively 0.625, 0.650, 0.675, and 0.700. However, for progressively smaller R_p-values, the proton peak emerges and eventually overtakes the α-particle peak.

7.2 Effects of Anisotropy Correlation

While Figures 7.1 and 7.2 indicate that (theoretically) the temperature anisotropy of α-particles alone can cause plasma to become unstable, they also show some of the complications that arise when multiple ion species are anisotropic. When the proton and α-particle peaks in γ have similar heights (see, e.g., Figures 7.1 and 7.2), the two species contribute roughly equally to the instability, which therefore cannot be classified as being primarily driven by either ion species.

A full analysis of plasma with anisotropic protons and α-particles was beyond the scope of this thesis project, but some treatment was still necessary. Figure 4.10 shows a correlation between R_p and R_α, which suggests that having only one ion species be anisotropic is unusual. However, so long as one ion species is significantly more anisotropic than the other (i.e., $0 \leq \zeta \ll 1$; see Equation 4.4), the former can be safely identified as the primary driver of any ensuing instability.

The effects that varying the value of ζ has on a given instability are not always intuitive. A larger ζ-value corresponds to the plasma having more free energy and therefore being less stable. For example, in Figure 7.2, increasing the value of ζ (even while ζ is still too small for a distinct proton peak to be present) causes the value of $\gamma_{\max}$ to likewise increase. However, $\gamma_{\max}$ is not a perfect proxy for overall plasma stability. Figure 7.3 shows plots for the α-particle cyclotron instability of $\omega_r(k)$ and $\gamma(k)$ for six different ζ-values: 0.00, 0.05, 0.10, 0.15, 0.20, and 0.25. The values of $\beta_{\|\alpha}$ and R_α were respectively fixed to 1.00 and 3.16. This figure clearly shows that, as ζ increases, $\gamma_{\max}$ slightly *decreases*. If $\gamma_{\max}$ is interpreted as quantifying the degree to which the plasma is unstable, then this would mean that making the protons more anisotropic actually stabilizes the plasma. However, such a conclusion

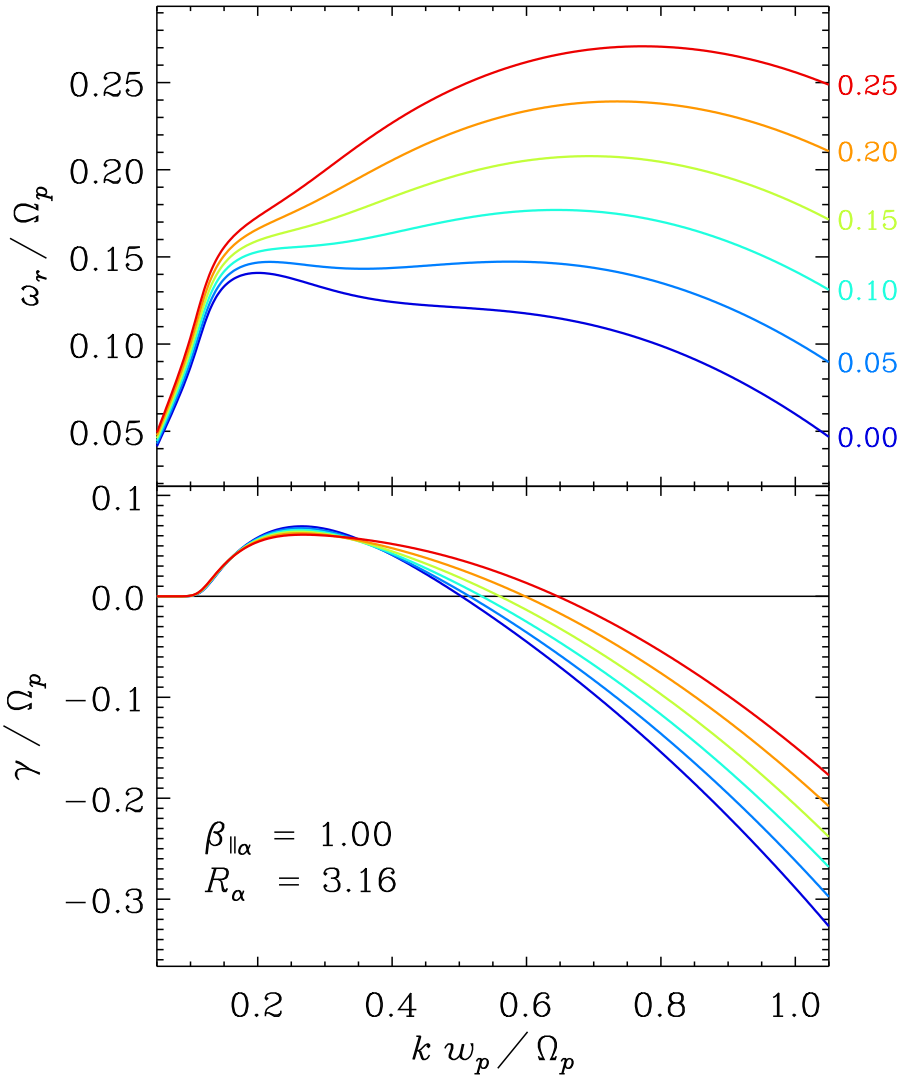

Figure 7.3.— Plots of ω_r (top) and γ (bottom) as functions of k for the α-driven cyclotron instability for $\beta_{\parallel\alpha} = 1.00$ and $R_\alpha = 3.16$. Each ω_r-curve is labeled with the ζ-value that was used in `T3` to generate it along with its corresponding γ-curve. As the value of ζ increases, the domain of k-values for which $\gamma(k) > 0$ becomes substantially wider, but the value of $\gamma_{\max}$ paradoxically (albeit slightly) decreases.

would be precipitous as it fails to consider all of the changes that occur to the γ-curve as the value of ζ is increased. Specifically, the decrease in $\gamma_{\max}$ is quite minor relative to the increase in the domain of k-values for which $\gamma(k)$ is positive. Thus, even though the maximum growth rate slightly decreases, substantially more waves are growing. This counterintuitive example underscores the limitations of $\gamma_{\max}$ that were discussed in Section 6.2.

7.3 Effects of α-Proton Differential Flow

As stated in Chapter 5, the `T3` code has the added feature of being able to consider the situation where the protons and α-particles are streaming relative to each other along the magnetic field (i.e., the case of $\Delta v_{\|\alpha p} \neq 0$). Differential flow between ion species, if sufficiently large, has been established as a driver of its own kinetic microinstabilities (see Schwartz, 1980, and references therein). However, the value of $\Delta v_{\|\alpha p}$ can also impact the growth rate of instabilities driven by ion temperature anisotropies. For the values of $\Delta v_{\|\alpha p}$ typically observed in the solar wind, this effect is relatively minor for proton temperature anisotropy instabilities (see the lower-right plot of Figure 6.11) but is somewhat more pronounced for some of their α-particle counterparts.

As an example, Figure 7.4 shows how the α-particle cyclotron instability is affected by α-proton differential flow. The plots of $\omega_r(k)$ and $\gamma(k)$ in this figure were generated using various values (both positive and negative) for $\Delta v_{\|\alpha p} \,/\, c_A$ while keeping fixed $\beta_{\|\alpha} = 1.00$ and $R_\alpha = 3.16$. While the ω_r-curves indicate a relatively strong dependence on the value of $\Delta v_{\|\alpha p} \,/\, c_A$, all of the γ-curves appear quite similar. Indeed, the greatest value of $\gamma_{\max}$ shown in Figure 7.4 is only 2.1 times the least. Furthermore, while Figure 7.4 considers values of $\left|\Delta v_{\|\alpha p}\right| \,/\, c_A$ up to 1.5., Figure 4.8 (bottom) indicates that values this high rarely occur in

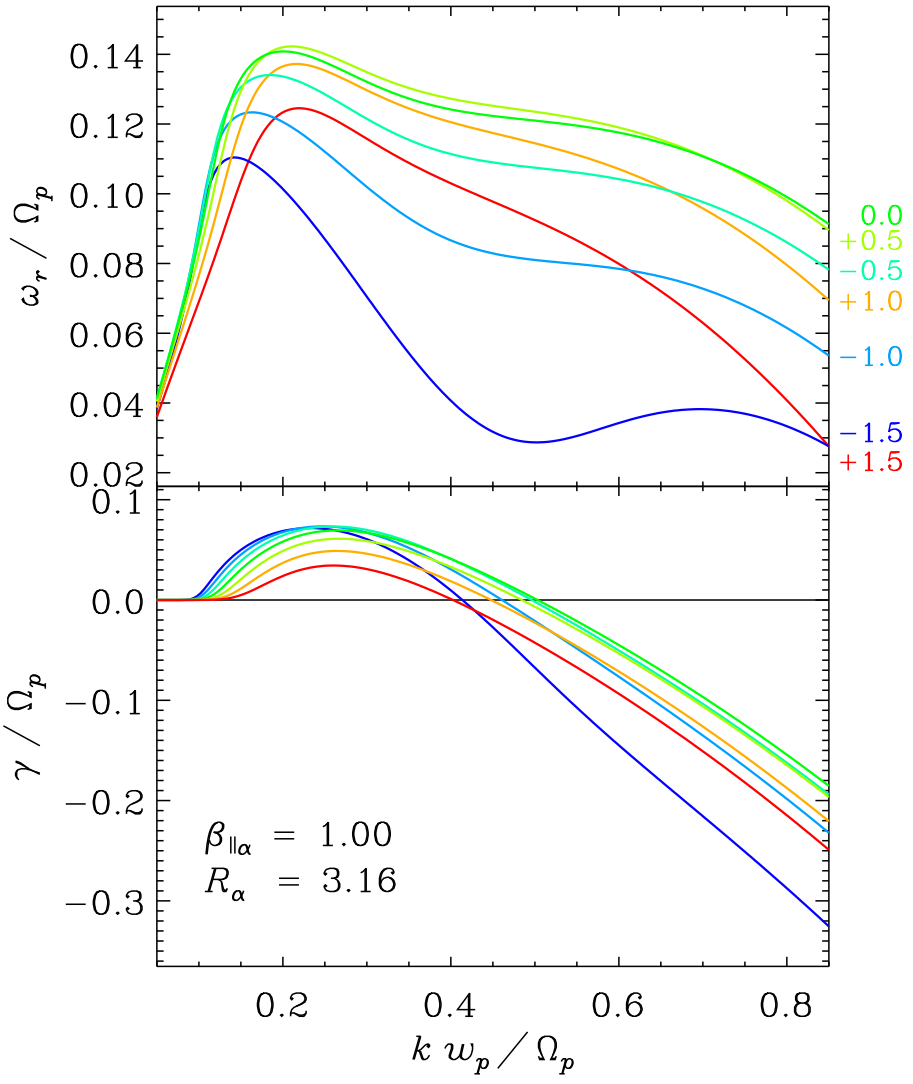

Figure 7.4.— Plots of ω_r (top) and γ (bottom) as functions of k for the α-driven cyclotron instability for $\beta_{\parallel\alpha} = 1.00$ and $R_\alpha = 3.16$. Each ω_r-curve is labeled with the value of $\Delta v_{\parallel\alpha p} \,/\, c_A$ that was used in `T3` to generate it along with its corresponding γ-curve.

Wind/FC data.

7.4 Effects of Stationary, Isotropic Protons

Section 6.2 contains various examples of how stationary, isotropic α-particles can affect proton temperature anisotropy instabilities. Unfortunately, stationary, isotropic protons can have similarly pathological effects on the α-particle instabilities.

Much of Section 6.2 is dedicated to examples of double peaks in $\gamma(k)$ and $\gamma(k, \theta)$, which occasionally result for proton instabilities due to the presence of isotropic α-particles. This double-peak phenomenon causes irregularities for the proton-driven parallel firehose, oblique firehose, and mirror instabilities (see Figures 6.6, 6.8, and 6.9, respectively).

Curiously, however, there is no clear evidence of the double-peak effect for the α-particle firehose instabilities: Figures 7.6 and 7.8 lack the "hook" structure that can be seen in Figures 6.6 and 6.8. Potentially, the double-peak effect does not occur for the α-particle firehose instabilities (at least for the plasma conditions considered in this study). Alternatively, its signature in the α-particle firehose instabilities may (for some reason) be much weaker than in the corresponding proton instabilities, or it may occur at $(\beta_{\parallel\alpha}, R_\alpha)$-values outside of the domain considered in this study.

Nevertheless, the double-peak effect clearly manifests itself for the α-particle mirror instability. Figure 7.5 shows plots for this instability of $\gamma(k, \theta)$. While all of the plots assumed $\beta_{\parallel\alpha} = 10.$, each was generated using a different R_α-value: 2.4, 2.5, 2.6, and 2.7. Together, these plots show two distinct peaks. For $R_\alpha = 2.5$, the lower-k peak is taller; however, for $R_\alpha = 2.6$, the higher-k peak is taller. This switching in the relative size of

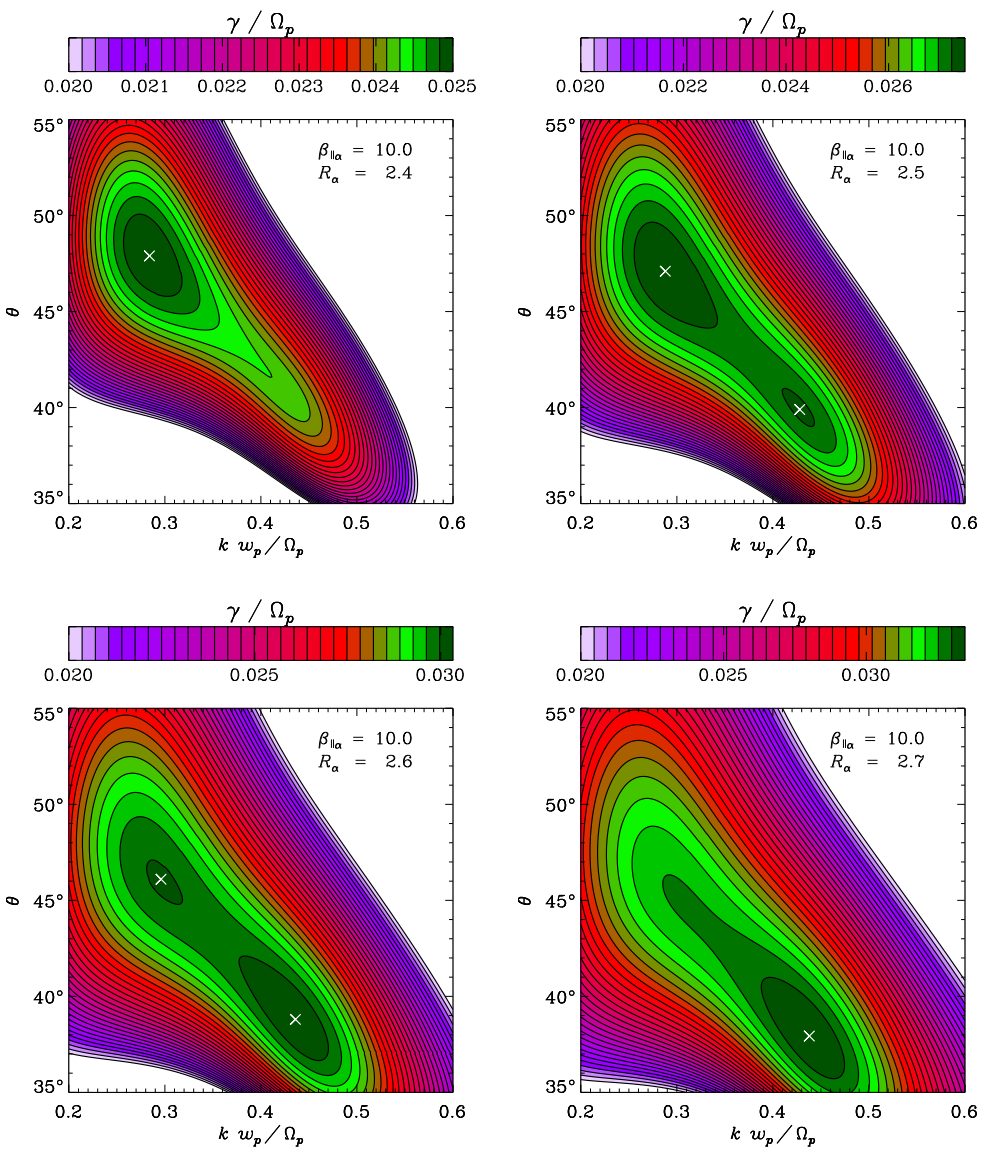

Figure 7.5.— Plots of γ as a function of k and θ for the α-driven mirror instability. Values of $\gamma < 10^{-3}\,\Omega_p$ are not shown. For each plot, the protons were assumed to be isotropic and to have no bulk flow relative to the α-particles. While $\beta_{\|\alpha} = 10.0$ was used for all four plots, each was generated using a different R_α-value: 2.4 (upper-left), 2.5 (upper-right), 2.6 (lower-left), and 2.7 (lower-right).

the two peaks results in the α-particle mirror instability having strong discontinuities in the $(\beta_{\parallel\alpha}, R_\alpha)$-plane, which are clearly apparent in Figure 7.9 (especially in the plot of $k_{\max}$). A similar but less-dramatic manifestation of this effect occurs with the proton mirror instability (see Figure 6.9).

7.5 Default Instability Thresholds

This section describes the analysis of the four α-particle temperature anisotropy instabilities using the default values of the four `SRCH` parameters listed in Table 6.1. The `SRCH` code was run in the manner described in Section 6.4 for each of the instabilities listed in Table 5.1. The results of this analysis are shown graphically in Figure 7.6 for the parallel firehose instability, Figure 7.7 for the cyclotron instability, Figure 7.8 for the oblique firehose instability, and Figure 7.9 for the mirror instability. Plots of $\gamma_{\max}(\beta_{\parallel\alpha}, R_\alpha)$ and $k_{\max}(\beta_{\parallel\alpha}, R_\alpha)$ appear in each of these figures. However, as explained in Section 6.5, plots of $\omega_{\max}(\beta_{\parallel\alpha}, R_\alpha)$ only appear in the figures for the one-dimensional instabilities, and plots of $\theta_{\max}(\beta_{\parallel\alpha}, R_\alpha)$ only appear in the figures for the two-dimensional instabilities.

Using the method described in Section 6.5, the threshold (as defined by Equation 6.2) of each α-particle instability was extracted and fit to the model given in Equation 6.4. These parameterizations of the α-particle instability thresholds are given in Table 7.1 along with those from Table 6.2 for the proton instabilities for reference.

The left-hand plot of Figure 7.10 is simply a reproduction of Figure 6.10, which shows the default proton instability thresholds plotted over the observed distribution of $(\beta_{\parallel p}, R_p)$-values from the *Wind*/FC ion spectra. As described in Section 6.5, the alignment of the

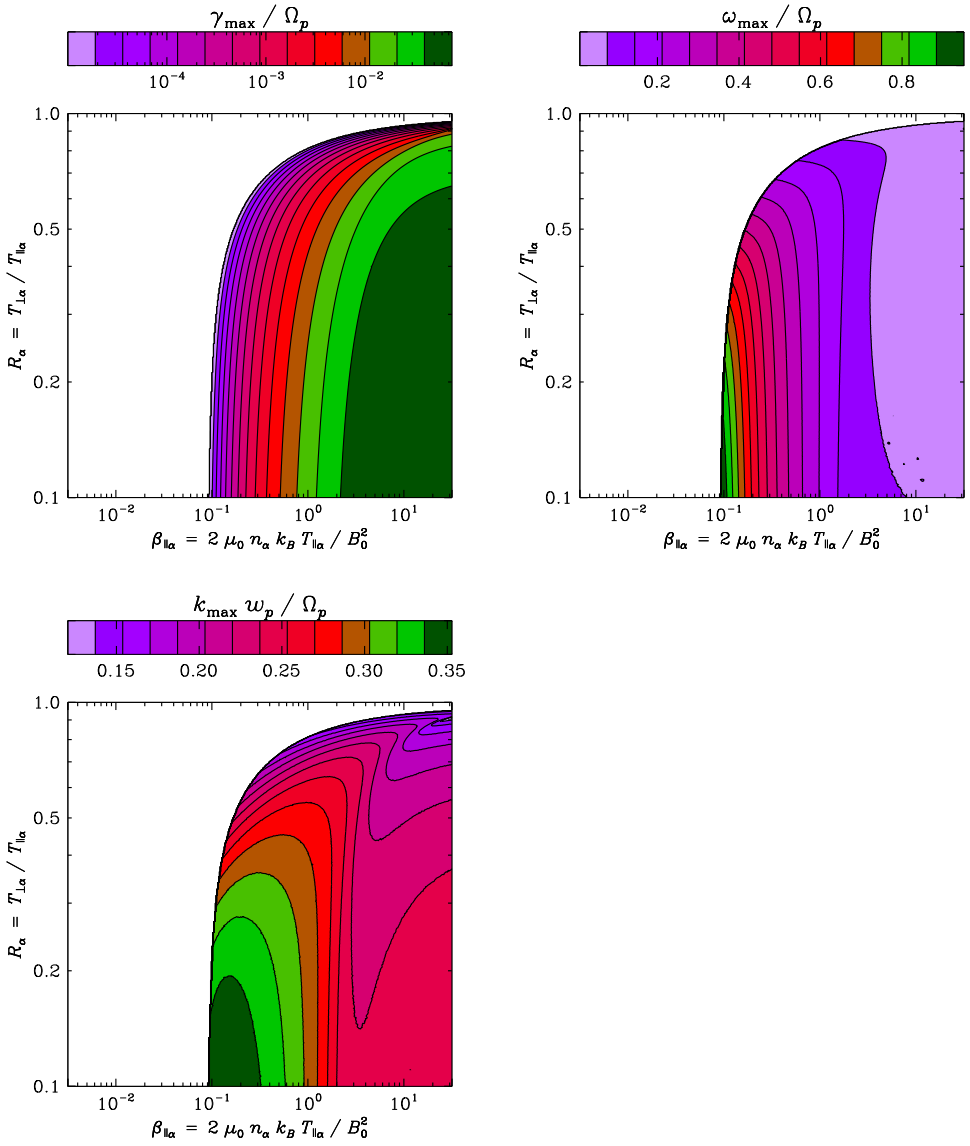

Figure 7.6.— Plots of $\gamma_{\max}$ (upper-left), $\omega_{\max}$ (upper-right), and $k_{\max}$ (lower-left) as functions of $\beta_{\|\alpha}$ and R_α for the α-driven parallel firehose instability. These plots were generated by using the default value for each of the four `SRCH` parameters (see Table 6.1). No plot of $\theta_{\max}$ was necessary since, being one-dimensional, the parallel firehose instability always has $\theta_{\max} = 0^\circ$ by definition.

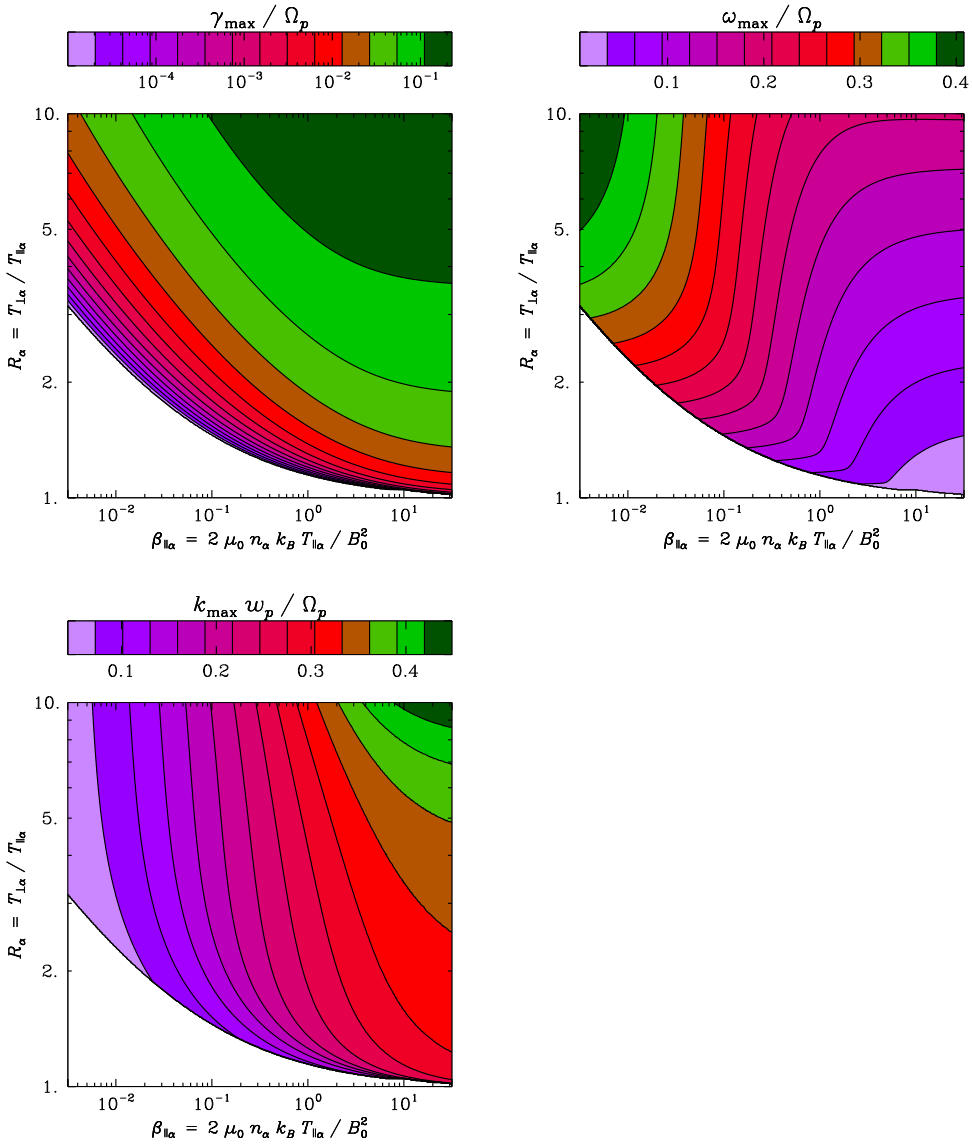

Figure 7.7.— Plots of $\gamma_{\max}$ (upper-left), $\omega_{\max}$ (upper-right), and $k_{\max}$ (lower-left) as functions of $\beta_{\|\alpha}$ and R_α for the α-driven cyclotron instability. These plots were generated by using the default value for each of the four `SRCH` parameters (see Table 6.1). No plot of $\theta_{\max}$ was necessary since, being one-dimensional, the cyclotron instability always has $\theta_{\max} = 0°$ by definition.

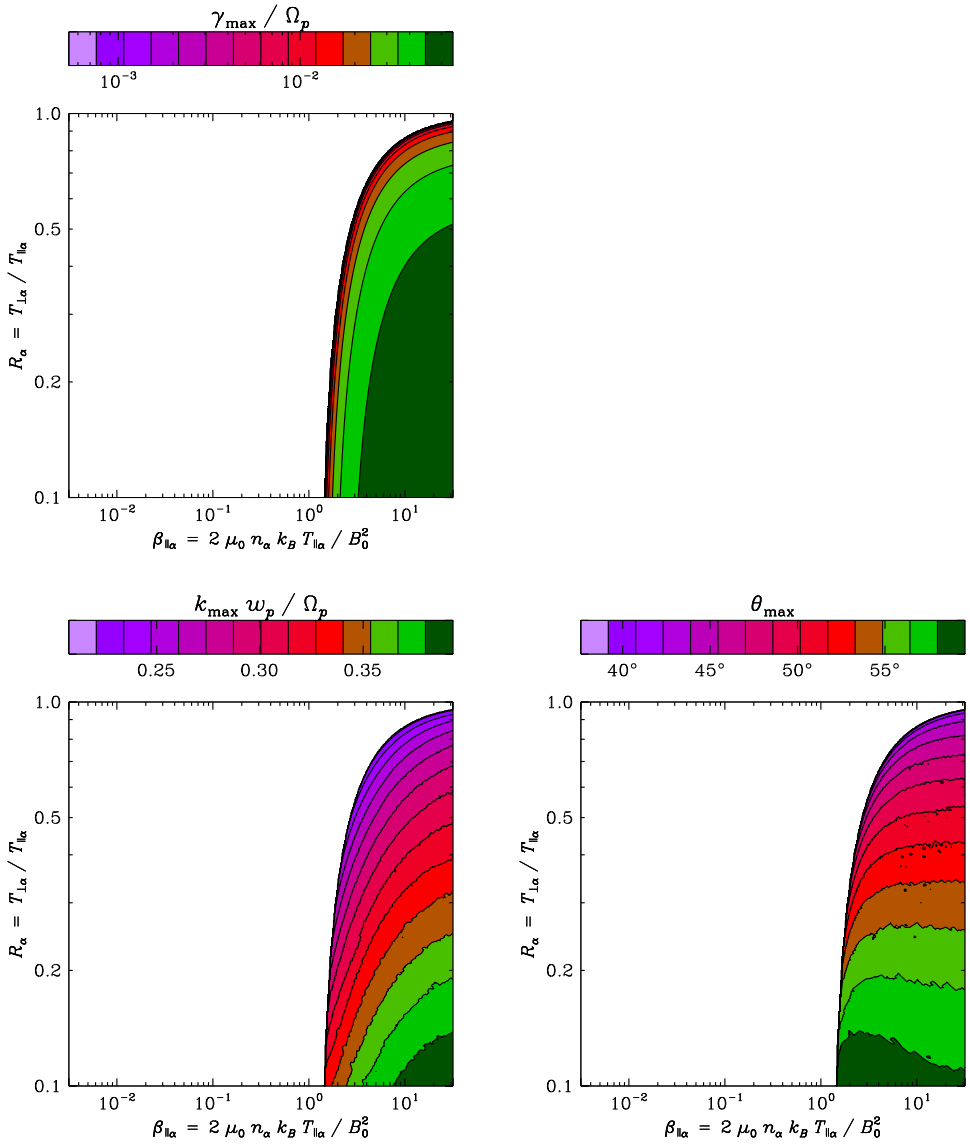

Figure 7.8.— Plots of $\gamma_{\max}$ (upper-left), $k_{\max}$ (lower-left), and $\theta_{\max}$ (lower-right) as functions of $\beta_{\|\alpha}$ and R_α for the α-driven oblique firehose instability. These plots were generated by using the default value for each of the four `SRCH` parameters (see Table 6.1). No plot of $\omega_{\max}$ was necessary since, being two-dimensional, the oblique firehose instability always has $\omega_{\max} = 0$.

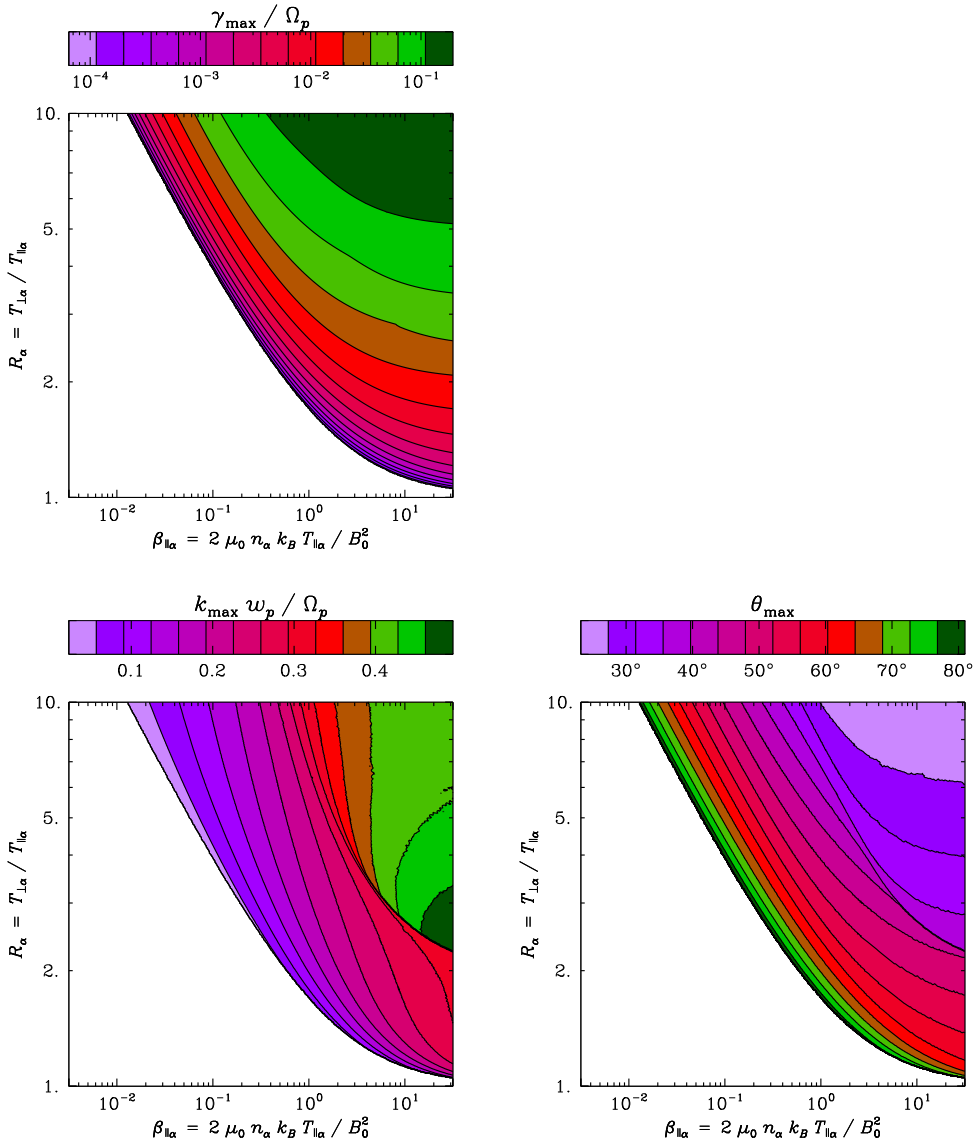

Figure 7.9.— Plots of $\gamma_{\max}$ (upper-left), $k_{\max}$ (lower-left), and $\theta_{\max}$ (lower-right) as functions of $\beta_{\parallel\alpha}$ and R_α for the α-driven mirror instability. These plots were generated by using the default value for each of the four `SRCH` parameters (see Table 6.1). No plot of $\omega_{\max}$ was necessary since, being two-dimensional, the mirror instability always has $\omega_{\max} = 0$.

Driving Species		Instability	Fit Parameters		
			a	b	β_0
$j = p$		Parallel Firehose	-1.144	0.774	-0.0619
		Cyclotron	$+1.001$	0.330	-0.0000
		Oblique Firehose	-1.134	0.910	$+0.3617$
		Mirror	$+1.054$	0.600	-0.0031
$j = \alpha$		Parallel Firehose	-0.624	0.505	$+0.2289$
		Cyclotron	$+0.480$	0.443	-0.0000
		Oblique Firehose	-1.106	0.839	$+0.2988$
		Mirror	$+1.515$	0.467	$+0.0069$

Table 7.1: Thresholds for one- and two-dimensional instabilities driven by either proton ($j = p$) or α-particle ($j = \alpha$) temperature anisotropy. In deriving these thresholds, only the default values of the `SRCH` physical parameters were used (see Table 6.1). These thresholds correspond to the instability growth rate contour $\gamma_{\max} = 10^{-2}\,\Omega_p$ (see Equation 6.2) as fit to the model given in Equation 6.4. The proton instability thresholds listed in this table are identical to those in Table 6.2 and are reproduced here for reference.

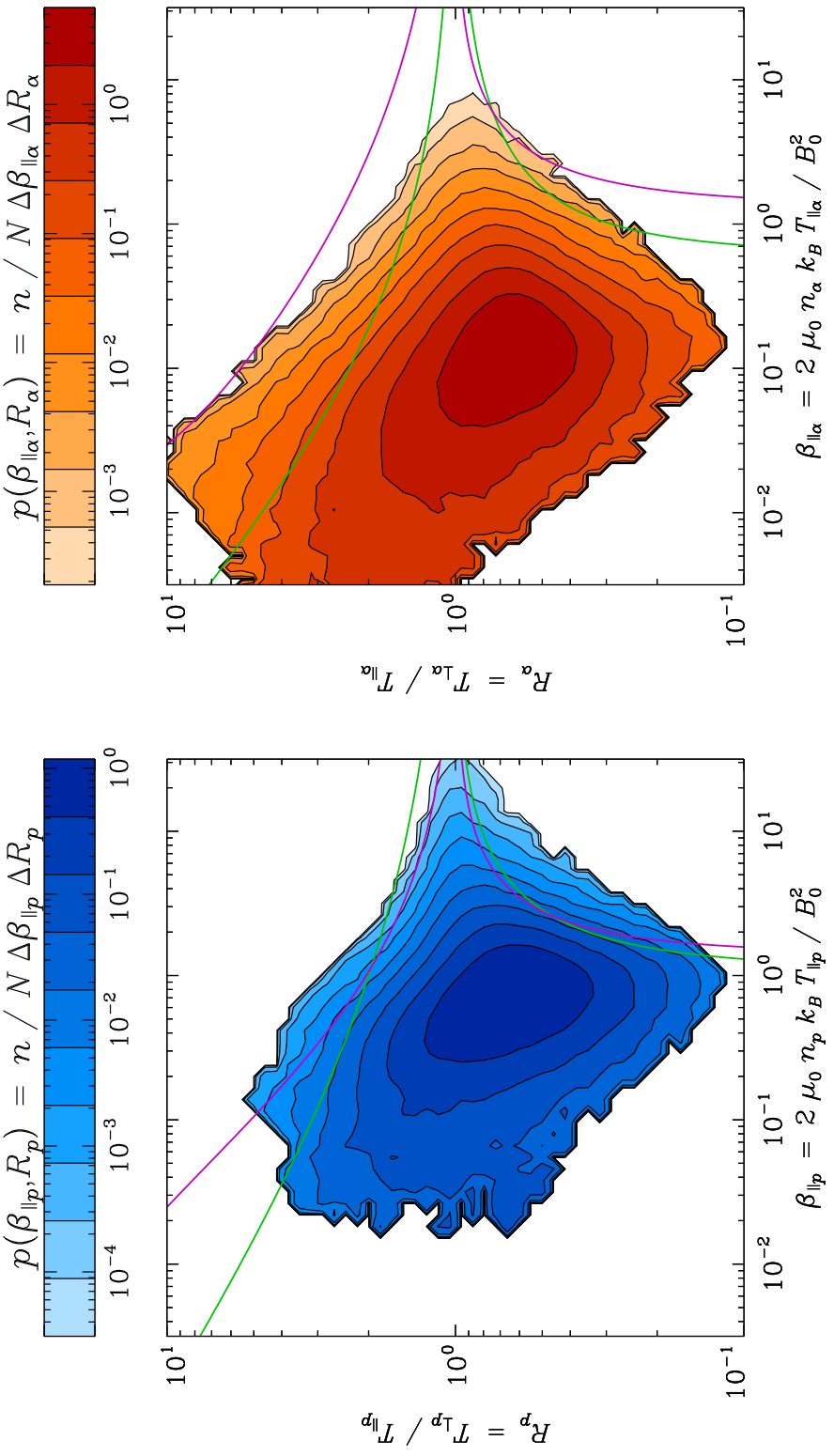

Figure 7.10.— Probability distributions of $(\beta_{\parallel p}, R_p)$ (left) and $(\beta_{\parallel \alpha}, R_\alpha)$ (right) from *Wind*/FC ion spectra (see Chapter 4). Overlaid curves show the thresholds of the proton (left) and α-particle (right) temperature anisotropy instabilities given in Table 7.1. The green curves correspond to the one-dimensional (i.e., parallel firehose and cyclotron) instabilities, and the magenta curves to the two-dimensional (i.e., oblique firehose and mirror) instabilities.

theoretical instability thresholds with the distribution of observations in this and similar plots generated by Hellinger et al. (2006) and Bale et al. (2009) has been interpreted as strong evidence that proton temperature anisotropy instabilities limit the range of R_p-values observed in the solar wind.

The right-hand plot of Figure 7.10 shows the α-particle counterpart of the left-hand plot: i.e., the default α-particle instability thresholds plotted over the observed distribution of $(\beta_{\parallel\alpha}, R_\alpha)$-values. Side-by-side, the two plots of Figure 7.10 are remarkably similar. In each, the observed range of R_j-values narrows as the value of $\beta_{\parallel j}$ increases, which is consistent with the actions of anisotropy-driven instabilities. Additionally, each plot shows a general agreement between the distribution of observations and the theoretical limits set by the instability thresholds (especially those for the two-dimensional instabilities). This suggests that the observed distribution of R_α-values is limited by α-particle temperature anisotropy instabilities just as that of R_p-values is limited by the corresponding proton instabilities.

However, Figure 7.10 shows that the agreement between the theoretical limits on temperature anisotropy and the observations thereof is significantly weaker for the α-particles than it is for the protons. This discrepancy may, in large part, stem from the low relative abundance of α-particles. Observationally, the signal from α-particles is significantly weaker than that of the protons, so the uncertainties in the parameter values of the former are typically much larger than those of the latter. Theoretically, as discussed in the next section, the low relative abundance of α-particles seems to make their instability thresholds generally more sensitive to the values of the parameters listed in Table 6.1. In fact, it is shown that a larger ζ-value produces α-particle instability thresholds that are considerably better-aligned with the observed distribution of $(\beta_{\parallel\alpha}, R_\alpha)$-values.

7.6 Dependence of Thresholds on Plasma Parameters

As with the proton instabilities (see Section 6.6), this study also used `SRCH` to explore how the alternative parameter values listed in Table 6.1 affected the α-particle instability thresholds. The results of this analysis are quantitatively summarized in Tables 7.2 and 7.3, which respectively list parameterizations (based on Equation 6.4) of the one- and two-dimensional α-particle instability thresholds. The first row of each table gives the thresholds for the default parameters values, which are also listed in Table 7.1. For the thresholds in each of the remaining rows, all but one of the parameters was set to its default value. However, while variations in the value of $\Delta v_{\parallel \alpha p} \,/\, c_A$ could be considered for the one-dimensional instabilities (see Table 7.2), this was not possible for their two-dimensional counterparts (see Table 7.3) because `EAN` does not allow non-zero differential flow (see Section 5.5).

The instability thresholds parameterized in Tables 7.2 and 7.3 are shown in Figure 7.11 plotted over copies of the probability distribution $p(\beta_{\parallel \alpha}, R_\alpha)$ from the right-hand plot of Figure 7.10. As usual, the thresholds of the one-dimensional instabilities are shown in green while those of the two-dimensional instabilities are shown in magenta. Each of the four plots in Figure 7.11 shows the default α-particle instability thresholds as solid curves. Additionally, the upper-left plot shows the thresholds for the alternative values of $n_\alpha \,/\, n_p$, the upper-right plot those for the alternative values of $T_{\parallel \alpha} \,/\, T_{\parallel p}$, the lower-left plot those for the alternative values of ζ, and the lower-right plot those for alternative values of $\Delta v_{\parallel \alpha p} \,/\, c_A$ (for the one-dimensional thresholds only due to the limitation of `EAN`).

A comparison of Figure 7.11 to Figure 6.11 (i.e., its proton counterpart) shows that, overall, the α-particle instability thresholds are more sensitive than their proton counterparts to the values of the parameters from Table 6.1. Most likely, this sensitivity stems from the

SRCH Parameters				α-Particle Parallel Firehose			α-Particle Cyclotron		
$n_\alpha \,/\, n_p$	$T_{\parallel\alpha} \,/\, T_{\parallel p}$	ζ	$\Delta v_{\parallel\alpha p} \,/\, c_A$	a	b	β_0	a	b	β_0
0.05	4.00	0.00	0.00	-0.624	0.505	$+0.2289$	$+0.480$	0.443	-0.0000
0.10	4.00	0.00	0.00	-0.642	0.554	$+0.2361$	$+0.522$	0.446	$+0.0001$
0.20	4.00	0.00	0.00	-0.685	0.593	$+0.2762$	$+0.587$	0.438	$+0.0001$
0.05	**2.00**	0.00	0.00	-1.101	0.562	$+0.2649$	$+0.635$	0.367	$+0.0013$
0.05	**8.00**	0.00	0.00	-0.555	0.546	$+0.1186$	$+0.484$	0.443	-0.0001
0.05	4.00	**0.05**	0.00	-0.612	0.557	$+0.0914$	$+0.491$	0.438	$+0.0001$
0.05	4.00	**0.25**	0.00	-0.535	0.694	-0.1017	$+0.545$	0.412	$+0.0004$
0.05	4.00	**0.50**	0.00	-0.423	0.748	-0.0992	$+0.597$	0.394	$+0.0006$
0.05	4.00	0.00	**-0.50**	-0.778	0.550	$+0.3628$	$+0.604$	0.442	$+0.0002$
0.05	4.00	0.00	**$+0.50$**	-0.455	0.449	$+0.1281$	$+0.325$	0.600	$+0.0083$

Table 7.2: Thresholds for one-dimensional α-particle temperature anisotropy instabilities for different values of the SRCH parameters. Any SRCH parameter value that is not its default is printed in **boldface**. The first row of this table corresponds to the case where all SRCH parameters were set to their default values, so these thresholds also appear in Table 7.1. All thresholds in this table correspond to the instability growth rate contour $\gamma_{\max} = 10^{-2}\,\Omega_p$ (see Equation 6.2) as fit to the model given in Equation 6.4.

SRCH Parameters			α-Particle Oblique Firehose			α-Particle Mirror		
$n_\alpha \,/\, n_p$	$T_{\parallel\alpha} \,/\, T_{\parallel p}$	ζ	a	b	β_0	a	b	β_0
0.05	4.00	0.00	−1.106	0.839	+0.2988	+1.515	0.467	+0.0069
0.10	4.00	0.00	−1.192	0.887	+0.1948	+1.364	0.506	+0.0045
0.20	4.00	0.00	−1.206	0.902	+0.2044	+1.271	0.537	+0.0022
0.05	**2.00**	0.00	−0.906	0.769	+0.7649	+1.787	0.391	+0.0145
0.05	**8.00**	0.00	−1.194	0.871	+0.1706	+1.425	0.489	+0.0055
0.05	4.00	**0.05**	−1.142	0.911	−0.1983	+1.556	0.443	+0.0104
0.05	4.00	**0.25**	−0.798	0.992	−0.3297	+1.138	0.567	+0.0011
0.05	4.00	**0.50**	−0.510	0.980	−0.1588	+0.685	0.684	−0.0021

Table 7.3: Thresholds for two-dimensional α-particle temperature anisotropy instabilities for different values of the SRCH parameters. The first row of this table corresponds to the case where all SRCH parameters were set to their default values, so these thresholds also appear in Table 7.1. All thresholds in this table correspond to the instability growth rate contour $\gamma_{\max} = 10^{-2}\,\Omega_p$ (see Equation 6.2) as fit to the model given in Equation 6.4. Each threshold was calculated assuming $\Delta v_{\parallel\alpha p} \,/\, c_A = 0.00$ since the EAN code cannot consider any other value for this parameter.

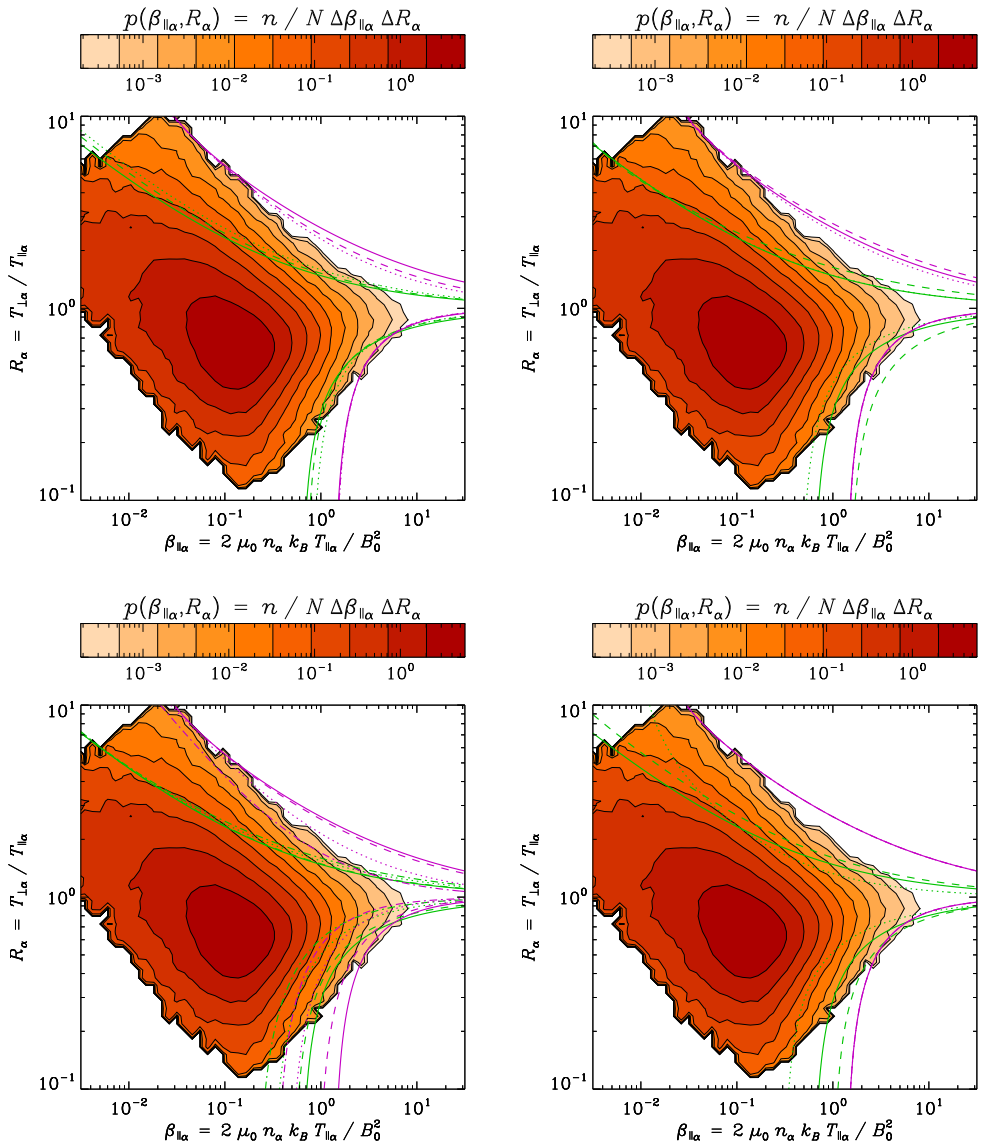

Figure 7.11.— Plots of $p(\beta_{\parallel\alpha}, R_\alpha)$ from *Wind*/FC ion spectra and the thresholds given in Tables 7.2 and 7.3 (green for one-dimensional, magenta for two-dimensional). The solid curves were generated with default values for all four `SRCH` parameters, but, for the others, one parameter had an alternative value. In the upper-left, $n_\alpha/n_p = 0.10$ (dashed) and 0.20 (dotted). In the upper-right, $T_\alpha / T_p = 2.00$ (dashed) and 8.00 (dotted). In the lower-left, $\zeta = 0.05$ (dashed), 0.25 (dotted), and 0.50 (dash-dotted). In the lower-right, $\Delta v_{\parallel\alpha p} / c_A = -0.50$ (dashed) and $+0.50$ (dotted).

low relative abundance of α-particles. For example, for fixed values of $(\beta_{\parallel p}, R_p)$, a slight change in $T_{\parallel\alpha} \,/\, T_{\parallel p}$ has relatively little impact on the total thermal energy density of the plasma; however, for fixed values of $(\beta_{\parallel\alpha}, R_\alpha)$, such a change would have a more significant effect.

Figure 7.11 shows that not all of the α-particle instabilities are affected the same way by variations in the value of a given parameter. As was the case for protons (see Figure 6.11), the one-dimensional α-particle instabilities are generally more sensitive to the parameter values than their two-dimensional counterparts. The two-dimensional α-particle instability thresholds in Figure 7.11, for the most part, show relatively little dependence on the `SRCH` parameters, but ζ (lower-left plot) provides a notable exception. Even a small increase in the value of ζ significantly pulls the oblique firehose and mirror instability thresholds closer to isotropy (i.e., toward $R_\alpha = 1$). In fact, a value of $\zeta = 0.25$ or 0.50 produces thresholds for the two-dimensional instabilities that are in significantly better alignment with the observations than those generated using the default value $\zeta = 0.00$. Given the sensitivity of these instabilities to the value of ζ, this improved agreement between theory and observations is not surprising: Figure 4.10 shows that the observations themselves are more consistent with a value of $\zeta = 0.25$ than with one of $\zeta = 0.00$.

Chapter 8

Proton Temperature in Unstable Plasma

This chapter extends the analysis of Chapter 6 to investigate more closely the connection between proton temperature anisotropy instabilities and heat flow in the solar wind. Section 8.1 motivates the connection between proton temperature anisotropy instabilities and anisotropic heating and cooling processes. Variations in proton temperature (both the scalar temperature and the temperature components) over the $(\beta_{\parallel p}, R_p)$-plane are shown and discussed in Section 8.2. Section 8.3 presents the results of a novel analysis technique which explores trends in observed proton temperature versus instability growth rate (as calculated from linear Vlasov theory).

8.1 Origins of Ion Temperature Anisotropy

Figure 6.10 shows the distribution of *Wind*/FC ion spectra extending up to and slightly beyond the thresholds of proton temperature anisotropy instabilities. In order for the protons to remain in this marginally unstable state (at least long enough to be observed), ongoing processes must be acting in the solar wind to counteract the isotropizing effects of the instabilities. The most obvious candidates are anisotropic heating and cooling processes (see Section 1.2.2) since they directly affect the temperature components.

Anisotropy-driven instabilities themselves are not understood to appreciably heat or cool the plasma (see, e.g., Southwood & Kivelson, 1993). Since the free energy that drives these instabilities is associated with $R_p \neq 1$, their ultimate effect should be to bring $T_{\perp p}$ and $T_{\parallel p}$ closer to equality while conserving T_p. Thus, comparing the temperatures of stable and unstable plasma gauges the relative roles of anisotropic heating and cooling in the plasma prior to the instability's onset. If T_p is elevated in marginally unstable plasma, anisotropic heating was more active than cooling; if T_p is depressed, anisotropic cooling was more active.

8.2 Temperature Trends over the $(\beta_{\parallel p}, R_p)$-Plane

One assessment of the connection between proton temperature and the actions of proton temperature anisotropy instabilities is carried out by examining variations in T_p, $T_{\perp p}$, and $T_{\parallel p}$ across the $(\beta_{\parallel p}, R_p)$-plane. A plot of $T_p(\beta_{\parallel p}, R_p)$ is shown in Figure 8.1, while Figure 8.2 shows plots of $T_{\perp p}(\beta_{\parallel p}, R_p)$ (left) and $T_{\parallel p}(\beta_{\parallel p}, R_p)$ (right). Each of these plots was generated by dividing the selected *Wind*/FC ion spectra (see Chapter 4) into a 50×50 grid of logarithmically-spaced bins in the $(\beta_{\parallel p}, R_p)$-plane. The number of observations, n, in each

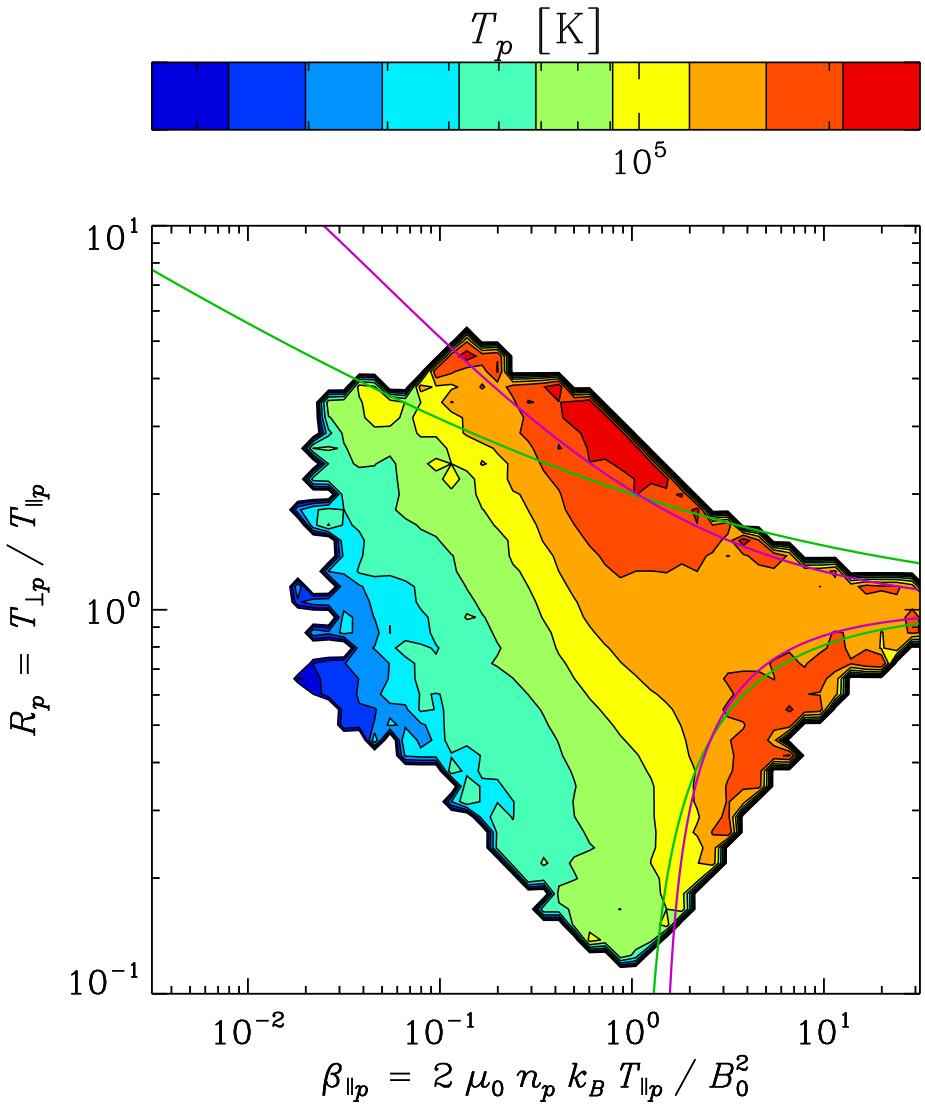

Figure 8.1.— Plot of proton scalar temperature, T_p, over the $(\beta_{\parallel p}, R_p)$-plane. The overlaid curves indicate the theoretical instability thresholds listed in Table 6.2; the thresholds of the one-dimensional (i.e., parallel firehose and cyclotron) instabilities are shown in green, and those of the two-dimensional (i.e., oblique firehose and mirror) instabilities are shown in magenta. The regions where the median T_p is highest occur near or beyond these thresholds.

bin was calculated, and bins with $n < 16$ were discarded. Each plot shows, for each of its remaining bins, the median value of the parameter listed in the plot's title. The grid in each plot was interpolated into contours, and the default proton instability thresholds specified in Table 6.2 were overlaid (with those for the one-dimensional instabilities shown in green and those for the two-dimensional instabilities shown in magenta).

The plot of $T_p(\beta_{\parallel p}, R_p)$ in Figure 8.1 shows a tendency for T_p to grow with $\beta_{\parallel p}$, which is expected since $\beta_{\parallel p} \propto T_{\parallel p}$ (see Equation 1.9). However, even beyond this overall trend, the highest T_p-values occur in two regions: one near the mirror instability threshold and the other near the firehose instability thresholds. Even at high-$\beta_{\parallel p}$, these regions have median T_p-values that are significantly higher than those in the region between them (i.e., near $R_p = 1$), which is consistent with an earlier suggestion of this effect that was identified by Liu et al. (2006). Additionally, the high-T_p region at $R_p > 1$ is more aligned with the mirror instability threshold than with the cyclotron instability threshold, which provides further evidence that (at 1 AU) the mirror instability is more active in limiting $R_p > 1$. Unfortunately, the similarity of the thresholds of the two firehose instabilities allows no such comparison between them.

The plots of $T_{\perp p}(\beta_{\parallel p}, R_p)$ and $T_{\parallel p}(\beta_{\parallel p}, R_p)$ in Figure 8.2, when considered along with the plot of $T_p(\beta_{\parallel p}, R_p)$ in Figure 8.1, indicate that the enhanced T_p near the mirror instability threshold is almost entirely due to increased $T_{\perp p}$ and that the enhanced T_p near the firehose instability thresholds is almost entirely due to increased $T_{\parallel p}$. Conceivably, deviations in R_p from unity could stem from a decrease in one of the two temperature components. However, the plots in Figure 8.2 show no strong evidence that $T_{\perp p}$ is depressed near the firehose instability thresholds or that $T_{\parallel p}$ is depressed near the mirror instability threshold.

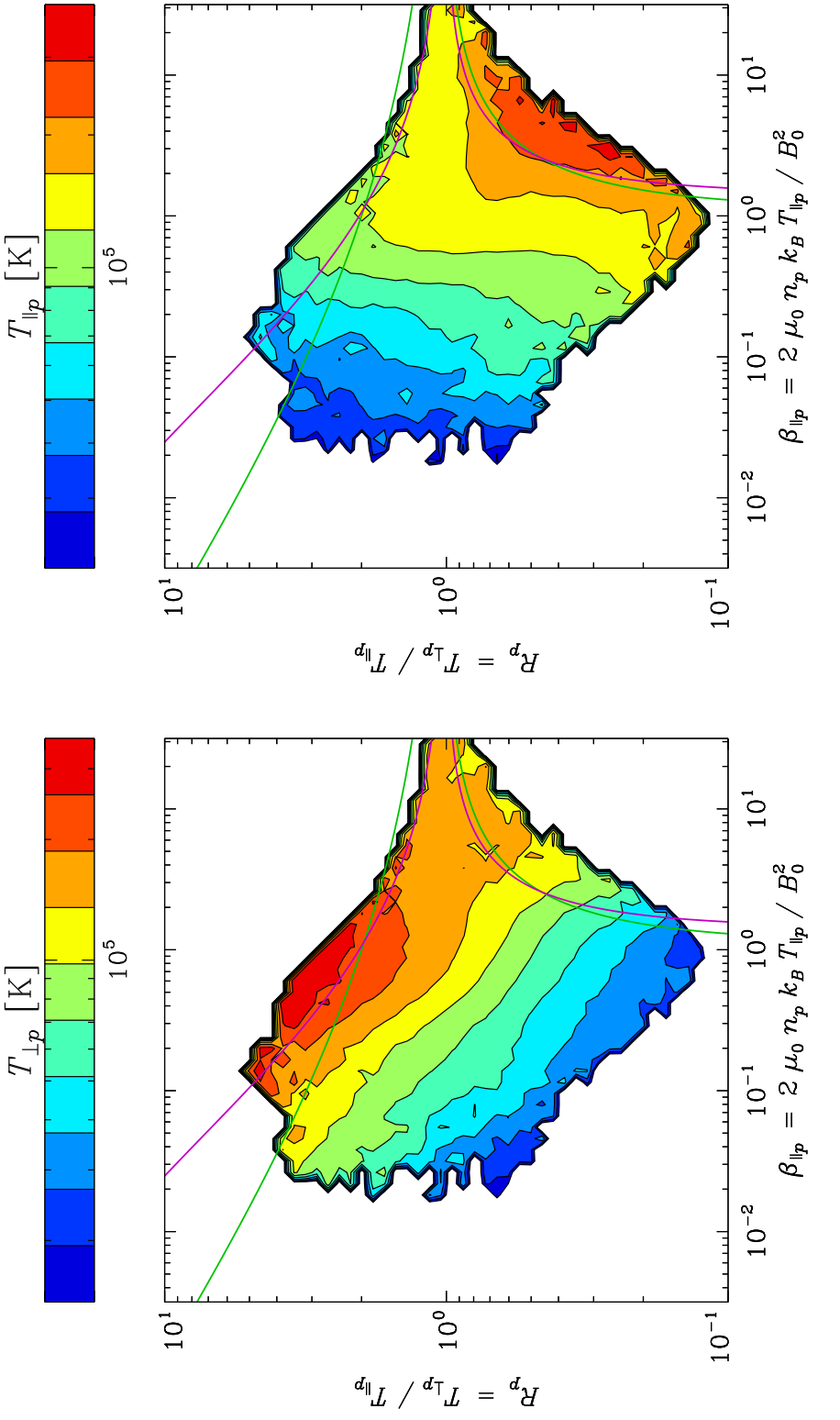

Figure 8.2.— Plots of proton temperature components, $T_{\perp p}$ (left) and $T_{\parallel p}$, (right) over the $(\beta_{\parallel p}, R_p)$-plane. The overlaid curves indicate the theoretical instability thresholds listed in Table 6.2; those of the one-dimensional (i.e., parallel firehose and cyclotron) instabilities are shown in green while those of the two-dimensional (i.e., oblique firehose and mirror) instabilities are shown in magenta.

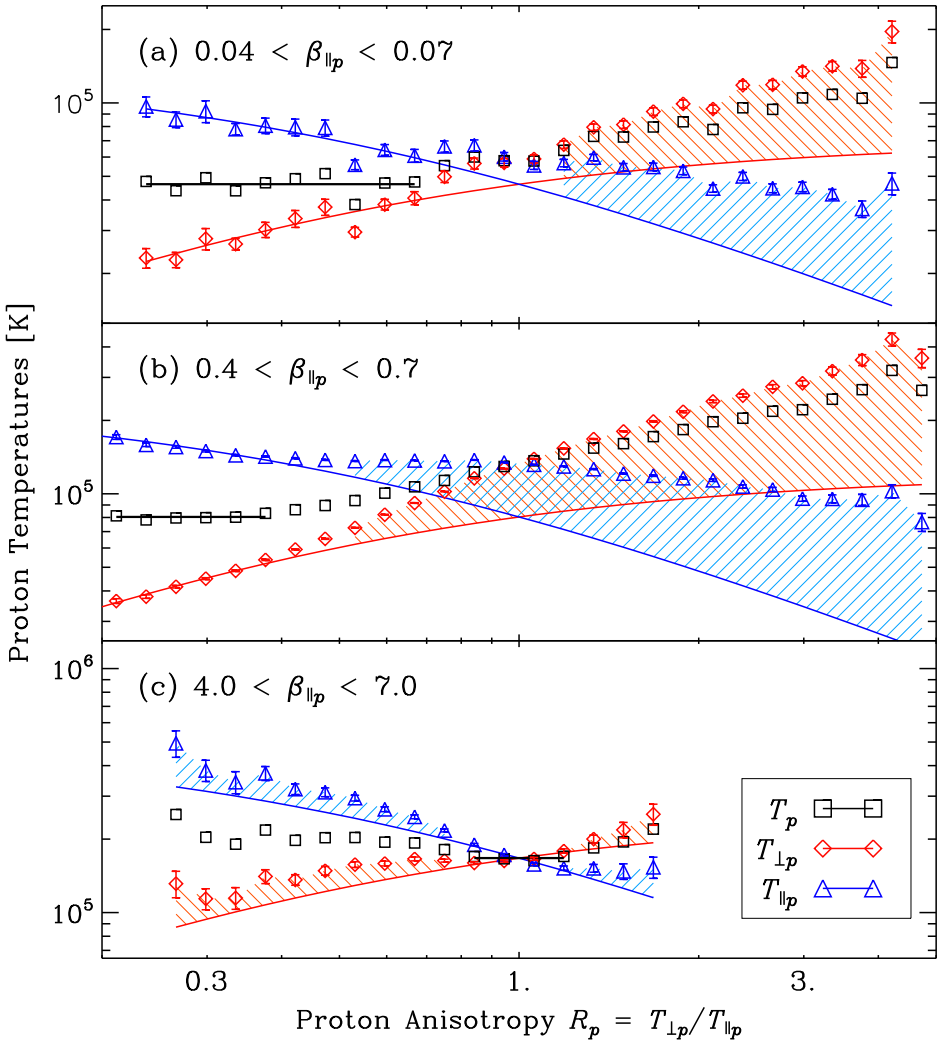

Figure 8.3.— Plots of mean T_p (black squares), $T_{\perp p}$ (red diamonds), and $T_{\|p}$ (blue triangles) versus R_p for three ranges of $\beta_{\|p}$: (a) 0.04 to 0.07, (b) 0.4 to 0.7, and (c) 4.0 to 7.0. For $T_{\perp p}$ and $T_{\|p}$, error bars indicate the uncertainties in the mean values. The solid black line in each plot indicates the mean T_p value over the range of R_p-values that it spans. The solid red and blue curves show the projected values of $T_{\perp p}$ and $T_{\|p}$ if T_p equaled this mean value for all R_p. Shading indicates enhancements in the observed $T_{\perp p}$- and $T_{\|p}$-values beyond these extrapolations.

For a more detailed perspective on these temperature enhancements, Figure 8.3 shows the mean values of T_p, $T_{\perp p}$, and $T_{\parallel p}$ as functions of R_p for the observations in each of three representative ranges of $\beta_{\parallel p}$: (a) 0.04 to 0.07, (b) 0.4 to 0.7, and (c) 4.0 to 7.0. Curiously, each plot has a domain of R_p-values for which T_p is approximately constant; a black line indicates each of these domains and the mean T_p-value over it. The colored curves show the expected trends in $T_{\perp p}$ and $T_{\parallel p}$ if T_p had the value indicated by the black line for all R_p. The shaded regions indicate the departures of the data from this simple model.

All three plots in Figure 8.3 show a strong enhancement in T_p and $T_{\perp p}$ for $R_p \gtrsim 1$, which is consistent with enhancements seen near the mirror instability threshold in Figures 8.1 and 8.2. A similar enhancement in $T_{\parallel p}$ for $R_p \lesssim 1$ is only apparent in Figure 8.3(c) because the firehose instabilities are only active for $\beta_{\parallel p} \gtrsim 1$. Curiously, though, Figure 8.3 also suggests that, whenever one temperature component is enhanced beyond the expected trend for constant-T_p, the other is as well. Interpreting this effect is complicated by Figure 8.2, which suggests that only one temperature component is appreciably enhanced near either threshold. Potentially, then, the simultaneous enhancement of both temperature components in Figure 8.3 results simply from the breakdown of the constant-T_p model, which itself lacks any theoretical or even intuitive justification. However, the concurrent excess in both temperature components could possibly be a result of the instabilities themselves. The ultimate effect of a proton temperature anisotropy instability is to drive R_p closer to unity by redistributing thermal energy so that $T_{\perp p}$ and $T_{\parallel p}$ become closer in value. Therefore, the simultaneous enhancement of both temperature components in Figure 8.3 could be an indication of the initial stages of this process.

8.3 Temperature Trends With Instability Growth Rate

This section focuses on more quantitatively comparing the relative effectiveness of the mirror and cyclotron instabilities at limiting $R_p > 1$. While in principle a similar comparison could be made for $R_p < 1$ of the parallel and oblique firehose instabilities, their theoretical trends in growth rate (see Figures 6.6 and 6.8) are too similar for the proceeding method.

Figure 6.10 shows the probability distribution of $(\beta_{\parallel p}, R_p)$-values from the selected *Wind*/FC ion spectra (see Chapter 4) with the default thresholds for the proton temperature anisotropy instabilities (see Table 6.2) overlaid. Like similar plots by Hellinger et al. (2006) and Bale et al. (2009), the distribution of observations seems to be more aligned with the threshold of the mirror instability than with that of the cyclotron instability, which has been interpreted as evidence that the former is more active in limiting $R_p > 1$ (despite setting a weaker limit than the latter for $\beta_{\parallel p} \lesssim 1$.). However, this analysis is quite subjective. Can a more rigorous and quantitative assessment be made?

As described in Chapter 6, all of the instability thresholds in this study were derived by calculating the instability growth rate, $\gamma_{\max}$, over a fine grid of $(\beta_{\parallel j}, R_j)$-values (where j indicates the instability's driving species). The results of this analysis for the proton cyclotron and mirror instabilities, for the default values of the `SRCH` parameters (see Table 6.1), are shown respectively in Figures 6.7 and 6.9. Deriving the thresholds of these instabilities (which are listed in Table 6.2) corresponds to simply extracting and fitting the contours of constant $\gamma_{\max} = 10^{-2}\,\Omega_p$ (see Equation 6.2). However, this analysis is somewhat wasteful in that it discards most of the information in these plots.

This section describes a more advanced method for using the computed $\gamma_{\max}(\beta_{\parallel p}, R_p)$-

values to interpret the *Wind*/FC proton data. In particular, the values of $\gamma_{\max}(\beta_{\parallel p}, R_p)$ were interpolated so that a $\gamma_{\max}$-value could be individually assigned to each spectrum based on its specific values of $\beta_{\parallel p}$ and R_p. This procedure was performed separately for the proton cyclotron and mirror instabilities and used the $\gamma_{\max}$-values shown respectively in Figures 6.7 and 6.9. This unique and entirely new analysis more closely integrated the theoretical and empirical data so that the effects of instabilities on the plasma could be more directly explored.

The plots in Figure 8.4 show T_p (top), $T_{\perp p}$ (middle), $T_{\parallel p}$ (bottom) as functions of $\gamma_{\max}$ for the cyclotron (left) and mirror (right) instabilities. The plots in this figure were made using only the *Wind*/FC ion spectra with $0.4 < \beta_{\parallel p} < 0.7$, which is the same subset of data used for Figure 8.3(b). For each plot, the spectra were divided into logarithmically-spaced $\gamma_{\max}$-bins. The mean temperature- and $\gamma_{\max}$-values of the bins are indicated with diamonds, and error bars show the uncertainties in these mean values.

For each instability, Figure 8.4 shows that T_p and $T_{\perp p}$ each has a strong, positive correlation with $\gamma_{\max}$ but that $T_{\parallel p}$ is largely independent of (or perhaps is somewhat negatively correlated with) $\gamma_{\max}$. These trends are consistent with the temperature enhancements seen in Figures 8.1 and 8.2: near the cyclotron and mirror instability thresholds, T_p and $T_{\perp p}$ are significantly elevated, and $T_{\parallel p}$ seems mostly unaffected by proximity to these thresholds. However, the analysis shown in Figure 8.4 carries the advantage of actually quantifying these effects.

Each plot in Figure 8.4 is labeled with the equation for the best linear fit of the data therein, and this fit is also plotted along with the data. Interestingly, the trend in each plot is well-fit by this simple, linear model. However, even more remarkably, the fitted slopes

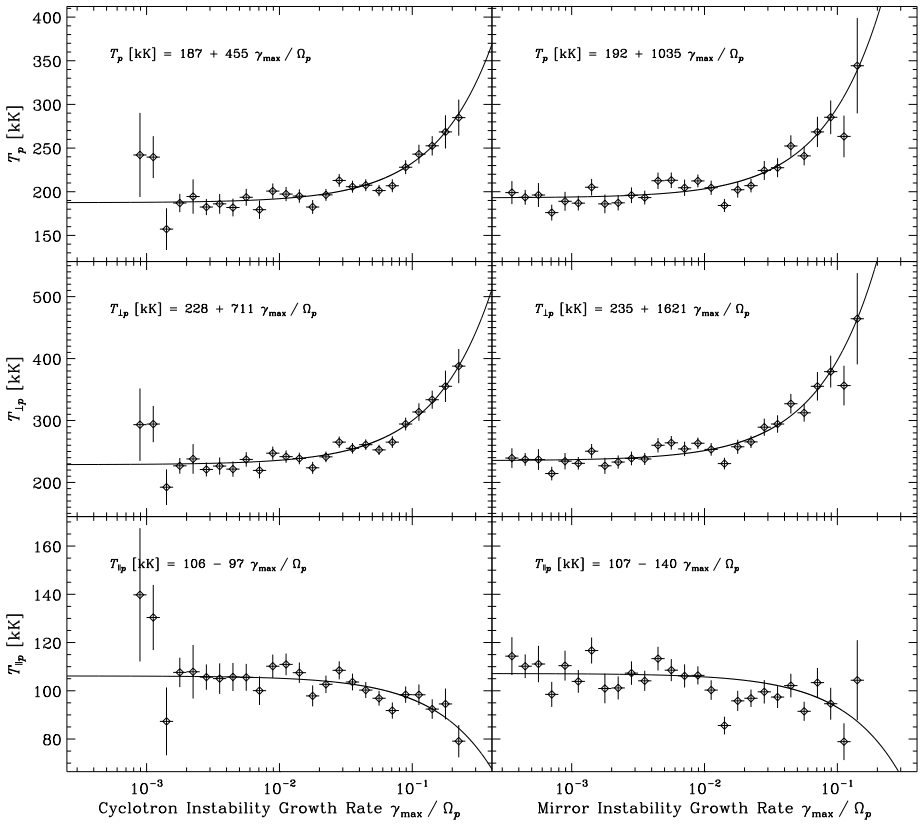

Figure 8.4.— Plots, for $0.4 < \beta_{\parallel p} < 0.7$, of T_p (top), $T_{\perp p}$ (middle), and $T_{\parallel p}$ (bottom) as functions of $\gamma_{\max}$ for the proton cyclotron (left) and mirror (right) instabilities. The values of $\beta_{\parallel p}$ and of the proton temperatures are empirical and taken from the *Wind*/FC ion spectra (see Chapter 4); conversely, the values of $\gamma_{\max}$ are theoretical and taken from the same calculations used to produce Figures 6.7 and 6.9. For each instability, interpolation was used to assign a $\gamma_{\max}$-value to each *Wind*/FC ion spectrum. These spectra were then sorted into logarithmically-spaced $\gamma_{\max}$-bins, and the diamonds in the plots indicate the median temperature- and $\gamma_{\max}$-values of these bins. Each plot shows the equation and curve of the best linear fit of the data therein.

of $T_p(\gamma_{\max})$ and $T_{\perp p}(\gamma_{\max})$ are each more than twice as high for the mirror instability than the cyclotron instability. In the above discussion of Figures 8.1 and 8.2, it is noted that the contours of $T_p(\beta_{\parallel p}, R_p)$ and $T_{\perp p}(\beta_{\parallel p}, R_p)$ qualitatively seem to be more aligned with the threshold of the mirror instability than with that of the cyclotron instability. The analysis in Figure 8.4 shows this quantitatively and thereby lends new credence to the interpretation that the mirror instability is more active than the cyclotron instability in limiting the values of $R_p > 1$ observed in the solar wind.

Chapter 9

Conclusions and Discussion

This chapter concludes this dissertation. Section 9.1 overviews the most significant results from the analysis presented in the preceding chapters. Section 9.2 contains comments on the larger implications of these results and on possible ways in which this work could be extended.

9.1 Summary of Results

For this thesis project, both observational and theoretical methods were used to explore how ion temperature anisotropy instabilities affect the evolution of plasma in the heliosphere. The *Wind* spacecraft's Faraday cups were used to provide in situ measurements of protons and α-particles in the solar wind. The code used to extract ion bulk parameters from these measurements was fully revised from an earlier version to increase its reliability and to improve the quality of its data output. In particular, this version was found to produce significantly more accurate values for the temperature anisotropy, $R_j = T_{\perp j} \, / \, T_{\parallel j}$, of both

protons and α-particles ($j = p$ and α, respectively). Additional code, based on linear Vlasov theory, was used to predict thresholds in the $(\beta_{\parallel j}, R_j)$-plane for both the proton and α-particle temperature anisotropy instabilities under a variety of plasma conditions.

This study's combined observational and theoretical analysis has provided the most conclusive evidence to date that kinetic microinstabilities limit the range of α-particle temperature anisotropy observed in the solar wind. Similar studies have previously shown this to be the case for protons, the dominant ion in the solar wind, but the ability of a low-abundance ion, like α-particles, to drive temperature anisotropy instabilities had not been demonstrated. Nevertheless, the theoretical work in this thesis project showed that a sufficiently anisotropic population of α-particles can indeed lead to unstable plasma modes. Furthermore, this study's analysis of *Wind*/FC data found that the distribution of R_α-values observed in interplanetary space is consistent with the limits predicted for these instabilities.

In calculating instability thresholds from linear Vlasov theory, different values for four basic plasma parameters were considered (see Table 6.1). For the most part, the thresholds of the proton instabilities were not particularly sensitive to these parameters, but the α-particle instability thresholds showed considerably more variability. The interspecies anisotropy coupling factor, ζ, was of particular interest because the use of more-realistic ζ values in calculations of α-particle thresholds was found to dramatically improve their agreement with the observed $(\beta_{\parallel\alpha}, R_\alpha)$-values.

This study, like those of Hellinger et al. (2006) and Bale et al. (2009), found that observations of solar wind protons were more consistent with the limits imposed by the two-dimensional (i.e., mirror and oblique firehose) instabilities than those imposed by the one-dimensional (i.e., cyclotron and parallel firehose) instabilities. Curiously, this holds

true even at $\beta_{\|p}$-values for which a one-dimensional instability places the stricter limit on R_p. The analysis in this thesis project found the same phenomenon with the α-particles, for which the differences between the one- and two-dimensional thresholds are even more dramatic. The cause of this apparent inconsistency remains a mystery. However, two-dimensional instabilities are associated with non-propagating modes, which Bale et al. (2009) has speculated could make them more efficient at scattering particles in phase space despite potentially lower growth rates.

In an extended analysis of the proton data, this study explored trends in proton temperature over the $(\beta_{\|p}, R_p)$-plane. The scalar temperature was found to be significantly enhanced in marginally unstable plasma relative to plasma with isotropic protons (i.e., $R_p = 1$). For $R_p > 1$, almost all of this temperature enhancement seemed to be in the perpendicular component: the parallel component appeared to be unaffected or perhaps weakly depressed. Likewise, for $R_p < 1$, the parallel component was found to be enhanced and the perpendicular component to be either unchanged or slightly decreased. These results strongly suggest that the values of both $R_p > 1$ and $R_p < 1$ observed in the solar wind are more the products of anisotropic heating rather than cooling.

The enhancements seen in scalar and perpendicular temperature for $R_p > 1$ were quantitatively confirmed by a novel technique that directly combined the observed $(\beta_{\|p}, R_p)$-values with the calculated growth rates for the cyclotron and mirror instabilities. This analysis also indicated that the temperature trends were remarkably better aligned with the growth rate of the mirror versus the cyclotron instability and thus provided further evidence that the former is more active in limiting $R_p > 1$.

9.2 Future Paths and Applications

Though α-particle temperature anisotropy instabilities have not received much attention in the literature, this study found strong evidence that they limit the observed distribution of R_α-values in the solar wind. This result has implications for the study of minor ions (e.g., carbon and oxygen) throughout the heliosphere. Could the temperature anisotropies of these even-less-abundant species be similarly limited by instabilities? Minor ions are preferentially and anisotropically heated, and spectroscopic methods have established that they can typically achieve temperature anisotropies of 10 to 20 in the solar corona (Cranmer et al., 2008). However, are these remotely-measured anisotropy values an accurate indication of the total heating of coronal plasma or are they simply the limits imposed by anisotropy-driven instabilities? If a minor ion species is demonstrated to be able to drive such an instability, it could significantly impact how observations of astrophysical plasmas (both inside and outside of the solar system) are interpreted. An extension of this thesis project's linear Vlasov analysis to include minor ions may help to reveal the complex interplay among different particle species in such plasmas.

This study's analysis of proton temperature trends strongly suggests that anisotropic heating is more responsible than cooling for producing the extreme proton temperature anisotropies (both $R_p < 1$ and $R_p > 1$) that ultimately lead to the onset of the associated instabilities. While, in principle, anisotropic cooling processes could drive R_p far enough from unity to trigger an instability, only weak evidence was found that either the perpendicular or the parallel component of proton temperature is depressed in unstable plasma. This result was particularly surprising for $R_p < 1$ since conventional wisdom has held that perpendicular cooling from CGL double adiabatic expansion is a major factor in driving

$R_p < 1$ (Chew et al., 1956; Matteini et al., 2007). Instead, parallel heating seems to have a more significant role in exciting the proton firehose instabilities. This finding motivates more detailed studies of parallel heating mechanisms, which have received significantly less attention in the literature than their perpendicular counterparts. These results could have important implications for the study of the solar wind as well as the expanding, magnetized plasmas that are found in other astrophysical environments.

In principle, these methods for studying trends in proton temperature over the $(\beta_{\parallel p}, R_p)$-plane could also be used to consider trends in α-particle temperature over the $(\beta_{\parallel \alpha}, R_\alpha)$-plane, but the lower accuracy of the α-particle data could pose practical problems. Assuming that these complications could be overcome, the natural expectation would be that the α-particle temperature trends would mimic those for proton temperature. However, this may not be the case since heating and cooling processes are known to act with different efficiencies on different ions species.

For this thesis project, trends in proton temperature in plasma with $R_p > 1$ were also studied with an entirely new technique in which theoretical values for the mirror and cyclotron instability growth rates were assigned to each *Wind*/FC ion spectrum. This analysis uniquely combined theoretical and observational results and, in doing so, provided a quantitative assessment of trends in proton temperature. The scalar and perpendicular temperatures were each shown to be positively and linearly correlated with the growth rate of either instability, but the trends in temperature versus growth rate were found to be twice as steep for the mirror instability. This result quantitatively indicates that the temperature enhancements in the $(\beta_{\parallel p}, R_p)$-plane are more aligned with the mirror instability's growth-rate contours and therefore that the mirror instability has a stronger impact on the evolution of the plasma.

Nevertheless, this merger of theoretical and observational results has raised several important questions. First, why are the trends in temperature versus growth rate so remarkably linear? Despite the success of this model, there is no clear theoretical justification for it. Second, how are the fit parameters of this model related to the evolution of the plasma? For example, the slope is presumably dependent on the rate of perpendicular heating and the efficiency with which the instability isotropizes temperature. Investigating these questions could provide important insights into the interaction between these two processes in astrophysical plasmas.

In this thesis project, theoretical instability growth rates were assigned to each *Wind*/FC ion spectrum via interpolation over the $(\beta_{\|p}, R_p)$-plane. Of course, this limited the analysis to fixed values for the remaining plasma parameters. Conceivably, though, this analysis could be significantly improved by running linear Vlasov code for each spectrum individually by using its particular set of values for the fit parameters. While running the code on each spectrum would likely prove to be very computationally intensive, this approach should produce better results because the computed values of growth rate would more accurately reflect the measured plasma conditions. Additionally, this method removes the need to identify a single driving species or even to distinguish among different types of instabilities (e.g., temperature anisotropy versus drift instabilities) since the use of the full set of measured parameters automatically accounts for these different effects.

References

Abetti, G. 1962, *Solar Research* (Macmillan, New York, NY)

Acuña, M. H. et al. 1995, *Spa. Sci. Rev.*, **71**, 5

Alexander, D. 2005, *The Sun* (Greenwood Press, Santa Barbara, CA)

Asbridge, J. R. et al. 1974, *Solar Phys.*, **37**, 451

Bale, S. D. et al. 2009, *Phys. Rev. Lett.*, **103**, 211101

Baumjohann, W. & Treumann, R. A. 1997, *Basic Space Plasma Physics* (Imperial College Press, London, UK)

Bevington, P. R. & Robinson, D. K. 2003, *Data Reduction and Error Analysis for the Physical Sciences* (McGraw-Hill Higher Education, Boston, MA)

Bhatnagar, A. & Livingston, W. 2005, *Fundamentals of Solar Astronomy* (World Scientific, New Jersey)

Biermann, L. 1951, *Z. Astrophys.*, **29**, 274

Boteler, D. H. 2006, *Adv. Space Res.*, **38**, 159

Bureau international des poids et mesures 2006, *Le Système international d'unités*, 8$^{\text{th}}$ edn. (Sèvres, France)

Burlaga, L. F. 1995, *Interplanetary Magnetohydrodynamics* (Oxford University Press, New York, NY)

Carrington, R. C. 1859, *Mon. Not. R. Astron. Soc.*, **20**, 13

Chandran, B. D. G. et al. 2010, *Astrophys. J.*, **720**, 503

—. 2011, *Astrophys. J.*, **743**, 197

Chapman, S. 1957, *Smithsonian Contrib. Astrophys.*, **2**, 1

Chew, G. F. et al. 1956, *Proc. R. Soc. A*, **236**, 112

Clack, D. et al. 2004, *Geophys. Res. Lett.*, **31**, 6812

Cowling, T. G. 1957, *Magnetohydrodynamics* (Interscience Publishers, New York, NY)

Cranmer, S. R. 2001, *J. Geophys. Research*, **106**, 24937

Cranmer, S. R. et al. 2008, *Astrophys. J.*, **678**, 1480

Feldman, W. C. et al. 1973, *J. Geophys. Res.*, **78**, 2017

Gary, S. P. 1993, *Theory of Space Plasma Microinstabilities* (Cambridge University Press, Cambridge, UK)

Gary, S. P. & Winske, D. 1993, *J. Geophys. Res.*, **98**, 9171

Gary, S. P. et al. 1976, *J. Geophys. Res.*, **81**, 1241

—. 1994, *J. Geophys. Res.*, **99**, 5903

—. 1998, *J. Geophys. Res.*, **103**, 14567

—. 2001, *Geophys. Res. Lett.*, **28**, 2759

—. 2003, *J. Geophys. Res.*, **108**, 1068

Golub, L. & Pasachoff, J. M. 1997, *The Solar Corona* (Cambridge University Press, Cambridge, UK)

Harten, R. & Clark, K. 1995, *Spa. Sci. Rev.*, **71**, 23

Heidarzadeh, T. 2008, *A History of Physical Theories of Comets, From Aristotle to Whipple* (Springer Science + Business Media)

Hellinger, P. & Trávníček, P. M. 2011, *J. Geophys. Res. (Spa. Phys.)*, **116**, 11101

Hellinger, P. et al. 2005, *J. Geophys. Res.*, **110**, 12109

—. 2006, *Geophys. Res. Lett.*, **33**, 9101

Hodgson, R. 1859, *Mon. Not. R. Astron. Soc.*, **20**, 15

Hollweg, J. V. & Isenberg, P. A. 2002, *J. Geophys. Res.*, **107**, 1147

Hundhausen, A. J. 1972, *Coronal Expansion and Solar Wind* (Springer-Verlag, Berlin, Germany)

Isenberg, P. A. & Hollweg, J. V. 1983, *J. Geophys. Res.*, **88**, 3923

Isenberg, P. A. & Vasquez, B. J. 2007, *Astrophys. J.*, **668**, 546

Kasper, J. C. 2002, PhD thesis, Massachusetts Institute of Technology

Kasper, J. C. et al. 2002, *Geophys. Res. Lett.*, **29**, 20

—. 2006, *J. Geophys. Res. (Spa. Phys.)*, **111**, 3105

—. 2007, *Astrophys. J.*, **660**, 901

—. 2008, *Phys. Rev. Lett.*, **101**, 261103

Kepler, J. 1604, *Astronomiæ Pars Optica* (Frankfurt, Germany)

—. 1619, *De Cometis Libelli Tres* (Augsburg, Germany)

—. 2000, *Optics: Paralipomena to Witelo & Optical Part of Astronomy*, trans. W. H. Donahue (Green Lion Press, Santa Fe, NM)

Kulsrud, R. M. 1983, "MHD Description of Plasma" in *Basic Plasma Physics I* (North-Holland Publishing Company), 115

Lacombe, C. et al. 1995, *Ann. Geophys.*, **13**, 343

Lepping, R. P. et al. 1995, *Spa. Sci. Rev.*, **71**, 207

Liu, Y. et al. 2006, *J. Geophys. Res. (Spa. Phys.)*, **111**, 1102

Liu, Y. C.-M. et al. 2007, *J. Geophys. Res. (Spa. Phys.)*, **112**, 7217

Lu, Q. M. et al. 2006, *J. Geophys. Res. (Spa. Phys.)*, **111**, 9101

Markovskii, S. A. & Hollweg, J. V. 2004, *Astrophys. J.*, **609**, 1112

Markwardt, C. B. 2009, in *Astronomical Society of the Pacific Conference Series*, Vol. 411, *Astronomical Data Analysis Software and Systems XVIII*, 251

Marquardt, D. W. 1963, *SIAM J. Appl. Math.*, **11**, 431

Marsch, E. 1991, "Kinetic Physics of the Solar Wind Plasma" in *Physics of the Inner Heliosphere II* (Springer-Verlag), 45

Marsch, E. & Richter, A. K. 1984, *J. Geophys. Res.*, **89**, 6599

Marsch, E. & Tu, C.-Y. 2001, *J. Geophys. Res.*, **106**, 8357

Marsch, E. et al. 1982, *J. Geophys. Res.*, **87**, 52

Matteini, L. et al. 2006, *J. Geophys. Res. (Spa. Phys.)*, **111**, 10101

—. 2007, *Geophys. Res. Lett.*, **34**, 20105

—. 2011, *Spa. Sci. Rev.*, 128

McComas, D. J. et al. 1998, *Spa. Sci. Rev.*, **86**, 563

McInnes, C. R. 1999, *Solar Sailing: Technology, Dynamics and Mission Applications* (Springer, London, UK)

Mecheri, R. & Marsch, E. 2008, *Astron. and Astrophys.*, **481**, 853

Merka, J. et al. 2003, *J. Geophys. Res. (Spa. Phys.)*, **108**, 1077

Mohr, P. J. et al. 2008, *Rev. Mod. Phys.*, **80**, 633

Moré, J. J. et al. 1980, *User Guide for MINPACK-1* (Argonne National Laboratory)

Motschmann, U. & Glassmeier, K.-H. 1993, *J. Geophys. Res.*, **98**, 20977

Neugebauer, M. & Snyder, C. W. 1962, *Science*, **138**, 1095

Ogilvie, K. W. et al. 1995, *Spa. Sci. Rev.*, **71**, 55

Olbers, H. W. M. 1812, *Zachs Monatl. Corresp.*, **25**, 3

Ovid. 8, *Metamorphoses*

—. 1956, *Metamorphoses*, trans. F. J. Miller (William Heinemann, London, UK)

Oxford English Dictionary. March 2012, online

Parker, E. N. 1958, *Astrophys. J.*, **128**, 664

Plutarch. c. 90, "*De facie quæ in orbe lunæ apparet* (Περὶ τοῦ ἐμφαινομένου προσώπου τῷ κύκλῳ τῆς σελήνης)" in *Moralia*

—. 1957, "Concerning the Face Which Appears in the Orb of the Moon" in *Moralia*, Vol. 12, trans. H. Cherniss (Harvard University Press, Cambridge, MA)

Proctor, R. A. 1884, *The Universe of Suns and Other Science Gleanings* (R. Worthington)

Prölss, G. W. 2004, *Physics of the Earth's Space Environment* (Springer-Verlag, Berlin, Germany)

Quataert, E. 1998, *Astrophys. J.*, **500**, 978

Russell, C. T. 1971, *Cosmic Electrodyn.*, **2**, 184

Sahraoui, F. et al. 2009, *Phys. Rev. Lett.*, **102**, 231102

—. 2010, *Phys. Rev. Lett.*, **105**, 131101

Schekochihin, A. A. & Cowley, S. C. 2006, *Phys. Plasmas*, **13**, 56501

Schekochihin, A. A. et al. 2009, *Astrophys. J. Supp.*, **182**, 310

Schwartz, S. J. 1980, *Rev. Geophys. & Spa. Phys.*, **18**, 313

Schwenn, R. 1990, "Large-Scale Structure of the Interplanetary Medium" in *Physics of the Inner Heliosphere I* (Springer-Verlag), 99

Sharma, P. et al. 2006, *Astrophys. J.*, **637**, 952

Southwood, D. J. & Kivelson, M. G. 1993, *J. Geophys. Res.*, **98**, 9181

Spitzer, L. 1956, *Physics of Fully Ionized Gases* (Interscience Publishers, New York, NY)

Stewart, B. 1861, *R. Soc. London Phil. Trans. (Ser. I)*, **151**, 423

Stix, T. H. 1992, *Waves in Plasmas* (American Institute of Physics, New York, NY)

Taylor, J. R. 1997, *An Introduction to Error Analysis* (University Science Books, Sausalito, CA)

The New York Times. 3 September 1859, "Aurora Australis: Magnificent Display on Friday Morning"

Thompson, A. & Taylor, B. N. 2008, *Guide for the Use of the International System of Units (SI)*, NIST Special Publication 811, National Institute of Standards and Technology, Gaithersburg, MD

Tiersch, H. & Notni, P. 1989, *Astron. Nachr.*, **310**, 67

Treumann, R. A. & Baumjohann, W. 1997, *Advanced Space Plasma Physics* (Imperial College Press, London, UK)

Velli, M. 2001, *Astrophys. and Spa. Sci.*, **277**, 157

Zirin, H. 1966, *The Solar Atmosphere* (Blaisdell Publishing, Waltham, MA)

Appendix A

Summary of Units and Notation

The International System of Units (*Le Système international d'unités*) (*Bureau international des poids et mesures*, 2006; Thompson & Taylor, 2008) is exclusively employed in this dissertation. In keeping with the *de facto* standards in space plasma physics, speeds are generally specified in units of km/s, number densities in units of cm^{-3}, and magnetic field strength and component in units of nT.

In this dissertation, the names of programs, programming languages, and software packages appear in a `monospaced` font. Programs written in `IDL` have their names appear in lower-case letters, but, following historical convention, those written in `FORTRAN` have their names fully capitalized.

A vector quantity appears in **boldface** and its magnitude in *italics*. The projection and component of a vector along a given axis are shown in **boldface** and *italics*, respectively, with a subscript that indicates the axis. The symbols $\perp$ and $\parallel$ correspond respectively to the axes perpendicular and parallel to the background magnetic field, $\mathbf{B}_0$. Likewise, x, y, and z

are used to indicate the axes of a Cartesian coordinate system; x_{GSE}, y_{GSE}, and z_{GSE} refer to the axes of the geocentric solar ecliptic coordinate system (Russell, 1971) in particular. A normalized vector quantity (i.e., unit vector), its projections, and its components are also typeset according to these conventions, but each of these additionally bears a caret symbol $\hat{}$ above it.

A tensor appears in **boldface sans-serif**, and each of its components appears in *italics* with subscripts that are listed in "row-column" order; i.e., for any tensor C,

$$\mathsf{C} = \begin{pmatrix} C_{xx} & C_{xy} & C_{xz} \\ C_{yx} & C_{yy} & C_{yz} \\ C_{zx} & C_{zy} & C_{zz} \end{pmatrix} \quad . \tag{A.1}$$

The juxtaposition of two vectors (without any operator between them) indicates their dyadic product, the result of which is a tensor. For example, for any two vectors $\mathbf{a}$ and $\mathbf{b}$,

$$\mathbf{a}\,\mathbf{b} = \begin{pmatrix} a_x\,b_x & a_x\,b_y & a_x\,b_z \\ a_y\,b_x & a_y\,b_y & a_y\,b_z \\ a_z\,b_x & a_z\,b_y & a_z\,b_z \end{pmatrix} \quad . \tag{A.2}$$

The principal mathematical variables that appear in this dissertation are listed in Appendix B. As elsewhere in this document, a subscript j is used to indicate a given particle species (with $j = p$ for protons, $j = \alpha$ for α-particles, and $j = e$ for electrons). Some symbols in Appendix B appear with parenthetical superscripts, which indicate that the symbols are serving specialized purposes. Additionally, in the main body of this dissertation, a superscript (b) is added to a symbol from Appendix B when it is used under the assumption of a bi-Maxwellian VDF (see Equation 1.5). Likewise, the superscripts (0) and (1) are applied to indicate respectively the zeroth- and first-order terms in the expansion of a function (see, e.g., Equation 5.4). In a few cases, these superscripts are combined to form $(b0)$ and $(b1)$.

Appendix B

Index of Symbols

Symbol	Description	Reference
$\mathbf{1}$	Unit tensor (i.e., 3×3 identity matrix)	Equation 5.25
A	Effective collecting area	Section 2.3.1
A_c	Proton collisional age	Equation 1.14
a	Fit parameter for $\mathcal{R}_j(\beta_{\parallel j})$	Equation 6.4
$\mathbf{B}$	Magnetic field	Equation 5.3
$\overline{\mathbf{B}}$	Mean measured magnetic field	Equation 3.20
$\mathbf{B}_0$	Background magnetic field	Section 1.2.2
$\mathbf{B}_\xi$	ξ-th magnetic field measurement	Equation 3.20
b	Fit parameter for $\mathcal{R}_j(\beta_{\parallel j})$	Equation 6.4
b_j	Phase of plasma wave	Equation 5.36
D	Distance of an observer from the Sun	Equation 1.14
c	Speed of light *in vacuo*	Mohr et al. (2008)
c_A	Alfvén speed	Equation 1.11

$\mathbf{E}$	Electric field	Equation 5.3
$\mathbf{F}$	Force	Equation 5.2
F_{zj}	Reduced VDF of species j along the z-axis	Equation 2.16
$\tilde{F}_{z\eta j}$	Inferred value of $F_{z\eta j}$	Equation 3.7
f_j	Velocity distribution function (VDF) of species j	Section 1.2.2
I_j	Collector-plate current from species j	Section 2.3.1
i	Imaginary unit (i.e., $\sqrt{-1}$)	Equation 5.5
$\overline{I}$	Mean current from Faraday cup collector plate	Equation 2.12
$\mathbf{J}$	Current density	Equation 5.6d
$\mathbf{k}$	Wavevector	Section 5.2.1
k	Wavenumber (i.e., $\lvert\mathbf{k}\rvert$)	Equation 5.13
k_B	Boltzmann constant	Mohr et al. (2008)
$\mathbf{k}_{\max}$	Value of $\mathbf{k}$ corresponding to $\gamma_{\max}$	Equation 5.7
$k_{\max}$	Value of k corresponding to $\gamma_{\max}$	Equation 5.51
m_j	Mass of a particle of species j	Equation 1.2
N	Total number of spectra in a histogram	Section 6.5
n	Number of spectra in a given bin of a histogram	Section 6.5
n_j	Number density of species j	Equation 1.1
$\tilde{n}_{\eta j}$	η-th inferred value of n_j	Equation 3.11
p	Probability distribution	Section 6.5
q_j	Charge of a particle of species j	Equation 1.8
$R_\oplus$	Radius of the Earth	Equation 4.1
R_j	Temperature anisotropy (ratio) of species j	Equation 1.4
$\mathcal{R}_j$	Instability threshold in the $(\beta_{\parallel j}, R_j)$-plane	Section 6.3

$\mathbf{r}$	Position in space	Section 5.2.1
$\mathbf{r}^{(s)}$	Position of the *Wind* spacecraft	Equation 4.2
T_j	Scalar temperature of species j	Equation 1.2
$T_{\perp j}$	Perpendicular temperature of species j	Section 1.2.2
$T_{\parallel j}$	Parallel temperature of species j	Section 1.2.2
t	Time	Section 2.3.1
t'	Time (variable of integration)	Section 5.3.1
$\mathbf{u}$	Velocity (of an individual particle)	Section 1.2.2
$\mathbf{u}'$	Velocity in rest frame of plasma bulk flow	Equation 2.22
$u_j^{(c)}$	Cut-off speed for species j	Equation 2.8
$u_\xi^{(w)}$	Center inflow-speed of the ξ-th spectral window	Equation 3.1
V	Voltage of Faraday cup modulator grid	Section 2.2
V_0	Voltage offset of Faraday cup modulator grid	Equation 2.1
$V_\xi^{(w)}$	Value of V_0 for the ξ-th spectral window	Section 2.4
$\mathbf{v}_j$	Bulk velocity of species j	Equation 1.1
$\tilde{v}_{z_\eta j}$	Inferred value of $v_{z_\eta j} = \mathbf{v}_j \cdot \hat{\mathbf{z}}_\eta$	Equation 3.13
w_j	RMS thermal speed of species j	Equation 1.1
$w_{\perp j}$	Perpendicular RMS thermal speed of species j	Equation 1.6
$w_{\parallel j}$	Parallel RMS thermal speed of species j	Equation 1.6
w_{zj}	Effective thermal speed along z-axis	Equation 2.19
$\tilde{w}_{z_\eta j}$	Inferred value of $w_{z_\eta j}$	Equation 3.15
$\hat{\mathbf{x}}$	Direction of a Cartesian coordinate system's x-axis	Equation 4.2
$\hat{\mathbf{y}}$	Direction of a Cartesian coordinate system's y-axis	Equation 4.2
$\hat{\mathbf{z}}$	Direction of a Cartesian coordinate system's z-axis	Equation 4.2

$\hat{\mathbf{z}}_\eta$	η-th pointing direction of the Faraday cup	Section 2.4
$\beta_{\parallel j}$	Plasma parallel-β of species j	Equation 1.9
β_0	Fit parameter for $\mathcal{R}_j(\beta_{\parallel j})$	Equation 6.4
γ	Growth rate (i.e., imaginary component of ω)	Equation 5.5
$\gamma_{\max}$	Instability growth rate (local maximum of γ)	Equation 5.7
ΔI	Total demodulated current (from all ion species)	Equation 2.35
ΔI_j	Demodulated current from j-particles	Equation 2.11
$\Delta I^{(n)}$	Noise/background in demodulated current	Equation 2.35
$\Delta J_{(\eta,\xi)}$	Measured value of $\Delta I(\hat{\mathbf{z}}_\eta, \Delta V_\xi^{(w)}, V_\xi^{(w)})$	Equation 2.40
ΔR_j	Width in R_j of a given bin of a histogram	Section 6.5
$\Delta u_\xi^{(w)}$	Width (in inflow speed) of the ξ-th spectral window	Equation 3.2
ΔV	Faraday cup grid voltage amplitude	Equation 2.1
$\Delta V_\xi^{(w)}$	Value of ΔV for the ξ-th spectral window	Section 2.4
$\Delta \mathbf{v}_{\alpha p}$	α-proton differential flow	Equation 3.21
$\Delta\beta_{\parallel j}$	Width in $\beta_{\parallel j}$ of a given bin of a histogram	Section 6.5
ζ	Interspecies anisotropy coupling	Equation 4.4
η	Index for pointing directions in a spectrum	Section 2.4
θ	Angle between $\mathbf{k}$ and $\mathbf{B}$	Equation 5.13
$\theta_{\max}$	Value of θ corresponding to $\gamma_{\max}$	Equation 5.51
Λ_j	Plasma parameter of species j	Equation 1.13
μ_0	Magnetic constant	Mohr et al. (2008)
Ξ	Total number of windows in a spectrum	Section 2.4
ξ	Index for windows in a spectrum	Section 2.4
σ	Uncertainty (in subscripted parameter)	Section 4.1.1

τ	Time relative to t	Equation 5.43
τ_m	Period of Faraday cup modulator voltage	Equation 2.10
τ_j	Self-collision time of species j	Equation 1.12
ϕ	Phase of cyclotron motion	Equation 5.39
χ_R	Reduced-χ	Taylor (1997)
$\psi_{\mathbf{B}}$	Angular deviation in $\mathbf{B}$	Equation 3.23
Ω_j	Cyclotron angular frequency of species j	Equation 1.8
ω	Complex angular frequency	Section 5.2.1
$\omega_{\max}$	Value of ω_r corresponding to $\gamma_{\max}$	Equation 5.8
ω_r	Real component of ω	Equation 5.5